A numerical study of the shape mode oscillation of microbubbles in a viscous compressible liquid

by

CALLAN CORBETT

A thesis submitted to
The University of Birmingham
for the degree of
Doctor of Philosophy (Sc, Qual)

School of Mathematics
The University of Birmingham
AUGUST 2022

Abstract

Recent experiments (Vyas et al. [2020]) have revealed the interesting cleaning effects that take place due to the shape mode oscillation of bubbles over a rigid boundary. Whilst a microbubble was undertaking shape oscillation moving over a bacterial biofilm, it removed the contaminants from the boundary and created a clean path through the biofilm. This demonstrated much higher cleaning efficiency than that associated with the volume oscillation of cavitation bubbles. Hence, the shape mode oscillation of bubbles near to a rigid boundary proves to be an important topic of research and the main topic of this thesis. The viscous, weakly compressible boundary integral method (VCBIM) is initially described and validated against analytical, numerical, and experimental results, achieving excellent agreement. The characteristics of a microbubble in shape oscillation are then studied, finding that the rigid boundary decreases the natural frequency of the modes. It is found that shape oscillation of a nearby bubble generates a significantly larger amount of shear stress on a rigid boundary, agreeing with experimental observations. This exemplifies the applicability of shape oscillation to ultrasonic cleaning. Additionally, the effects of a surfactant on bubble oscillation are examined. The presence of a surfactant is found to have a significant effect on the shape oscillation of bubbles, as well as greatly increasing the shear stress generated on a rigid boundary. Thus, it is found that the presence of a surfactant enhances the cleaning of a surface by the shape oscillation of a nearby bubble.

Acknowledgements

I would like to thank my supervisors Qianxi Wang and Warren Smith, as well as the members of the Birmingham bubble group for their support and guidance.

I would also like to thank the members of the Birmingham PhD department for making this an enjoyable process.

Finally, I would like to thank my friends and family, and my partner Karo, for their constant support and encouragement.

Contents

List of Figures

Chapter 1

Introduction

Bubbles, volumes of gas and vapour completely surrounded by liquid, are associated with many effects that prove to be of interest. Rapid changes of pressure in a liquid can lead to the formation of many small bubbles in the regions of low pressure, a process known as hydrodynamic cavitation. One such example of cavitation is by a ship propeller, where the continual rotation of the propeller leads to significant pressure changes in the surrounding fluid. Regions of cavitation subject to high pressure leads to bubble collapse - a process by which the bubble rapidly contracts. This collapse can lead to undesirable effects (Plesset and Prosperetti [1977]). Firstly, bubble collapse generates shock waves in the fluid that lead to the gradual erosion of the surface of the propeller blades (Wang and Brennen [1995]). Also contributing to this erosion is the impact of liquid jets forming at the end of bubble collapse (Philipp and Lauterborn [1998]). Secondly, underwater noise is produced by collapsing bubbles, which has the potential to negatively impact marine life (Jones [2019]). Finally, the thrust created by the propeller is reduced due to the decreased average density of the fluid surrounding the blades (Lauterborn and Kurz [2010]). Thus, the generation of these bubbles has been subject to many investigations, as well as the mechanism of damage.

Damage to surfaces due to bubble collapse is not all bad news, however, as it can be

utilised and controlled to clean the surfaces of very small medical and electronic devices, as well as dental implants (Bulat [1974], Song et al. [2004]). When sufficiently close to a rigid wall, a bubble can form a jet directed towards it (Plesset and Chapman [1971]). This is due to a high pressure zone that develops at the far side of the bubble. Upon impact, the bubble exerts shear stress on the surface, which has been shown to be enough to remove contaminants (Chahine et al. [2016]). Investigation of the ideal bubble size and distance from the surface is therefore important to optimise this removal, whilst ensuring damage to the surface is minimal. Unfortunately, this method of removal isn't quite optimal due to the fact that the jet won't always be directed as desired. If, for example, the bubble is situated inside a corner, then the jet direction can be difficult to predict (Cui et al. [2020]). To bypass this issue, an acoustic wave can be used.

Subject to an acoustic wave, a bubble experiences a force in the direction of propagation of the wave. This allows for the targeted direction of bubbles, potentially towards a surface or a corner. It is not just for removal of contaminants, however, that bubbles targeted by ultrasound are useful. Targeted drug delivery, where microbubbles are coated with a thin layer of a drug, can be used to increase effectiveness of treatments whilst reducing side effects (Coussios and Roy [2008]). A stream of coated microbubbles are injected into the bloodstream, and an ultrasonic wave of sufficient intensity is focused over a desired region. Upon entering the region of ultrasound, the bubble is activated and forms a liquid jet that leads to the delivery of the drug. This reduces harmful side effects, such as those experienced during chemotherapy treatment, and allows for a larger volume of drug to be delivered to a tumour, for example.

Under the influence of an acoustic wave, a bubble can also develop non-linear oscillations given certain pressure amplitudes and frequencies. An incident acoustic wave drives spherical oscillations, a system that is remarkably stable. Acoustic trapping utilises this stability, and allows for the observation of a bubble oscillating in a wave (Gaitan et al.

[1992]). The bubble experiences very fast, strong collapse under these conditions, yet is not destroyed. By trapping the bubble, one can observe the phenomenon of sonoluminescence (Brenner et al. [2002]). When the ultrasound driven bubble experiences violent collapse, it can emit light that is visible to the naked eye (Putterman and Weninger [2000]). This fascinating occurrence is possible due to the extreme conditions inside the bubble. The temperature of the gases inside the bubble can surpass the temperature at the surface of the sun (Ndiaye et al. [2012]).

If the frequency and amplitude of an incident acoustic wave is close to a natural frequency of oscillation of a bubble, then non-linear oscillations can occur. This can lead to the shape mode oscillation of the bubble, in which sinusoidal patterns appear on the surface (Guédra and Inserra [2018]). Predicting the development of these shape mode oscillations is interesting, with applications to sonoluminescence and medical procedures (Leslie and Kennedy [2006]). Different shape modes, classified by the number of half waves on the surface, lead to different shear stresses exerted by the bubble oscillation. For processes such as sonothromboslysis, in which ultrasonic waves are used to treat medical conditions, microbubbles are injected into the bloodstream to reduce the necessary energy threshold to induce cavitation (Collis et al. [2010]). If shape mode oscillations in these microbubbles develop, then the effects of the different stresses needs to be considered to minimise damage to the body. It is theorised that shape mode oscillations can lead to increased shear stress on nearby surfaces, so can be applied to cavitation cleaning. For delicate structures, the damage caused by the impact of a jet may be extensive. Thus, the nearby shape mode oscillation of a bubble may be enough to clean the surface without forming a jet. Finding the optimal shape mode, distance between the bubble and wall, and other such parameters are therefore important to find. This can be done following the numerical modelling of the bubble.

The boundary integral method is widely used to model bubble dynamics (Lee et al.

[2007], Lucca and Prosperetti [1982], Zhang et al. [1994]). This is due to the fact that it is grid free in the fluid domain, vastly reducing computation time. By only considering the discretised surface of a bubble, the spacial dimension of the problem is reduced by one. In particular, the axisymmetric boundary integral method is often used to study bubbles in an infinite fluid, subject to an acoustic wave, or near to a rigid boundary (Taib [1985], Wang and Blake [2010]). The advantages of axisymmetry include further reduction of spacial dimension, with the increased simplicity allowing for more accurate approximations. Viscous and compressible effects can be implemented to further improve the model. The surface of an axisymmetric bubble is easy to discretise and define. It is for this reason that toroidal bubbles can be modelled, as the domain cut is simple to define. This has not been achieved by three-dimensional models. Compared to other methods employing Eulerian techniques, the axisymmetric boundary integral method, a Lagrangian technique, can study many cycles of oscillation due to the reduced computational cost. This is beneficial for the study of shape mode oscillations of bubbles, since they can take many cycles to develop.

Bubble dynamics has been a central research topic for many decades, providing essential insight into cavitation damage to pumps, turbines, and propellers (Blake and Gibson [1987], Lauterborn and Kurz [2010]). Microbubble dynamics subject to an acoustic wave are associated with applications to cavitation cleaning (Ohl et al. [2006], Chahine et al. [2016], Reuter et al. [2017]). In practice this has been used to remove bacterial biofilms from dental implants, contaminants from microchips, and aide in the sterilisation of medical instruments (Mason [2016]). This has been attributed to the pressure impulse, the micro-steaming associated with bubble oscillation, and high-speed jetting during bubble collapse (Ohl et al. [2006], Chahine et al. [2016], Reuter et al. [2017]).

Recently, (Vyas et al. [2020]) observed an interesting phenomenon in experiments removing dental biofilms from surfaces using cavitation bubbles generated by a scaler

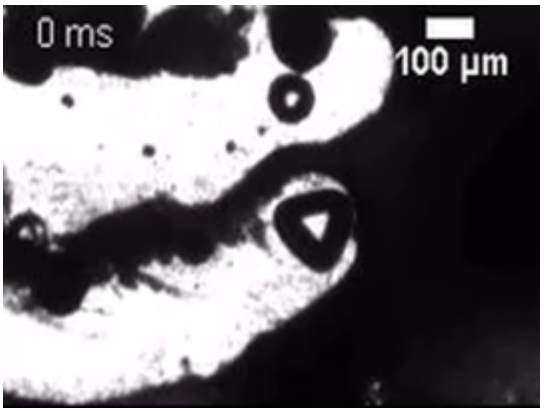

Figure 1.1: Bubbles on the surface exhibit shape oscillations whilst disrupting the biofilm (Vyas et al. [2020]: supplementary video e). Here, the bubble of interest is represented by the triangular black shape near the centre of the image. The white triangle at its centre is due to the effect of the back-light. The black areas represent the biofilm, with the white areas the clean surface. This image shows the path that the bubble in shape oscillation has cleaned through the biofilm.

tip vibrating at high frequency. As shown in figure 1.1, a microbubble in shape mode oscillation directly above a biofilm migrated along the biofilm due to the first Bjerknes force. The shape oscillating bubble removed the contaminating biofilm from the surface and created a clean path through the biofilm, like a brush sweeping away dust. This new phenomenon demonstrated higher cleaning efficiency than that associated with the volume oscillation of microbubbles (Vyas et al. [2020]). This is therefore linked with important applications in ultrasonic cleaning; however, the associated mechanisms are unknown.

There are two important issues to activate and control these applications. Firstly, we need to find the natural frequency of shape modes for a bubble near a rigid boundary. This is because, to activate shape oscillation of bubbles, the driving acoustic wave should be near the natural frequency of shape modes. However, the natural frequency of shape modes has mainly been studied for bubbles in an infinite field. Secondly, it is important to study the cleaning mechanism of a bubble in shape mode oscillation over a boundary, specifically the magnitude and distribution of the shear stress generated at the

boundary due to the shape oscillation of the bubble. This is because the mechanism for surface cleaning is the application of shear stress onto contaminants, dislodging them from the surfaces being cleaned. Theoretical studies were undertaken on shape oscillations of bubbles at small amplitudes using perturbation methods via spherical harmonics, predicting the natural frequency of shape modes and the stability threshold (Plesset [1954]; Prosperetti [1977]; Shaw [2009, 2017]; Doinikov [2004]; Guédra et al. [2017], Guédra and Inserra [2018]). It has been noticed that the natural frequency and amplitude of spherical oscillation of bubbles are affected by the presence of a wall (Garbin et al. [2007]; Doinikov and Bouakaz [2010]; Roovers et al. [2019]). Recently (Maksimov [2020]) extended the theory for a bubble far away from a flat rigid boundary using the method of images.

To study the above two problems, we describe a numerical model for a bubble in shape mode oscillation near as well as in contact with a rigid boundary, based on the boundary integral method (BIM). The viscous effects are approximated by the viscous potential flow theory (Joseph and Wang [2004]; Wang et al. [2022]) and the compressible effects are modelled using weakly compressible flow theory (Wang and Blake [2010, 2011]). Validation of the model is carried out by comparison with theoretical results (Tsamopoulos and Brown [1983]; Maksimov [2020]). The viscous shear stress at the rigid boundary is then approximated using boundary layer theory (Nyborg [1958]; Doinikov and Bouakaz [2010]). Parametric studies are subsequently carried out for the natural frequency of various shape modes and the shear stress generated at the boundary, in terms of the shape mode and the standoff distance of the bubble from the wall.

The presence of a surfactant at the surface of a bubble has the effect of modifying the surface tension (Chang and Franses [1995], Rosen and Kunjappu [2012]). This has numerous useful applications including in cleaning, emulsification and as foaming agents (Brenner [2013]). An interesting application is to ultrasonic cleaning, where the presence of a surfactant can improve cleaning efficiency (Awad and Awad [2022]). Firstly,

the reduced surface tension in the liquid means that cavitation is more likely. Secondly, the energy required to overcome surface tension and promote oscillation is reduced and so more energy is transferred to remove the contaminant. Finally, shape oscillation and jetting have lower energy thresholds to achieve. The extent of the reduction of these thresholds is not known, however, along with the changing properties and cleaning efficiency of shape oscillation. These factors will be found using the weakly compressible, viscous boundary integral method.

Surfactants are generally formed of a hydrophilic head and a hydrophobic tail, which gives them a tendency to adsorb to interfaces with the tail pointing out from the liquid (Piorr [1987]). At an air-water interface, for example, surface tension is particularly high due to the strong hydrogen bonds that form between molecules of water. When a simple non-ionic surfactant is present, however, its adsorption to the interface disrupts the structure reducing the quantity of hydrogen bonds, hence reducing the attraction of the water molecules to each other. This in turn leads to a lower surface tension. In the case that the head of the surfactant is complex or ionic, bonds can form between the heads that can lead to increased surface tension at points on the surface and a non-linear distribution of surface tension. Here, however, we will only consider simple non-ionic surfactants such that molecular interaction between surfactant heads is negligible. Thus, as the concentration of surfactant increases, the surface tension will strictly decrease.

The structure of this thesis is as follows. In Chapter 2, the viscous, weakly compressible boundary integral method (VCBIM) is described. In Chapter 3, results of the VCBIM are presented and compared against analytical, numerical, and experimental results. Excellent agreement is achieved with results for a bubble subject to an acoustic wave, and for a bubble in a viscous compressible liquid. In Chapter 4, the shape mode oscillation of a bubble near to a rigid boundary is examined. The natural frequencies of shape modes are calculated near to a rigid boundary, as is the shear stress generated at

the rigid boundary. This is found using boundary layer theory. In Chapter 5, results are presented for a bubble subject to a surfactant. The natural frequencies of shape modes are calculated for different initial concentrations of surfactants, as is the amplitude of oscillation. The effect of a surfactant on liquid jet formation is also considered.

Chapter 2

Physical, mathematical, and numerical model of an axisymmetric bubble

In this chapter, the governing equations for a bubble in a viscous, weakly compressible fluid will be defined. These equations are valid for a bubble in an infinite fluid, subject to an acoustic wave, and near to a rigid boundary. Compressible effects are modelled using the weakly compressible theory (Wang and Blake [2010, 2011]), with viscous effects approximated using the viscous potential flow theory (Joseph and Wang [2004], Wang et al. [2022]). The process of numerically solving these equations to model numerous cycles of oscillation will then be covered, utilising the axisymmetric boundary integral method (BIM). The 4^{th} order Runge-Kutta scheme used to numerically solve the system of equations will be detailed, along with the discretisation and cubic spline interpolation of the bubble surface, and the treatment of the logarithmic singularities that arise. Finally, the numerical treatment of toroidal bubbles is provided, including the re-discretisation of the bubble surface and insertion of a vortex ring.

2.1 Physical and mathematical model

Consider a bubble with surface S and initial radius R_0 initiated at a distance of s from a rigid boundary, centred at the origin of a Cartesian coordinate system (x, y, z). Inside the bubble is a mixture of gas and vapour, whilst outside the bubble is a liquid, generally water, with domain Ω, viscosity μ, and density ρ. The surrounding liquid is assumed to be irrotational, weakly compressible, and weakly viscous. This configuration is demonstrated in figure 2.1.

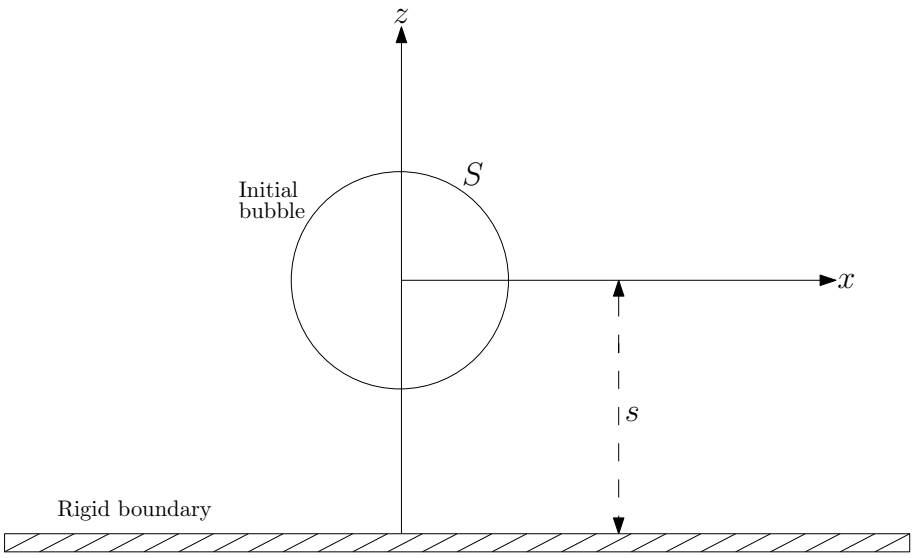

Figure 2.1: A bubble with surface S initiated near to a rigid boundary located at $z = -s$. The bubble is centred at the origin of a Cartesian coordinate system (x, y, z).

Assuming that the fluid flow is irrotational, the velocity field can be expressed as $\mathbf{u} = \nabla\phi$ where the velocity potential ϕ satisfies Laplace's equation $\nabla^2\phi = 0$ in the fluid domain Ω with boundary S. Following from Green's theorem, provided that ϕ is sufficiently smooth, the solution to Laplace's equation can be written in integral form as

$$c(\mathbf{r})\phi(\mathbf{r}) = \int_{\partial\Omega} \left(\frac{\partial\phi}{\partial n}(\mathbf{q})G(\mathbf{r},\mathbf{q}) - \phi(\mathbf{q})\frac{\partial G}{\partial n}(\mathbf{r},\mathbf{q}) \right) \mathrm{d}S(\mathbf{q}), \tag{2.1.1}$$

where $\mathbf{r} \in \Omega \cup \partial\Omega$ and $\mathbf{q} \in \partial\Omega$ represent the field points and source points respectively,

$\partial\Omega$ is the boundary of the fluid domain where $\partial\Omega = S \cup S_w$ with S and S_w the surface of the bubble and wall respectively, and the normal derivative is defined by $\partial/\partial n = \widehat{\mathbf{n}} \cdot \nabla$, where the unit normal $\widehat{\mathbf{n}} = (n_x, n_y, n_z)$ points outwards from the fluid towards the centre of the bubble. The constant $c(\mathbf{r})$, which represents the solid angle, is defined by

$$c(\mathbf{r}) = \begin{cases} 4\pi, & \text{if } \mathbf{r} \in \Omega; \\ 2\pi, & \text{if } \mathbf{r} \in \partial\Omega. \end{cases} \tag{2.1.2}$$

The Greens function $G(\mathbf{r}, \mathbf{q})$ for a bubble in the presence of a rigid boundary is defined as

$$G(\mathbf{r}, \mathbf{q}) = \frac{1}{|\mathbf{r} - \mathbf{q}|} + \frac{1}{|\mathbf{r} - \mathbf{q}_{im}|}, \tag{2.1.3}$$

where $\mathbf{q}_{im}$ is the image of the source points reflected across the boundary. The insertion of an image bubble utilises the method of images to take into account the presence of the wall, and satisfies the no-flux boundary condition

$$\left.\frac{\partial\phi}{\partial n}\right|_{S_w} = 0. \tag{2.1.4}$$

2.1.1 Viscous effects

In bubble dynamics, driven by inertia as the associated Reynolds number $Re = \rho U R_0/\mu$ is often large, viscous effects are solely located in a thin viscous boundary layer at the surface of the bubble with thickness $\mathcal{O}(R_0/\sqrt{Re})$ (Batchelor and Batchelor [2000], Boulton-Stone and Blake [1993]). In certain circumstances such as with multiple cycles of stable shape mode oscillation, the associated Reynolds number can be $\mathcal{O}(10)$ given lower values of the velocity scale. This leads to non-negligible viscous effects, especially when considering the compound effect of viscosity over multiple cycles of oscillation. Thus, viscosity must be accounted for. The effects of viscoelasticity were included in the potential flow theory of

microbubbles by (Lind and Phillips [2010, 2012, 2013]).

Consider the surface of a bubble surrounded by a liquid with viscosity μ, under the effect of surface tension. The gas inside the bubble is assumed to be inviscid. The normal stress across the interface must be constant, i.e. there is no jump in stress across the surface. Thus, assuming that there is no mass transfer across the interface, it is required that

$$(\boldsymbol{\sigma}_L - \boldsymbol{\sigma}_B) \cdot \widehat{\mathbf{n}} = \sigma\kappa\widehat{\mathbf{n}}, \tag{2.1.5}$$

where σ_L and σ_B represent the normal stress tensors at the liquid and gas side of the interface respectively, σ the surface tension coefficient of the liquid gas interface, and $\kappa = \nabla \cdot \widehat{\mathbf{n}}$ the total curvature of the surface. This is known as the dynamic boundary condition. Using the relation that

$$\boldsymbol{\sigma} \cdot \widehat{\mathbf{n}} = \sigma_{nn}(\mathbf{r}) = -p(\mathbf{r}) + \tau_{nn} \qquad \text{for } \mathbf{r} \in \partial\Omega, \tag{2.1.6}$$

where σ_{nn} is the normal component of the normal stress tensor, p is the pressure at the interface, and τ_{nn} is the normal-normal component of the deviatoric stress tensor, we can write

$$p_L(\mathbf{r}) = p_B - \sigma\nabla \cdot \widehat{\mathbf{n}} + \tau_{nn}, \text{ where } \tau_{nn} = 2\mu\frac{\partial^2\phi}{\partial n^2}. \tag{2.1.7}$$

Here, τ_{nn} is calculated using the Frenet formulae and definition of the stress tensor $\mathbf{T} = 2\mu\nabla\mathbf{u}$ (Miksis et al. [1982]). However, using this stress balance leads to a singularity arising at the surface of the bubble. The shear stress at the gas side of the interface is equal to zero as the gas is assumed to be inviscid, but the shear stress at the liquid side is non-zero as the liquid has viscosity μ. To counter this discrepancy, a viscous pressure correction term p_{vc} is introduced to the normal stress balance (Joseph and Wang [2004]).

The stress balance at the bubble surface is then written

$$p_L(\mathbf{r}) = p_B - \sigma\nabla\cdot\widehat{\mathbf{n}} - p_{vc} + 2\mu\frac{\partial^2\phi}{\partial n^2} \qquad \text{for } \mathbf{r}\in\partial\Omega. \tag{2.1.8}$$

To be physical, the pressure correction term needs to satisfy the conservation of energy of the flow, and it must have an equivalent power contribution as the shear stress at the surface of the bubble. Now, comparing the work done on each surface element dS by the viscous correction term and the shear stress yields

$$\mathrm{d}W = -u_n p_{vc}\,\mathrm{d}S \;\text{ and }\; \mathrm{d}W = \mathbf{u}_\tau\cdot\boldsymbol{\tau}_s\,\mathrm{d}S, \tag{2.1.9}$$

respectively, where at each surface element, u_n represents the normal velocity, $\mathbf{u}_\tau$ the tangential velocity, and τ_s the shear stress. The minus sign in the first term is required as the normal vector faces outwards from the liquid. Over the whole surface,

$$\int_S u_n(-p_{vc})\,\mathrm{d}S = \int_S \mathbf{u}_\tau\cdot\boldsymbol{\tau}_s\,\mathrm{d}S. \tag{2.1.10}$$

It can be assumed that the viscous pressure correction term is directly proportional to the normal stress (Manmi and Wang [2017]), hence $p_{vc} = -C\tau_{nn}$, where C is some constant to be determined. Now (2.1.8) can be written

$$p_L(\mathbf{r}) = p_B - \sigma\nabla\cdot\widehat{\mathbf{n}} + 2\mu(1+C)\frac{\partial^2\phi}{\partial n^2}. \tag{2.1.11}$$

As the shear stress $\boldsymbol{\tau_s}$ proves difficult to directly compute, an extra step is required to find C. The energy dissipation rate is defined (Zhang and Ni [2013]), where $\boldsymbol{\sigma}$ is the stress tensor, by

$$D = \int_S \mathbf{u}\cdot\boldsymbol{\sigma}\cdot\widehat{\mathbf{n}}\,\mathrm{d}S = \int_S u_n\tau_{nn}dS + \int_S \mathbf{u}_\tau\cdot\boldsymbol{\tau}_s\,\mathrm{d}S. \tag{2.1.12}$$

Following the substitution of (2.1.10) into (2.1.12) and using the relations $u_n = \partial\phi/\partial n$, $\tau_{nn} = \partial^2\phi/\partial n^2$, and $p_{vc} = -C\tau_{nn}$, the energy dissipation can be written

$$D = 2\mu(1+C)\int_S \frac{\partial\phi}{\partial n}\frac{\partial^2\phi}{\partial n^2}\,\mathrm{d}S. \tag{2.1.13}$$

An alternative definition of the energy dissipation rate can be found in Lamb [1932], where

$$D = 2\mu\int_S \left[\phi_x\frac{\partial\phi_x}{\partial n} + \phi_y\frac{\partial\phi_y}{\partial n} + \phi_z\frac{\partial\phi_z}{\partial n}\right]\,\mathrm{d}S. \tag{2.1.14}$$

Upon equating these two equations for D, the constant C can be written

$$C = \frac{\int_S \nabla\phi\cdot\frac{\partial\nabla\phi}{\partial n}\,\mathrm{d}S}{\int_S \frac{\partial\phi}{\partial n}\frac{\partial^2\phi}{\partial n^2}\,\mathrm{d}S} - 1. \tag{2.1.15}$$

Pressure inside the bubble

The pressure inside a bubble is assumed to be constant in space, i.e. $p_B = p_B(t)$. This is because the internal gases have a significantly lower density and viscosity than the surrounding liquid, with $\rho_g \ll \rho_l$, and $\mu_g \ll \mu_l$.

The contents of a bubble consists of a mixture of gases and vapour. Each of the gases in the mixture contributes to the total gas pressure, which increases when the volume of the bubble decreases. The vapour, in a state of thermodynamic equilibrium with its condensed phases, also exerts a pressure. From Dalton's law for an ideal gas in an adiabatic system, the total pressure inside the bubble is given by (Best and Kucera [1992])

$$p_B(t) = p_v + p_{g0}\left(\frac{V_0}{V(t)}\right)^{\lambda}, \tag{2.1.16}$$

where p_v is the constant vapour pressure, p_{g0} the initial partial gas pressure, V the volume of the bubble at time t, V_0 the initial volume and λ the polytropic index of the gases.

We do not consider the thermal effects associated with this phenomenon (Szeri et al. [2003]; Fuster and Montel [2015]). This equation is constant in space but varies in time, as required.

Pressure in surrounding liquid

For a potential flow, Bernoulli's equation must be satisfied by the velocity potential. The potential must also satisfy the far-field condition, which requires that the potential ϕ goes to zero when $r \to \infty$. This is because the fluid in the far-field is assumed to be undisturbed. Gravitational forces are generally ignored given the small Bond number associated with microbubble dynamics, which for water $Bo = \rho R_0^2 g/\sigma = \mathcal{O}(10^{-7})$. Bernoulli's equation is given by

$$\frac{\partial \phi}{\partial t} + \frac{1}{2}|\nabla \phi|^2 + \frac{p}{\rho} + gz = c(t), \tag{2.1.17}$$

where $c(t)$ is constant in space. For a bubble initially at rest located at $z = s$, $\phi = 0$ and $p = p_\infty$ where p_∞ denotes the ambient pressure in the system. Hence,

$$\rho \frac{\partial \phi}{\partial t} + \frac{\rho}{2}|\nabla \phi|^2 + p - p_\infty + \rho g(z - s) = 0. \tag{2.1.18}$$

It then follows that the pressure at any point in the liquid, p_L, is given by:

$$p_L = p_\infty - \rho \left(\frac{\partial \phi}{\partial t} + \frac{1}{2}|\nabla \phi|^2 + g(z - s) \right). \tag{2.1.19}$$

Using the terms for the pressure at either side of the interface, the dynamic boundary condition follows.

Dynamic boundary condition at the surface of a bubble including viscous effects

Using equations (2.1.11), (2.1.16) and (2.1.19), along with the following identity

$$\frac{\partial\phi}{\partial t}+\frac{1}{2}|\nabla\phi|^2=\frac{\partial\phi}{\partial t}+\mathbf{u}\cdot\nabla\phi-\frac{1}{2}|\nabla\phi|^2=\frac{D\phi}{Dt}-\frac{1}{2}|\nabla\phi|^2, \tag{2.1.20}$$

the dynamic boundary condition (DBC) on the surface of the bubble can be written

$$\frac{D\phi}{Dt}\Big|_S=\frac{1}{2}|\nabla\phi|^2+\frac{p_\infty+p_{ac}-p_v}{\rho}-\frac{p_{g0}}{\rho}\left(\frac{V_0}{V}\right)^\lambda-g(z-s)+\frac{\sigma}{\rho}\nabla\cdot\widehat{\mathbf{n}}+2\frac{\mu}{\rho}(1+C)\frac{\partial^2\phi}{\partial n^2}, \tag{2.1.21}$$

where p_{ac} represents pressure due to an acoustic wave. This equation tracks the changing potential of the fluid over time at the surface of the bubble.

To account for the presence of a plane harmonic acoustic wave travelling along the z axis with pressure contribution p_{ac}, the ambient pressure p_∞ is replaced by

$$p_\infty+p_{ac},\quad\text{where}\quad p_{ac}=p_a\sin(kz-\omega t), \tag{2.1.22}$$

where p_a is the pressure amplitude, k the wave-number, and ω the angular frequency of the wave. This is because the far-field pressure is now equal to the hydrostatic pressure of the fluid at rest plus the effect of the pressure oscillation of the acoustic wave.

Kinematic boundary condition

It is required that a fluid particle located at a free surface, say $\mathbf{r}_p(t)$, must remain on the free surface for all time. This is known as the kinematic boundary condition (KBC), and is written

$$\frac{D\mathbf{r}_p(t)}{Dt}=\mathbf{u}(\mathbf{r}_p,t), \tag{2.1.23}$$

where $\mathbf{u}(\mathbf{r}_p, t)$ is the velocity of the fluid particle at time t. This equation is used to track the changing position of the free surface. For a bubble with velocity potential ϕ, this can be written

$$\frac{D\mathbf{r}}{Dt}\Big|_S = \nabla\phi. \tag{2.1.24}$$

Dimensionless form

The following scales are introduced, where dimensionless variables are denoted by a star,

$$L = R_0 L^*, \quad p = \nabla p p^*, \quad t = T t^*, \quad u = U u^*. \tag{2.1.25}$$

Here, the length L is scaled by the initial bubble radius R_0, the pressure p by the pressure difference $\nabla p = p_\infty - p_v$, time t by the time scale T, and velocity u by the velocity scale U. The velocity and time scales are defined by

$$U = \sqrt{\frac{\nabla p}{\rho}}, \quad T = \frac{R_0}{U}. \tag{2.1.26}$$

The following identities are used to reduce the system to dimensionless form

$$z = R_0 z^*, \quad \gamma = s/R_0, \quad \nabla = \frac{1}{R_0}\nabla^*, \quad \phi = R_0 U \phi^*. \tag{2.1.27}$$

Upon substitution, the KBC becomes:

$$\frac{R_0}{T}\frac{D\mathbf{r}^*}{Dt^*} = \frac{R_0 U}{R_0}\nabla^*\phi^*, \tag{2.1.28}$$

so using the definition of the time scale, the dimensionless form of the KBC can be written

$$\frac{D\mathbf{r}^*}{Dt^*}\Big|_S = \nabla^*\phi^*. \tag{2.1.29}$$

Substitution of the scales into the DBC yields the dimensionless DBC

$$\frac{D\phi^*}{Dt^*} = \frac{1}{2}|\nabla^*\phi^*|^2 + \left(1 + \frac{p_{ac}}{\Delta p} - \frac{p_{g0}}{\Delta p}\left(\frac{V_0}{V}\right)^{\lambda}\right) - \frac{gR_0\rho}{\Delta p}(z^* - \gamma) + \frac{\sigma}{\Delta p R_0}\nabla^* \cdot \widehat{\mathbf{n}} + 2\frac{\mu}{\rho R_0 U}(1 + C)\frac{\partial^2\phi^*}{\partial n^2}. \tag{2.1.30}$$

Setting some non-dimensional parameters to simplify this equation, namely

$$\varepsilon_p = \frac{p_{g0}}{\Delta p}, \;\; p_a = \Delta p \, p_a^*, \;\; \delta = \sqrt{\frac{gR_0\rho}{\Delta p}}, \;\; Re = \frac{\rho R_0 U}{\mu} \;\text{ and }\; We = \frac{R_0\Delta p}{\sigma}, \tag{2.1.31}$$

yields the dimensionless DBC, which after dropping stars becomes:

$$\frac{D\phi}{Dt}\Big|_S = 1 + \frac{1}{2}|\nabla\phi|^2 + p_a \sin(kz - \omega t) - \varepsilon_p\left(\frac{V_0}{V}\right)^{\lambda} - \delta^2(z - \gamma) + \frac{\nabla \cdot \widehat{\mathbf{n}}}{We} + \frac{2}{Re}(1 + C)\frac{\partial^2\phi}{\partial n^2}. \tag{2.1.32}$$

Here, the non-dimensional parameters ε_p, δ, We, and Re represent properties of the system (Brennen and Brennen [1995]). The strength parameter ε_p is a measure of the initial pressure inside the bubble compared to the ambient pressure at the level of the centre of the bubble at inception. The larger the value of ε_p, the more excess pressure there is inside the bubble. The buoyancy parameter δ corresponds to the ratio of half of the lifetime of the bubble with the time taken for the bubble to rise a distance R_0 under the effect of gravity. Thus, the larger the buoyancy parameter, the faster the bubble rises. The Weber number We represents the importance of fluid inertia against surface tension. The higher the Weber number, the more important the fluid inertia and the smaller the relative effect of surface tension. The Reynolds number Re quantifies the significance of fluid inertial forces against viscous forces. A low Reynolds number indicates viscous effects are the dominant force in the system, whilst a high Reynolds number means that

viscous effects are not important.

2.1.2 Weakly compressible theory

The Mach number measuring the compressibility of a fluid flow is defined by

$$\varepsilon = \frac{U}{c_\infty}, \tag{2.1.33}$$

where U is the reference velocity of the flow, and c_∞ is the speed of sound in the fluid. Bubble dynamics is often associated with a low Mach number, as the speed of sound in the liquid is significantly larger than the maximum velocity observed during bubble oscillation. This maximum velocity occurs during jet formation, which for micrometer sized bubbles has been shown to reach speeds of up to 150 ms^{-1} (Brujan and Matsumoto [2012]). The speed of sound in undisturbed water is $\sim$ 1500 ms^{-1}, leading to a Mach number with a maximum value of $\varepsilon = 0.1$. Here, the Mach number is assumed to be small with $\varepsilon \ll 1$. Thus, the flow can be described as weakly compressible.

For the conservation of mass of a compressible flow to be satisfied, the density of the fluid $\rho(\mathbf{r}, t)$ and velocity field $\mathbf{u}$ must satisfy

$$\frac{\partial \rho}{\partial t} + \nabla \cdot (\rho \mathbf{u}) = 0, \tag{2.1.34}$$

and for the conservation of momentum must satisfy Euler's equation

$$\frac{\partial \mathbf{u}}{\partial t} + \mathbf{u} \cdot \nabla \mathbf{u} = \mathbf{f} - \frac{1}{\rho} \nabla p, \tag{2.1.35}$$

where $\mathbf{f}$ represents body forces and p pressure. With the speed of sound and enthalpy defined as

$$c^2 = \frac{\mathrm{d}p}{\mathrm{d}\rho}, \qquad h = \int_{p_\infty}^{p} \frac{\mathrm{d}p}{\rho}, \tag{2.1.36}$$

substituting into 2.1.34 and 2.1.35, using that the fluid is irrotational, Taylor expanding and then nondimensionalising, we receive the equations governing liquid flow at low Mach number. The conservation of mass equation becomes (Wang and Blake [2010]):

$$\nabla^2\phi + \frac{\varepsilon^2}{c^2}\left(\frac{\partial p}{\partial t} + \nabla\phi \cdot \nabla p\right) = \mathcal{O}(\varepsilon^4), \tag{2.1.37}$$

and Euler's equation becomes Bernoulli's equation given by

$$\frac{\partial \phi}{\partial t} + \frac{1}{2}|\nabla\phi|^2 + p + \delta^2 z = \mathcal{O}(\varepsilon^2). \tag{2.1.38}$$

The fluid domain of the inviscid flow is separated into two regions (Wang [2014]). These are the inner region near the bubble where $(x, y, z) = \mathcal{O}(R_0)$ and the outer region far away from the bubble where $(x, y, z) = \mathcal{O}(\lambda)$. Here $\lambda = c_\infty R_0/U = R_0/\varepsilon$ where λ is the wavelength of the acoustic waves generated by the bubble oscillating. These shockwaves occur as the bubble approaches its minimum volume, and occur due to compressible effects. This configuration is demonstrated below in figure 2.2.

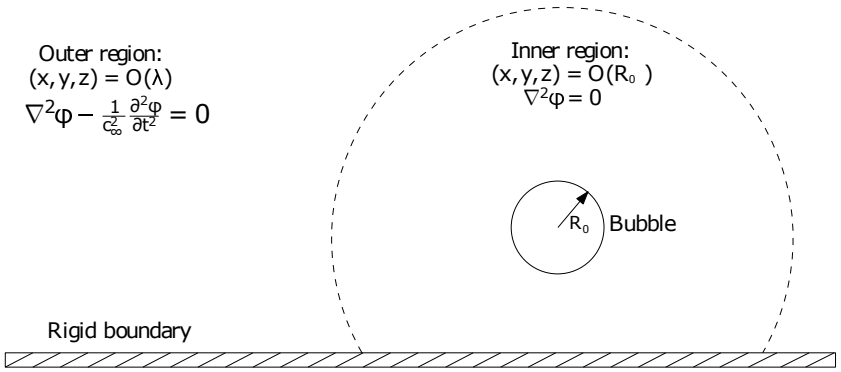

Figure 2.2: A schematic of a bubble near a wall in a compressible fluid, with the fluid domain split into two separate regions. The length scale at the far field is much larger than the bubble maximum radius.

In the outer region the variable $\tilde{\mathbf{r}} = \varepsilon \mathbf{r}$ is introduced, leading to the following expressions

$$\phi(\mathbf{r}, t) = \Phi(\tilde{\mathbf{r}}, t) = \Phi_0(\tilde{\mathbf{r}}, t) + \varepsilon \Phi_1(\tilde{\mathbf{r}}, t) + \mathcal{O}(\varepsilon^2), \tag{2.1.39}$$

$$p(\mathbf{r}, t) = P(\tilde{\mathbf{r}}, t) = P_0(\tilde{\mathbf{r}}, t) + \varepsilon P_1(\tilde{\mathbf{r}}, t) + \mathcal{O}(\varepsilon^2). \tag{2.1.40}$$

Substitution of the outer expansions into (2.1.37) and (2.1.38) yields the wave equation

$$\tilde{\nabla}^2 \Phi_i - \frac{\partial^2 \Phi_i}{\partial t^2} = 0 \qquad \text{for } i = 0, 1, \tag{2.1.41}$$

for the first two orders, meaning the outer solution must satisfy the wave equation for the first two orders. The first order solution follows from the requirement for the potential to decompose to zero in the far field at first order. At second order D'Alembert's solution of the wave equation is used. Due to the Sommerfeld radiation condition, the solution cannot contain incoming waves. Thus the first two order solutions are given by (Wang and Blake [2011]):

$$\Phi_0 = 0, \qquad \Phi_1 = \frac{F_1(t - |\tilde{\mathbf{r}}|)}{|\tilde{\mathbf{r}}|}. \tag{2.1.42}$$

The arbitrary function F_1 is calculated by asymptotic matching with the inner solution. In order to perform this matching, the inner limits of the first two-order solutions are considered. Hence,

$$(\Phi_0)^i = 0, \quad (\Phi_1)^i = \frac{F_1(t - \varepsilon r)}{\varepsilon r} = \frac{F_1(t)}{\varepsilon r} - F_1'(t) + \mathcal{O}(\varepsilon). \tag{2.1.43}$$

Substitution into (2.1.39) then yields the inner limit of the outer expansion

$$(\Phi)^i = \frac{F_1(t)}{r} - \varepsilon F_1'(t) + \mathcal{O}(\varepsilon^2). \tag{2.1.44}$$

For the inner solution, it can be written that

$$\phi(\mathbf{r},t) = \phi_0(\mathbf{r},t) + \varepsilon\phi_1(\mathbf{r},t) + \mathcal{O}(\varepsilon^2), \tag{2.1.45}$$

$$p(\mathbf{r},t) = p_0(\mathbf{r},t) + \varepsilon p_1(\mathbf{r},t) + \mathcal{O}(\varepsilon^2). \tag{2.1.46}$$

Once again substituting these into (2.1.37) and (2.1.38), it is found that the inner region satisfies Laplace's equation for the first two orders. Hence

$$\nabla^2\phi_i = 0 \qquad \text{for } i = 0, 1. \tag{2.1.47}$$

Using Gauss' second identity the general solution can be written (Wang [2014])

$$\phi_i(\mathbf{r}) = f_i(t) + \frac{1}{4\pi}\int_S \frac{\partial\phi_i(\mathbf{q},t)}{\partial n}G(\mathbf{r},\mathbf{q}) - \phi_i(\mathbf{q},t)\frac{\partial G(\mathbf{r},\mathbf{q})}{\partial n}dS(\mathbf{q}) \quad \text{for } i = 0, 1. \tag{2.1.48}$$

Here, $f_i(t)$ is an arbitrary function to be found after asymptotic matching, $\mathbf{q}$ is the position vector of a source point, $\widehat{\mathbf{n}}$ the outward facing normal vector from the bubble surface S, and $G(\mathbf{r},\mathbf{q})$ the Green's function as before defined by

$$G(\mathbf{r},\mathbf{q}) = \frac{1}{|\mathbf{r}-\mathbf{q}|} + \frac{1}{|\mathbf{r}-\mathbf{q}_{im}|}. \tag{2.1.49}$$

Upon taking the outer limit of these inner solutions, it follows that

$$(\phi_i)^o = f_i(t) + \varepsilon\frac{1}{2\pi}\frac{m_i(t)}{r} + \mathcal{O}(\varepsilon^2), \tag{2.1.50}$$

where

$$m_i(t) = \int_S \frac{\partial\phi_i(\mathbf{q},t)}{\partial n}dS(\mathbf{q}) \quad \text{for } i = 0, 1. \tag{2.1.51}$$

Then the general form of the outer limit of the inner expansion is given by

$$(\phi)^o = f_0(t) + \frac{1}{2\pi}\frac{m_0(t)}{r} + \varepsilon f_1(t) + \mathcal{O}(\varepsilon^2). \tag{2.1.52}$$

Now Van Dyke's matching principle (Dyke [1975]) is used to find the arbitrary functions. Setting

$$(\phi)^o = (\Phi)^i, \tag{2.1.53}$$

yields

$$f_0(t) + \frac{1}{2\pi}\frac{m_0(t)}{r} + \varepsilon f_1(t) = \frac{F_1(t)}{r} - \varepsilon F_1'(t) + \mathcal{O}(\varepsilon^2). \tag{2.1.54}$$

It then follows that the arbitrary functions are defined by

$$f_0(t) = 0, \quad f_1(t) = -\frac{m_0'(t)}{2\pi}, \quad F_1(t) = \frac{m_0(t)}{2\pi}. \tag{2.1.55}$$

Note that given the value of $f_0(t)$ and $f_1(t)$, the far-field condition of the inner solution can be found. Taking the limit as $r \to \infty$ of the outer limit of the inner solution $(\phi)^o$ finds that

$$\phi|_{r\to\infty} = -\varepsilon\frac{m_0'(t)}{2\pi} + \mathcal{O}(\varepsilon^2). \tag{2.1.56}$$

The weakly compressible model essentially models an incompressible flow in the inner region, and a flow governed by the wave equation in the outer region. This is to be expected, due to the difference in timescales between the bubble collapse, T, and the acoustic wave travelling through the inner region, T_a. It is found that

$$\frac{T_a}{T} = \mathcal{O}\left(\frac{R_m/c_\infty}{R_m/U}\right) = \mathcal{O}(\varepsilon), \tag{2.1.57}$$

which means that to first order the acoustic wave instantly travels through the inner region. It can also be assumed that the effects of the acoustic wave lead to constant

differences in the pressure and velocity in the inner region to first order. This agrees with the inner region being modelled as incompressible.

Now, a transformation is introduced ensuring that the potential decays to zero in the far-field satisfying Laplace's equation, which is given by

$$\phi = \Phi - \varepsilon \frac{m_0'(t)}{2\pi}. \tag{2.1.58}$$

Using this substitution, the set of governing equations is given by

$$\nabla^2 \Phi = \mathcal{O}(\varepsilon^2), \tag{2.1.59a}$$

$$\frac{D\mathbf{r}}{Dt}\Big|_S = \nabla\Phi + \mathcal{O}(\varepsilon^2), \tag{2.1.59b}$$

$$\begin{aligned}\frac{D\Phi}{Dt}\Big|_S = 1 + \frac{1}{2}|\nabla\Phi|^2 - \varepsilon_p \left(\frac{V_0}{V}\right)^{\lambda} + p_a \sin(\omega t) - (\delta^2 + \delta_c)(z - z_0) \\ + \frac{\kappa}{We} - \frac{2(1+C)}{Re}\frac{\partial^2 \Phi}{\partial n^2} + \varepsilon \frac{m_0''(t)}{2\pi} + \mathcal{O}(\varepsilon^2),\end{aligned} \tag{2.1.59c}$$

with boundary conditions

$$\Phi\big|_{r\to\infty} = \mathcal{O}(\varepsilon^2), \tag{2.1.59d}$$

$$\Phi_n\big|_{z=-z_0} = 0. \tag{2.1.59e}$$

Here $\delta_c = \varepsilon\omega^2 \cos(\omega t)$. This term is a result of the asymptotic matching. This is a simple addition to the derivation as in Wang and Blake [2010]. Here Φ, henceforth referred to as ϕ for simplicity, satisfies Laplace's equation and decays to zero in the far field. This is now in the right form to apply the boundary integral method, and numerically solve the model.

2.2 Numerical modelling of an axisymmetric bubble

2.2.1 Boundary integral method modelling

To numerically model the evolution of the bubble over time, the kinematic and dynamic boundary conditions can be used. For an axisymmetric bubble, The surface of the bubble is discretised into a set of, say, $N + 1$ nodes. At each node, the initial velocity potential and position is known. Using Lagrangian time integration, the DBC can numerically approximate the potential ϕ at each node of the surface of the bubble over time, following the introduction of an appropriately small time step Δt. The boundary integral method, utilising the boundary integral equation (2.1.1), can then be used to calculate the normal velocity at each node. The tangential velocity at each node can be approximated given that the potential at the neighbouring nodes is known. With both the tangential and normal velocity at each node of the surface known, the velocity is easily calculated. Finally, given that the velocity at each node of the surface is known, the position of the surface after a time step Δt can be calculated using the kinematic boundary condition. Once again, Lagrangian time integration is used to do this.

The boundary integral method, known as the BIM, is based upon Green's second identity. It is a widely used method in bubble dynamics (Lee et al. [2007], Lucca and Prosperetti [1982], Zhang et al. [1994]). It allows for the reduction of the dimension of the problem by one by reformulating Laplace's equation as the solution to a Fredholm integral equation. This is known as the boundary integral equation. In the case of an axisymmetric problem, the dimension of these integrals can be reduced from two to one upon integration through the azimuthal angle. Assuming that the bubble is axisymmetric about the z axis allows for significantly simpler and faster computations. Given that many of the interesting phenomena in bubble dynamics are in essence axisymmetric, making this assumption does not lead to significant inaccuracy given appropriate application of

the model (Blake et al. [1986]). Some accuracy is lost by discretising the surface of the bubble, but this can be significantly reduced by ensuring a fine mesh. As well as reducing the dimension of the problem, the BIM is also mesh-less in the fluid domain as only the behaviour at the surface is considered. This leads to a significant reduction in the computation time that is required, which means that the BIM has the unique ability to model multiple cycles of oscillation. This is particularly useful when considering effects such as resonant oscillation that can take multiple cycles to develop. Alternative methods such as the volume of fluids method require a mesh over the entire fluid domain, leading to a significantly higher computational cost.

The boundary integral method is used instead of classical spherical bubble theory, such as the Keller-Miksis equation (Keller and Miksis [1980]), since non-linear behaviour can arise when the bubble is subject to an acoustic wave or near to a rigid boundary. Hence, the bubble develops non-spherical oscillations and can no longer be accurately predicted by a spherical model. Now, the discretisation, interpolation and numerical treatment of the bubble surface and boundary integral equation will be described.

2.2.2 Discretisation of the Surface of the Bubble

The bubble surface, ∂S, is discretised into N segments with $N+1$ nodes. Each segment is labelled S_j with $j = 1, \ldots, N$. This is represented in figure 2.3.

Note that the numbering of the nodes arbitrarily begins at the bottom of the bubble, and the coordinates of each node are defined as (r_j, z_j) for $j = 1, \ldots, N+1$. The top and bottom nodes always remain on the axis of symmetry. The number of segments N is arbitrarily chosen in a balance between accuracy and computational time, with the number of nodes required determined by convergence testing. Given that the bubble is axisymmetric about the z axis, integration through the polar angle represents the entire three dimensional bubble.

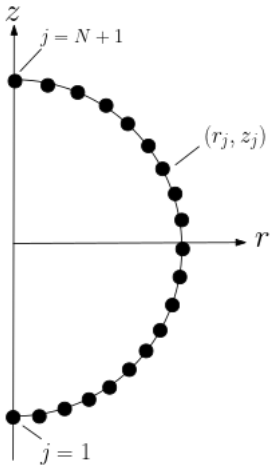

Figure 2.3: The surface of an axisymmetric bubble discretised into N segments S_j, with $N + 1$ nodes

The surface of the bubble must now be interpolated to provide an approximation of the intermediate values between nodes. Cubic splines are the chosen method of interpolation.

2.2.3 Cubic Spline Interpolation of Surface Variables and Potential

Cubic splines are a helpful tool for interpolating large data sets, since they avoid high order polynomial approximations. Instead of fitting one curve to the data set, many curves are used. Each segment between data points has a curve fit to it, with each polynomial restricted to cubic order. This approach has the benefit of low interpolation error without the need for a high order polynomial. This also means that Runge's phenomenon is avoided, in which unwanted oscillation occurs between data points. In order for the interpolation of the complete data set to have low error, it is required that the interpolation is smooth. To ensure this, the first and second derivatives of adjacent splines must be equal at each node.

In order to interpolate the surface position variables and potential of the bubble as in Popinet and Zaleski [2002], one dimensional cubic splines are used. Each variable is parametrised in terms of the arc-length ξ. At each node j, the value of the r coordinate

r_j, z coordinate z_j, and potential ϕ_j are known, as well as the cumulative arc-length ξ_j up to the node. Clamped splines are used for both the potential ϕ and z, with data sets $\{\phi_1, \ldots, \phi_{N+1}\}$ and $\{z_1, \ldots, z_{N+1}\}$ respectively. Natural splines are used for the value of the r coordinate, with data set $\{r_1, \ldots, r_{N+1}\}$. The data sets ϕ_i, r_i, and z_i replace the values of y_i in the matrix systems derived in Appendix A, (A.0.32) for natural splines and (A.0.38) for clamped splines. Thus the potential, r coordinate, and z coordinate can be completely described on the surface of the bubble via cubic spline interpolation. Note that the normal derivative $\partial\phi/\partial n$ is represented linearly with respect to arc-length, rather than by a cubic splines, due to the complexity of the matrix system that will arise.

2.2.4 Simplifying the Boundary Integral Equation for an Axisymmetric Bubble

Now that the discretisation and interpolation of the bubble surface variables have been defined, the boundary integral equation can be simplified for an axisymmetric bubble. Simplifications to the boundary integral equation given axisymmetry have been previously described (Taib [1985], Lind [2010]).

For an axisymmetric bubble near to a rigid boundary, the field points are represented by $\mathbf{r} = (r_0, 0, z_0)$ and the source points, after transformation to cylindrical polar coordinates, are given by $\mathbf{q} = (r\cos\theta, r\sin\theta, z)$ and $\mathbf{q}_{im} = (r\cos\theta, r\sin\theta, -z)$. Thus, the Greens function can be written

$$G(\mathbf{r}, \mathbf{q}) = \frac{1}{[(r\cos\theta - r_0)^2 + (r\sin\theta)^2 + (z - z_0)^2]^{\frac{1}{2}}} + \frac{1}{[(r\cos\theta - r_0)^2 + (r\sin\theta)^2 + (z + z_0)^2]^{\frac{1}{2}}}, \tag{2.2.1}$$

or equivalently using utilising a half angle formula

$$G(\mathbf{r},\mathbf{q}) = \left[(r+r_0)^2 + (z-z_0)^2 - 4rr_0\cos^2\left(\frac{\theta}{2}\right)\right]^{-\frac{1}{2}} + \left[(r+r_0)^2 + (z+z_0)^2 - 4rr_0\cos^2\left(\frac{\theta}{2}\right)\right]^{-\frac{1}{2}}. \tag{2.2.2}$$

For simplicity, this can be written $G(\mathbf{r},\mathbf{q}) = G_1(\mathbf{r},\mathbf{q}) + G_2(\mathbf{r},\mathbf{q})$, where $G_1(\mathbf{r},\mathbf{q})$ is the Greens function in free space and $G_2(\mathbf{r},\mathbf{q})$ is the amendment to the Greens function to include a rigid boundary.

Now, the boundary integral equation is discretised to make appropriate simplifications. Given the discretisation from Section 2.2.2, and the parametrisation of the surface variables by the arc-length such that $r = r(\xi)$, $z = z(\xi)$, and $\phi = \phi(\xi)$, the boundary integral equation can be written in the form

$$\begin{aligned} c(\mathbf{r}_i)\phi(\mathbf{r}_i) = &\sum_{j=1}^{N}\int_{\xi_j}^{\xi_{j+1}} \frac{\partial\phi}{\partial n}(\xi)\left(\int_0^{2\pi} G(\mathbf{r}_i,\xi,\theta)J(\xi,\theta)d\theta\right)\mathrm{d}\xi \\ &- \sum_{j=1}^{N}\int_{\xi_j}^{\xi_{j+1}} \phi(\xi)\left(\int_0^{2\pi} \frac{\partial G}{\partial n}(\mathbf{r}_i,\xi,\theta)J(\xi,\theta)d\theta\right)\mathrm{d}\xi, \end{aligned} \tag{2.2.3}$$

where $i = 1,\ldots,N+1$, and $J(\xi,\theta)$ is the Jacobian following the parametrisation. The boundary integral equation has been broken up into integrals over the N segments of the surface of the bubble, which are summed together to represent the whole of the surface. The surface variables $\phi(\xi)$, $r(\xi)$, and $z(\xi)$ are represented by the cubic spline interpolation in each segment, as defined in Section 2.2.3. The surface of the bubble S is projected into two dimensions, ξ and θ, such that $\mathrm{d}S = J(\xi,\theta)\ \mathrm{d}\xi\mathrm{d}\theta$. The Jacobian of the coordinate transform is then defined by $J(\xi,\theta) = |\mathbf{r}_\xi \times \mathbf{r}_\theta|$, where $\mathbf{r} = r(\xi)\cos\theta\widehat{\mathbf{i}} + r(\xi)\sin\theta\widehat{\mathbf{j}} + z(\xi)\widehat{\mathbf{k}}$

describes the vector coordinates of any arbitrary point in the fluid domain. Hence,

$$\mathbf{r}_\xi = \frac{dr}{d\xi}(\xi)\cos\theta\widehat{\mathbf{i}} + \frac{dr}{d\xi}(\xi)\sin\theta\widehat{\mathbf{j}} + \frac{dz}{d\xi}(\xi)\widehat{\mathbf{k}}, \tag{2.2.4}$$

$$\mathbf{r}_\theta = -r(\xi)\sin\theta\widehat{\mathbf{i}} + r(\xi)\cos\theta\widehat{\mathbf{j}}, \tag{2.2.5}$$

and after taking the modulus of the cross product of these two vectors, the Jacobian is given by

$$J(\xi) = r(\xi)\sqrt{\left(\frac{dz}{d\xi}\right)^2 + \left(\frac{dr}{d\xi}\right)^2}. \tag{2.2.6}$$

Now, the integrals in equation (2.2.3) can be simplified, upon substitution of the Jacobian and Greens function.

There are two integrals in equation (2.2.3) that can be analytically calculated. These are labelled A_i and B_i, with

$$A_i = A_{i1} + A_{i2} = \int_0^{2\pi} G_1(\mathbf{r}_i, \xi, \theta)J(\xi)\ \mathrm{d}\theta + \int_0^{2\pi} G_2(\mathbf{r}_i, \xi, \theta)J(\xi)\ \mathrm{d}\theta, \tag{2.2.7}$$

$$B_i = B_{i1} + B_{i2} = \int_0^{2\pi} \frac{\partial G_1}{\partial n}(\mathbf{r}_i, \xi, \theta)J(\xi)\ \mathrm{d}\theta + \int_0^{2\pi} \frac{\partial G_2}{\partial n}(\mathbf{r}_i, \xi, \theta)J(\xi)\ \mathrm{d}\theta. \tag{2.2.8}$$

Using the definitions of the Greens function and Jacobian, A_{i1} can be written

$$A_{i1} = \frac{J(\xi)}{\left[(r+r_i)^2 + (z-z_i)^2\right]^{\frac{1}{2}}} \int_0^{2\pi} \frac{\mathrm{d}\theta}{\left[1 - k_1^2(\xi)\cos^2\left(\frac{\theta}{2}\right)\right]^{\frac{1}{2}}}, \tag{2.2.9}$$

where

$$k_1^2(\xi) = \frac{4r(\xi)r_i}{(r(\xi)+r_i)^2 + (z(\xi)-z_i)^2}. \tag{2.2.10}$$

Setting $\alpha = \theta/2$, the integral becomes

$$\int_0^{2\pi} \frac{\mathrm{d}\theta}{\left[1 - k_1^2\cos^2\left(\frac{\theta}{2}\right)\right]^{\frac{1}{2}}} = 2\int_0^{\pi} \frac{\mathrm{d}\alpha}{\left[1 - k_1^2\cos^2\alpha\right]^{\frac{1}{2}}} = 4\int_0^{\frac{\pi}{2}} \frac{\mathrm{d}\alpha}{\left[1 - k_1^2\cos^2\alpha\right]^{\frac{1}{2}}}, \tag{2.2.11}$$

due to the symmetry of the function over the range $(0, \pi)$. Over the region $(0, \pi/2)$, sine and cosine in the integral are equivalent as they are symmetric about the midpoint $\pi/4$. This is beneficial as now the integral can now be written

$$4\int_0^{\frac{\pi}{2}} \frac{\mathrm{d}\alpha}{[1-k_1^2\cos^2\alpha]^{\frac{1}{2}}} = 4\int_0^{\frac{\pi}{2}} \frac{\mathrm{d}\alpha}{\left[1-k_1^2\sin^2\alpha\right]^{\frac{1}{2}}} = 4K(k_1), \tag{2.2.12}$$

where, $K(k_1)$ is the complete elliptic integral of the first kind. This elliptic integral has a known polynomial approximation. The calculation of A_{i2} follows similarly, with

$$k_2^2(\xi) = \frac{4r(\xi)r_i}{(r(\xi)+r_i)^2+(z(\xi)+z_i)^2}. \tag{2.2.13}$$

Subsequently, A_i is now a function of ξ with no θ dependence as desired, and takes the form

$$A_i(\xi) = \frac{4r(\xi)\sqrt{\left(\frac{dz}{d\xi}\right)^2+\left(\frac{dr}{d\xi}\right)^2}K(k_1)}{[(r(\xi)+r_i)^2+(z(\xi)-z_i)^2]^{\frac{1}{2}}} + \frac{4r(\xi)\sqrt{\left(\frac{dz}{d\xi}\right)^2+\left(\frac{dr}{d\xi}\right)^2}K(k_2)}{[(r(\xi)+r_i)^2+(z(\xi)+z_i)^2]^{\frac{1}{2}}}. \tag{2.2.14}$$

For the calculation of B_i, the normal derivative of the Greens function must first be found. The normal derivative of the Greens function is defined as

$$\frac{\partial G}{\partial n}(\mathbf{r},\mathbf{q}) = \nabla G(\mathbf{r},\mathbf{q})\cdot\widehat{\mathbf{n}}, \tag{2.2.15}$$

where $\widehat{\mathbf{n}}$ is the outward facing normal to the surface. For the parametrised surface, this is defined as

$$\widehat{\mathbf{n}} = \frac{\mathbf{r}_\xi \times \mathbf{r}_\theta}{|\mathbf{r}_\xi \times \mathbf{r}_\theta|}. \tag{2.2.16}$$

Using the definition of $\mathbf{r}_\xi$ and $\mathbf{r}_\theta$ from (2.2.4) and (2.2.5) respectively, the normal vector can be written

$$\widehat{\mathbf{n}} = \frac{1}{J(\xi)}\left(r(\xi)\cos\theta\frac{dz}{d\xi}, r(\xi)\sin\theta\frac{dz}{d\xi}, -r(\xi)\frac{dr}{d\xi}\right). \tag{2.2.17}$$

Taking the gradient of the $G_1(\mathbf{r}_i, \xi, \theta)$ (2.2.2) yields

$$\nabla G_1(\mathbf{r}_i, \xi, \theta) = -G_1(\mathbf{r}_i, \xi, \theta)^3\left(r(\xi)\cos\theta - r_i, r(\xi)\sin\theta, z(\xi) - z_i\right). \tag{2.2.18}$$

Hence, after taking the dot product of (2.2.18) and (2.2.17)

$$\frac{\partial G_1}{\partial n} = \frac{r(\xi)G_1(\mathbf{r}_i, \xi, \theta)^3}{J(\xi)}\left(\frac{dz}{d\xi}\left(r_i\cos\theta - r(\xi)\right) + \frac{dr}{d\xi}(z(\xi) - z_i)\right). \tag{2.2.19}$$

Upon substitution of (2.2.19) into B_{i1},

$$B_{i1} = \int_0^{2\pi} r(\xi)G_1(\mathbf{r}_i, \xi, \theta)^3\left(\frac{dz}{d\xi}\left(r_i\cos\theta - r(\xi)\right) + \frac{dr}{d\xi}(z(\xi) - z_i)\right)\mathrm{d}\theta, \tag{2.2.20}$$

which can be rearranged finding

$$\begin{aligned} B_{i1} = -\Bigg[&r(\xi)\left(\frac{dz}{d\xi}r(\xi) + \frac{dr}{d\xi}(z_i - z(\xi))\right)\int_0^{2\pi} G_1(\mathbf{r}_i, \xi, \theta)^3\mathrm{d}\theta \\ &-r(\xi)\frac{dz}{d\xi}\int_0^{2\pi} G_1(\mathbf{r}_i, \xi, \theta)^3 r_i\cos\theta\ \mathrm{d}\theta\Bigg]. \end{aligned} \tag{2.2.21}$$

Using the definition of $G_1(\mathbf{r}_i, \xi, \theta)$ and $k_1^2(\xi)$ from (2.2.10), upon substitution, yields

$$\begin{aligned} B_{i1} = -\Bigg[&\frac{r(\xi)\left(\frac{dz}{d\xi}r(\xi) + \frac{dr}{d\xi}(z_i - z(\xi))\right)}{((r(\xi) + r_i)^2 + (z(\xi) - z_i)^2)^{\frac{3}{2}}}\int_0^{2\pi}\frac{\mathrm{d}\theta}{\left[1 - k_1^2\cos^2\frac{\theta}{2}\right]^{\frac{3}{2}}} \\ &- r(\xi)\frac{dz}{d\xi}\frac{r_i}{((r(\xi) + r_i)^2 + (z(\xi) - z_i)^2)^{\frac{3}{2}}}\int_0^{2\pi}\frac{\cos\theta}{\left[1 - k_1^2\cos^2\frac{\theta}{2}\right]^{\frac{3}{2}}}\mathrm{d}\theta\Bigg]. \end{aligned} \tag{2.2.22}$$

The two integrals in (2.2.22) are defined to be I_1 and I_2, with

$$I_1 = \int_0^{2\pi} \frac{\mathrm{d}\theta}{\left[1 - k_1^2 \cos^2 \frac{\theta}{2}\right]^{\frac{3}{2}}} \text{ and } I_2 = \int_0^{2\pi} \frac{\cos\theta}{\left[1 - k_1^2 \cos^2 \frac{\theta}{2}\right]^{\frac{3}{2}}} \mathrm{d}\theta. \tag{2.2.23}$$

Considering I_1, setting $\alpha = \theta/2$, and noting the symmetry of the integral,

$$I_1 = 4 \int_0^{\frac{\pi}{2}} \frac{\mathrm{d}\alpha}{\left[1 - k_1^2 \cos^2 \alpha\right]^{\frac{3}{2}}}. \tag{2.2.24}$$

Noticing that sine and cosine are equivalent when integrated over this region,

$$I_1 = \int_0^{\frac{\pi}{2}} \frac{\mathrm{d}\alpha}{\left[1 - k_1^2 \sin^2 \alpha\right]^{\frac{3}{2}}} = 4\Pi(k, k). \tag{2.2.25}$$

Here $\Pi(k, k)$ is the complete elliptic integral of the third kind. Moving on to consider I_2, using simple trigonometric identities receives

$$I_2 = \int_0^{2\pi} \frac{\cos\theta}{\left[1 - k_1^2 \cos^2 \frac{\theta}{2}\right]^{\frac{3}{2}}} \mathrm{d}\theta = \int_0^{2\pi} \frac{2\cos^2 \frac{\theta}{2} - 1}{\left[1 - k_1^2 \cos^2 \frac{\theta}{2}\right]^{\frac{3}{2}}} \mathrm{d}\theta. \tag{2.2.26}$$

Setting $\eta = \theta/2$, and noticing the symmetry of the function, this is equal to

$$I_2 = 4 \int_0^{\frac{\pi}{2}} \frac{2\cos^2 \eta - 1}{\left[1 - k_1^2 \cos^2 \eta\right]^{\frac{3}{2}}} \mathrm{d}\eta = \frac{8}{k^2} \int_0^{\frac{\pi}{2}} \frac{k_1^2 \cos^2 \eta - \frac{1}{2}k^2}{\left[1 - k^2 \cos^2 \eta\right]^{\frac{3}{2}}} \mathrm{d}\eta. \tag{2.2.27}$$

$$= \frac{8}{k_1^2} \int_0^{\frac{\pi}{2}} \frac{k_1^2 \cos^2 \eta - 1}{\left[1 - k_1^2 \cos^2 \eta\right]^{\frac{3}{2}}} + \frac{-\frac{1}{2}k_1^2 + 1}{\left[1 - k_1^2 \cos^2 \eta\right]^{\frac{3}{2}}} \mathrm{d}\eta. \tag{2.2.28}$$

$$= \left(\frac{8}{k_1^2} - 4\right) \int_0^{\frac{\pi}{2}} \frac{\mathrm{d}\eta}{\left[1 - k_1^2 \sin^2 \eta\right]^{\frac{3}{2}}} - \frac{8}{k_1^2} \int_0^{\frac{\pi}{2}} \frac{\mathrm{d}\eta}{\left[1 - k_1^2 \sin^2 \eta\right]^{\frac{1}{2}}}. \tag{2.2.29}$$

$$= \left(\frac{8}{k_1^2} - 4\right)\Pi(k_1, k_1) - \frac{8}{k_1^2}K(k_1), \tag{2.2.30}$$

where $\Pi(k_1, k_1)$ and $K(k_1)$ are the complete elliptic integrals of the third and first kind respectively. Note that

$$\Pi(k_1, k_1) = \frac{E(k_1)}{1 - k_1^2}, \tag{2.2.31}$$

where $E(k_1)$ is the complete elliptic integral of the second kind. Both the complete elliptic integrals of the first and second kind can be approximated by the use of tabulated polynomials. Substituting I_1 and I_2 back into B_{i1}, and following the same procedure to find B_{i2}, yields

$$\begin{aligned} B_i(\xi) = -4\frac{r(\xi)}{[(r(\xi)+r_i)^2 + (z(\xi)-z_i)^2]^{\frac{3}{2}}}\Bigg[\Bigg(\frac{dz}{d\xi}(r(\xi)+r_i) - \frac{dr}{d\xi}(z(\xi)-z_i) \\ -\frac{2}{k_1^2}\frac{dz}{d\xi}r_i\Bigg)\frac{E(k_1)}{1-k_1^2} + r_i\frac{dz}{d\xi}\frac{2}{k_1^2}K(k_1)\Bigg] + \\ -4\frac{r(\xi)}{[(r(\xi)+r_i)^2 + (z(\xi)+z_i)^2]^{\frac{3}{2}}}\Bigg[\Bigg(\frac{dz}{d\xi}(r(\xi)+r_i) - \frac{dr}{d\xi}(z(\xi)+z_i) \\ -\frac{2}{k_2^2}\frac{dz}{d\xi}r_i\Bigg)\frac{E(k_2)}{1-k_2^2} + r_i\frac{dz}{d\xi}\frac{2}{k_2^2}K(k_2)\Bigg]. \end{aligned} \tag{2.2.32}$$

All of the above terms can be calculated from the interpolated surface variables, and there is no dependence on θ as required. The elliptic integrals are given by

$$\begin{cases} K(k_i) = P(x_i) - Q(x_i)\ln(x_i), \\ E(k_i) = R(x_i) - S(x_i)\ln(x_i), \end{cases} \tag{2.2.33}$$

for $i = 1, 2$, where $x = 1 - k_i^2(\xi)$, and P, Q, R, S are known, tabulated polynomials (Hastings [1955]). Given the definition of the elliptic integrals, note that a logarithmic singularity arises in the case that $k_1^2(\xi) = 1$. This case requires special treatment.

2.2.5 Treatment of Logarithmic Singularities

In order to treat the singularity that arises, the conditions leading to $k_1^2(\xi) = 1$ must be identified. Recalling that

$$k_1^2(\xi) = \frac{4r(\xi)r_i}{(r(\xi) + r_i)^2 + (z(\xi) - z_i)^2}, \tag{2.2.34}$$

it is clear that $k_1^2(\xi) = 1$ only if $z(\xi) = z_i$ and thus $r(\xi) = r_i$. This means that the singularity only occurs when the source point (r_i, z_i) lies within the segment that is being integrated over. It is for this reason that the source points are chosen to be the nodes on the bubble surface. There are several beneficial reasons for this. Firstly, there are only two singularities that can arise over a segment, which occur at the end-points. The treatment for these singularities is the same for all of the segments on the bubble surface, which is significantly simpler than having to deal with singularities located at arbitrary points within the segment. Secondly, the potential at the nodes is known and does not have to be calculated from the interpolated potential over the surface. Calculating the potential at the midpoint of the segment, for example, would introduce error from interpolation. Finally, there are $N + 1$ nodes on the surface of the bubble, and so there are $N + 1$ unknown values of the normal derivative of the potential. Then by choosing the source point to be each of the nodes, we have $N + 1$ equations from the system (2.2.3). The resulting system then has enough information to be solved for the normal derivative of the potential at each node.

Now, we need to consider the treatment of the singularity for the two occasions it could occur: when the source point is located at the beginning of a segment or the end. Consider the segment j, with $\xi_j \leqslant \xi \leqslant \xi_{j+1}$. The singularity occurs at the start of the segment if $(r_i, z_i) = (r(\xi_j), z(\xi_j))$, or the end of the segment if $(r_i, z_i) = (r(\xi_{j+1}), z(\xi_{j+1}))$. First, the case with the singularity arising at $(r_i, z_i) = (r(\xi_j), z(\xi_j))$ will be considered.

To begin, the logarithms in (2.2.33) are re-written, where $x_1 = 1 - k_1^2(\xi)$, so that

$$\log(x_1) = \log\left(\frac{x_1}{((\xi - \xi_j)/\Delta\xi_j)^2}\right) + 2\log\left(\frac{\xi - \xi_j}{\Delta\xi_j}\right), \tag{2.2.35}$$

where $\Delta\xi_j = \xi_{j+1} - \xi_j$. Note that from (2.2.3)

$$c(\mathbf{r}_i)\phi(\mathbf{r}_i) = \sum_{j=1}^{N} \int_{\xi_j}^{\xi_{j+1}} \frac{\partial\phi}{\partial n}(\xi) A_i(\xi)\, \mathrm{d}\xi - \sum_{j=1}^{N} \int_{\xi_j}^{\xi_{j+1}} \phi(\xi) B_i(\xi)\, \mathrm{d}\xi, \tag{2.2.36}$$

where

$$A_{i1}(\xi) = \frac{4r(\xi)M(\xi)}{D(\xi)} K(k_1(\xi)), \tag{2.2.37}$$

$$B_{i1}(\xi) = -\frac{4r(\xi)}{D(\xi)^3}\left[\left(\frac{dz}{d\xi}(r(\xi) + r_i) - \frac{dr}{d\xi}(z(\xi) - z_i) - \frac{2}{k_1^2}\frac{dz}{d\xi} r_i\right)\frac{E(k_1)}{1 - k_1^2} + r_i \frac{dz}{d\xi}\frac{2}{k_1^2} K(k_1)\right], \tag{2.2.38}$$

upon defining

$$M(\xi) = \sqrt{\left(\frac{dr}{d\xi}\right)^2 + \left(\frac{dz}{d\xi}\right)^2} \quad \text{and} \quad D(\xi) = \left((r + r_i)^2 + (z - z_i)^2\right)^{\frac{1}{2}}. \tag{2.2.39}$$

Using (2.2.33) and (2.2.35) we can write

$$\begin{aligned}\int_{\xi_j}^{\xi_{j+1}} \frac{\partial\phi}{\partial n} A_{i1}(\xi)\mathrm{d}\xi = 4\Bigg\{ &\int_{\xi_j}^{\xi_{j+1}} \frac{\partial\phi}{\partial n}\frac{r(\xi)}{D(\xi)}\left[P(x_1(\xi)) - Q(x_1)\log\left(\frac{x_1(\xi)}{((\xi - \xi_j)/\Delta\xi_j)^2}\right)\right] M(\xi)\mathrm{d}\xi \\ &+ 2\int_{\xi_j}^{\xi_{j+1}} \frac{\partial\phi}{\partial n}\frac{r(\xi)}{D(\xi)} Q(x_i(\xi))\log\left(\frac{1}{(\xi - \xi_j)/\Delta\xi_j}\right) M(\xi)\mathrm{d}\xi\Bigg\},\end{aligned} \tag{2.2.40}$$

$$\int_{\xi_j}^{\xi_{j+1}} \phi(\xi) B_{i1}(\xi) \mathrm{d}\xi = -\int_{\xi_j}^{\xi_{j+1}} \phi(\xi) \frac{4r(\xi)}{D(\xi)^3} \left\{ \frac{R(x_1(\xi)) - S(x_1) \log\left(\frac{x_1(\xi)}{((\xi-\xi_j)/\Delta\xi_j)^2}\right)}{1-k_1^2(\xi)} \left(\frac{dz}{d\xi}(r(\xi)+ r_i) - \frac{dr}{d\xi}(z(\xi)-z_i) - \frac{2}{k_1^2}\frac{dz}{d\xi} r_i \right) + 2\frac{dz}{d\xi}\frac{r_i}{k_1^2} \left[P(x_1(\xi)) - Q(x_1(\xi)) \log\left(\frac{x_1(\xi)}{((\xi-\xi_j)/\Delta\xi_j)^2}\right) \right] \right\} \mathrm{d}\xi - 8\int_{\xi_j}^{\xi_{j+1}} \phi(\xi) \frac{r(\xi)}{D(\xi)^3} \left\{ \frac{S(x_1(\xi))}{1-k_1^2} \left(\frac{dz}{d\xi}(r(\xi)+r_i) - \frac{dr}{d\xi}(z(\xi)-z_i) - \frac{2}{k_1^2}\frac{dz}{d\xi} r_i \right) + 2\frac{dz}{d\xi}\frac{r_i}{k_1^2} Q(x_1(\xi)) \right\} \log\left(\frac{1}{(\xi-\xi_j)/\Delta\xi_j}\right) \mathrm{d}\xi. \tag{2.2.41}$$

Note that the first integral in each case does not include a logarithmic singularity, which has been removed to the second integral. The singularity can be removed since in the neighbourhood of $\xi = \xi_j$, Taylor expansion gives

$$r(\xi) = r_i + (\xi - \xi_j)\frac{dr}{d\xi} + (\xi-\xi_j)^2 \frac{d^2 r}{d\xi^2} + \dots \,, \tag{2.2.42}$$

$$z(\xi) = z_i + (\xi - \xi_j)\frac{dz}{d\xi} + (\xi-\xi_j)^2 \frac{d^2 z}{d\xi^2} + \dots \,, \tag{2.2.43}$$

and so

$$1 - k_1^2(\xi) = x \approx \frac{(\xi-\xi_j)^2}{4r_i^2} \left[\left(\frac{dr}{d\xi}\right)^2 + \left(\frac{dz}{d\xi}\right)^2 \right] = A(\xi-\xi_j)^2. \tag{2.2.44}$$

Therefore

$$\log\left(\frac{x}{(\xi-\xi_j)^2/\Delta\xi_j}\right) \approx \log(A\Delta\xi_j), \tag{2.2.45}$$

which can be calculated. In both cases the first integral can be calculated using 16 point Gauss-Legendre quadratures, in a process that will be detailed later. The integrals containing the logarithmic singularity can be calculated using a tabulated quadrature

scheme from Stroud and Secrest [1966] for integrals of the form

$$\int_0^1 f(x) \log\left(\frac{1}{x}\right) dx. \tag{2.2.46}$$

The singularity that occurs when $(r_i, z_i) = (r(\xi_{j+1}), z(\xi_{j+1}))$ can be treated similarly, instead writing

$$\log(x_1) = \log\left(\frac{x_1}{((\xi_{j+1} - \xi)/\Delta\xi_j)^2}\right) + 2\log\left(\frac{\xi_{j+1} - \xi}{\Delta\xi_j}\right). \tag{2.2.47}$$

Using this method of removing the singularity, we ensure that the integrals in the system can be computed for all of the source points. This means that the system can be solved.

2.2.6 Solving the Resulting System of Equations

The system of $N + 1$ equations can now be defined. We can write, following (2.2.36),

$$c(\mathbf{r}_i)\phi(\mathbf{r}_i) + \sum_{j=1}^{N} \alpha_{ij} = \sum_{j=1}^{N} \left(\beta_{ij} \frac{\partial \phi_j}{\partial n} + \gamma_{ij} \frac{\partial \phi_{j+1}}{\partial n}\right), \tag{2.2.48}$$

for $i = 1, \ldots, N + 1$. Here, we have used a linear representation for the normal derivative of the potential following Wang and Blake [2010], and

$$\alpha_{ij} = \int_{\xi_j}^{\xi_{j+1}} \phi_j(\xi) A_i(\xi)\, \mathrm{d}\xi, \tag{2.2.49}$$

$$\beta_{ij} = \int_{\xi_j}^{\xi_{j+1}} \frac{\xi_{j+1} - \xi}{\Delta\xi_j} B_i(\xi)\, \mathrm{d}\xi, \tag{2.2.50}$$

$$\gamma_{ij} = \int_{\xi_j}^{\xi_{j+1}} \frac{\xi - \xi_j}{\Delta\xi_j} B_i(\xi)\, \mathrm{d}\xi. \tag{2.2.51}$$

These three integrals are approximated using 16 point Gauss-Legendre quadratures. The logarithmic singularities that occur are treated with 16 point quadratures as mentioned

before. The integrand is calculated at each abscissae using the cubic spline approximation of ϕ, and the derived formulas for A_i and B_i. The abscissae and weights are calculated for each domain $[\xi_j, \xi_{j+1}]$ using standard tabulated formulae.

In order to solve the system for the normal derivative of potential, it must be reformulated. For simplicity, we define $\frac{\partial \phi_j}{\partial n}(\xi) = \psi_j(\xi)$. As discussed earlier, the field points $\mathbf{r}_i$ will always be taken to be the nodes on the bubble surface, and so the solid angle formula $c(\mathbf{r}_i) = 2\pi$. Hence, the lone potential term can incorporated into the sum given the definition $c(\mathbf{r}_i)\phi(\mathbf{r}_i) = 2\pi\phi(\mathbf{r}_j)\delta_{ij}$, where δ_{ij} is the Kronecker delta. Then we have the system of equations given by

$$\sum_{j=1}^{N} C_{ij} = \sum_{j=1}^{N+1} D_{ij}\psi_j, \tag{2.2.52}$$

for $i = 1, \ldots, N+1$, where

$$C_{ij} = 2\pi\phi_j(\xi)\delta_{ij} + \alpha_{ij}, \tag{2.2.53}$$

$$D_{ij} = \beta_{ij} + \gamma_{i(j-1)}, \tag{2.2.54}$$

defining $\gamma_{i(j-1)} = 0$ when $j = 1$, and $\beta_{ij} = 0$ when $j = N+1$. This can be written in matrix form as

$$\mathbf{D} \cdot \mathbf{\Psi} = \mathbf{C}, \tag{2.2.55}$$

where $\mathbf{D}$ is a matrix with $N+1$ rows and $N+1$ columns, where each element is known, $\mathbf{\Psi}$ is a column vector with $N+1$ unknowns, representing the normal derivative of potential, and $\mathbf{C}$ is a column vector with $N+1$ known elements. Then, by performing Gaussian elimination on the system, we can solve to find $\mathbf{\Psi}$. Thus, we have found the normal derivative of the potential, ψ_j, on each node of the bubble surface.

2.2.7 Lagrangian Time Integration

The process for calculating the normal derivative of the potential at each node on the bubble surface has been detailed. Now, we can approximate the behaviour of the bubble

over time using the kinematic and dynamic boundary conditions. To do this, we integrate the KBC and DBC using a fourth order Runge-Kutta time stepping scheme. We choose the time step to be

$$\Delta t = \frac{\Delta\phi}{\max|D\phi/Dt|}, \tag{2.2.56}$$

where $\Delta\phi = 0.005$ is a constant chosen to limit the size of the time step (Gibson and Blake [1982]). This variable time step is chosen so that the step is smaller when the potential changes the most. This is desired since large changes in the potential correspond with high speed behaviour, meaning a smaller time step is required to capture the behaviour. The maximum change in potential is found by comparing the size of the dynamic boundary condition at each node. This is calculated at the end of each time step, at which point the value of the next time step can be calculated. Initially, the time step is equal to $\Delta\phi$.

In order to use this time stepping scheme, we need to know the initial conditions. Assuming that the bubble is initially spherical with known radius, the initial surface nodes are easily found. If the bubble has initial non-dimensional radius R_0, then

$$r_j = R_0|\cos(\theta_j)|, \quad z_j = R_0\sin(\theta_j), \tag{2.2.57}$$

where θ_j, representing the angle between $z = 0$ and the line between the origin and node j, is given by

$$\theta_j = \pi\frac{j-1}{N} - \frac{\pi}{2}, \qquad \text{for } j = 1, \ldots, N+1. \tag{2.2.58}$$

This provides an equally spaced mesh on the surface of the bubble, with z ranging from $-R_0$ to R_0, and r ranging from 0 to R_0. As well as the initial coordinates of the surface, the initial potential is known. If the bubble is initially at equilibrium, then the potential distribution is assumed to be zero at each node. If the bubble is not initially at equilibrium, for example if the initial pressure is larger inside the bubble than outside, then the initial

potential $\phi_0(R_0)$ has uniform distribution (Blake and Gibson [1981]), with

$$\phi_0(R_0) = -R_0 \left[\frac{2}{3} \left(\frac{p_\infty - p_v}{\rho} \right) \left(\left(\frac{R_m}{R_0} \right)^3 - 1 \right) \right]^{\frac{1}{2}}, \tag{2.2.59}$$

where R_m is the maximum radius that the bubble would achieve in infinite space. This can be found from spherical bubble theory, such as the Rayleigh-Plesset equation. The initial potential of a bubble near to a rigid boundary is then defined

$$\phi_0(r_j, z_j) = -R_0 \left[\frac{2}{3} \left(\frac{p_\infty - p_v}{\rho} \right) \left(\left(\frac{R_m}{R_0} \right)^3 - 1 \right) \right]^{\frac{1}{2}} \left(1 + \frac{R_0}{[r_j^2 + (z_j + \gamma)^2]^{\frac{1}{2}}} \right), \tag{2.2.60}$$

where γ is the nondimensional stand-off distance between the bubble centroid and the rigid boundary (Taib [1985]). These initial conditions allow for the use of the time stepping scheme, by providing a known starting point that can be updated.

2.2.8 Updating the Kinematic Boundary Condition

When updated using the time stepping scheme, the KBC is used to update the position of the nodes of the bubble surface at each time step, and the DBC is used to update the potential at each node at each time step. As mentioned previously, we needed to find the normal derivative of potential since it represents the normal velocity in the fluid. Then, by using the tangential velocity, the velocity in the r and z directions can be calculated. We recall the KBC,

$$\left. \frac{D\mathbf{r}}{Dt} \right|_S = \nabla\phi. \tag{2.2.61}$$

Given that $\nabla\phi = \mathbf{u}$ by assumption of irrotationality, and $\mathbf{r} = (r, 0, z)$ by the assumption that the bubble is axisymmetric, we can write the discretised KBC as

$$\frac{Dr_j}{Dt} = u_{r_j}, \quad \text{and} \quad \frac{Dz_j}{Dt} = u_{z_j}, \quad \text{for} \quad j = 1, \ldots, N+1. \tag{2.2.62}$$

The velocity in the r and z direction at node j can be calculated as follows,

$$u_{r_j} = u_{\tau_j}\cos\theta_j - u_{n_j}\sin\theta_j, \quad u_{z_j} = u_{\tau_j}\sin\theta_j + u_{n_j}\cos\theta_j, \tag{2.2.63}$$

where u_{τ_j} represents the tangential velocity at node j, u_{n_j} the normal velocity at node j, and θ_j the angle between the tangent at point j and the r axis. Here, we approximate θ_j as

$$\theta_j = \arctan\left(\frac{z_{j+1} - z_{j-1}}{r_{j+1} - r_{j-1}}\right). \tag{2.2.64}$$

The coordinates (r_j, z_j) of each node on the bubble surface are known, as is the normal velocity. Hence, we just need to define the tangential velocity at each node of the bubble surface. For this, we use the central finite difference formula for a non-uniform grid (Li [2005])

$$u_{\tau_j} = \frac{\partial\phi}{\partial\xi}\Big|_{\phi=\phi_j} \approx \frac{-\Delta\xi_j}{\Delta\xi_{j-1}(\Delta\xi_{j-1}+\Delta\xi_{j+1})}\phi_{j-1} + \frac{\Delta\xi_j - \Delta\xi_{j-1}}{\Delta\xi_j\Delta\xi_{j-1}}\phi_j + \frac{\Delta\xi_{j-1}}{\Delta\xi_j(\Delta\xi_{j-1}+\Delta\xi_{j+1})}\phi_{j+1}, \tag{2.2.65}$$

for $j = 2, \ldots, N$, and recalling that $\Delta\xi_j = \xi_{j+1} - \xi_j$. We note that $u_{\tau_0} = u_{\tau_{N+1}} = 0$, since we want the points on the axis of symmetry to remain on the axis of symmetry. Thus, using (2.2.63) we can find the r and z component of the velocity at each node. Given that these are known, the kinematic boundary condition (2.2.62) can be updated in time to find the new coordinates of each node. This is only possible, however, if the potential at each time step is known. An improvement to the accuracy of the calculation of the tangential velocity could be made by directly calculating the derivative from the cubic spline interpolant of the surface. However, as the RHS of the KBC is calculated by adding the normal and tangential derivatives, the error from the normal derivative dominates. This is because the magnitude of error from the boundary integral method is significantly higher than that from a second order central difference scheme. Thus, improving this

calculation would not yield more accurate results overall.

2.2.9 Updating the Dynamic Boundary Condition

Now, it remains to consider how to evaluate the DBC in order to update the potential via the time stepping scheme. Recalling the DBC including weakly compressible and viscous effects,

$$\frac{D\phi}{Dt}\Big|_S = 1 + \frac{1}{2}|\nabla\phi|^2 + p_a \sin(kz - \omega t) - \varepsilon_p \left(\frac{V_0}{V}\right)^{\lambda} - (\delta^2 + \delta_c)(z - \gamma) + \frac{\nabla \cdot \widehat{\mathbf{n}}}{We} - \frac{2(1+C)}{Re}\frac{\partial^2\phi}{\partial n^2} + \varepsilon\frac{m_0''(t)}{2\pi}. \tag{2.2.66}$$

Given that the numerical approximation of a second derivative has higher error than a first derivative, the compressible term is incorporated into the time derivative on the left hand side. Thus at each node, it can be written (Wang and Blake [2010])

$$\frac{D}{Dt}\left(\phi_j - \varepsilon\frac{m_0'(t)}{2\pi}\right) = 1 + \frac{1}{2}|\nabla\phi_j|^2 + p_a \sin(kx_j - \omega t) - \varepsilon_p \left(\frac{V_0}{V}\right)^{\lambda} - (\delta^2 + \delta_c)(z_j - z_0) + \frac{\nabla \cdot \widehat{\mathbf{n}}_j}{We} - \frac{2(1+C)}{Re}\frac{\partial^2\phi_j}{\partial n^2}. \tag{2.2.67}$$

Now, the unknown terms in the DBC must be calculated. We start with $m_0(t)$, defined as

$$m_0(t) = \int_S \frac{\partial\phi}{\partial n} dS = \sum_{j=1}^{N} \int_{\xi_j}^{\xi_{j+1}} \frac{\partial\phi}{\partial n}(\xi) d\xi. \tag{2.2.68}$$

The normal derivative is known at each node, and so can be interpolated across the surface of the bubble using cubic splines. Then, the integral can be approximated using a 20 point Gaussian quadrature. Then to find $m_0'(t)$, a backwards finite difference scheme is employed using the value of $m_0(t)$ calculated at each time-step. Initially, this is equal to zero.

To find $|\nabla\phi_j|^2$, note that

$$|\nabla\phi_j|^2 = \left(\frac{\partial\phi_j}{\partial n}\right)^2 + u_{\tau_j}^2, \tag{2.2.69}$$

where the normal derivative of the potential is known from the boundary integral method, and the tangential velocity from the finite difference method in (2.2.65). This can then be computed using the known values at each node. The coordinates (r_j, z_j) of each node are known, as well as parameters relating to the problem, for example the pressure amplitude of the acoustic wave or the density of the liquid, meaning that the acoustic wave term and the buoyancy terms can be immediately computed. Thus, the only terms left to find are the volume V, the curvature $\nabla \cdot \widehat{\mathbf{n}}_j$, and the viscous term.

Starting with the volume of the bubble, we note that the coordinates of the nodes are known, and so the surface of the bubble can be represented by cubic spline interpolation. Then on each segment $r = f_j(\xi)$, where $f_j(\xi)$ is the cubic polynomial interpolating the r coordinate on the segment j. The volume is then given by

$$V = 2\pi\sum_{j=1}^{N}\int_{\xi_j}^{\xi_{j+1}} f_j(\xi)^2\frac{dz}{d\xi}d\xi, \tag{2.2.70}$$

where the derivative of z with respect to ξ is computed from the cubic spline interpolation of z. The integrals over each region are then approximated by use of 16 point Gaussian quadratures.

The curvature at node j, $\kappa_j = \nabla \cdot \widehat{\mathbf{n}}_j$, can be approximated using a known formula for mean curvature. The mean curvature of a point on a surface is defined as $\kappa = \kappa_1 + \kappa_2$ where κ_1 and κ_2 are the maximal and minimal curvatures respectively. These are known,

and for the node j on the bubble surface we have following Reilly [1982]

$$\nabla \cdot \widehat{\mathbf{n}}_j = \kappa_j = \frac{z_j'' r_j' - r_j''}{({r_j'}^2 + {z_j'}^2)^{\frac{3}{2}}} + \frac{z_j'}{r_j({r_j'}^2 + {z_j'}^2)^{\frac{1}{2}}}. \tag{2.2.71}$$

Here, r_j' represents the derivative of r with respect to ξ at node j, and r_j'' represents the second derivative of r with respect to ξ at node j. Again, these can be calculated from the cubic spline interpolation of r and z, upon differentiation of the known cubic polynomial.

Now, all that is left to be calculated is the viscous term. By considering Laplace's equation in boundary fitted coordinates following Lind [2010], we can say that

$$\frac{\partial^2 \phi}{\partial n^2} + \frac{\partial^2 \phi}{\partial \xi^2} - \kappa \frac{\partial \phi}{\partial n} + \frac{n_z}{r}\frac{\partial \phi}{\partial \xi} = 0. \tag{2.2.72}$$

Hence at node j, it follows from Boulton-Stone and Blake [1993] that

$$\frac{\partial^2 \phi_j}{\partial n^2} = -\frac{\partial u_{\tau_j}}{\partial \xi} + \kappa_j u_{n_j} - \frac{n_{z_j}}{r_j} u_{\tau_j}, \tag{2.2.73}$$

noting that on the axis of symmetry $r = 0$,

$$\frac{\partial^2 \phi_j}{\partial n^2} = -2\frac{\partial u_{\tau_j}}{\partial \xi} + \kappa_j u_{n_j}. \tag{2.2.74}$$

Here, the tangential velocity u_{τ_j} is known from (2.2.65), the curvature κ_j from (2.2.71), the normal derivative u_{n_j} via the boundary integral method, and the normal vector (2.2.17). The derivative of the tangential velocity with respect to arc-length is performed with a central finite difference method akin to the initial approximation of the tangential velocity in (2.2.65), with the potential replaced with the tangential velocity in the calculation. The constant term C, where

$$C = \frac{\int_S \nabla\phi \cdot \frac{\partial \nabla \phi}{\partial n} dS}{\int_S \frac{\partial \phi}{\partial n}\frac{\partial^2 \phi}{\partial n^2} dS} - 1, \tag{2.2.75}$$

is calculated as follows. For the integral on the denominator, both the normal velocity and its normal derivative have been found at each node. Then, by interpolating each using cubic splines, one can approximate the integral using 16 point Gaussian quadratures over each segment, as before. The integral on the numerator is reformulated as in Boulton-Stone and Blake [1993], such that we have

$$\int_S u_\tau \left(\frac{\partial u_n}{\partial \xi} + \kappa_1 u_\tau \right) dS, \tag{2.2.76}$$

where κ_1 is the in-plane curvature. The only unknown is the derivative of the normal velocity with respect to the arc-length, which is calculated using a central finite difference scheme, as in (2.2.65). Again, 16 point Gaussian quadratures at each segment of the bubble surface are used to approximate the integral.

The process for calculating the unknown terms of the DBC has been covered. Now, we proceed to detailing the numerical scheme used to integrate the system in time. A fourth order Runge-Kutta scheme is used to do so.

2.2.10 Fourth Order Runge-Kutta Scheme

To update the coordinates of the bubble surface and its potential at each time step, the KBC and DBC have to be integrated in time. The system then steps forwards by the time step Δt, detailed in (2.2.56). A fourth order Runge-Kutta scheme (Butcher [1963]) is used to do this.

To apply the scheme to the system, we first note that for each node j, we have a system of equations of the form

$$\frac{Dr_j}{Dt} = f_j(r, z, \phi, t), \quad \frac{Dz_j}{Dt} = g_j(r, z, \phi, t), \quad \frac{D\phi_j}{Dt} = h_j(r, z, \phi, t), \quad \text{for } j = 1, \ldots, N+1, \tag{2.2.77}$$

where (r_j, z_j) and ϕ_j are known at $t = 0$. The fourth order Runge-Kutta scheme is then defined, upon defining the time at step n as $t_n = t_0 + n\Delta t$ and $r_j(t_n) = r_j^n$,

$$r_j^{n+1} = r_j^n + \frac{1}{6}\left(k_{1_j} + 2k_{2_j} + 2k_{3_j} + k_{4_j}\right), \tag{2.2.78}$$

$$z_j^{n+1} = z_j^n + \frac{1}{6}\left(l_{1_j} + 2l_{2_j} + 2l_{3_j} + l_{4_j}\right), \tag{2.2.79}$$

$$\phi_j^{n+1} = \phi_j^n + \frac{1}{6}\left(m_{1_j} + 2m_{2_j} + 2m_{3_j} + m_{4_j}\right), \tag{2.2.80}$$

$$t_{n+1} = t_n + \Delta t, \tag{2.2.81}$$

where $j = 1, \ldots, N+1$. The following list of equations defines each unknown term:

$$k_{1_j} = \Delta t\ f_j(r_j^n, z_j^n, \phi_j^n, t_n), \tag{2.2.82}$$

$$k_{2_j} = \Delta t\ f_j(r_j^n + \frac{1}{2}k_{1_j}, z_j^n + \frac{1}{2}l_{1_j}, \phi_j^n + \frac{1}{2}m_{1_j}, t_n + \frac{1}{2}\Delta t), \tag{2.2.83}$$

$$k_{3_j} = \Delta t\ f_j(r_j^n + \frac{1}{2}k_{2_j}, z_j^n + \frac{1}{2}l_{2_j}, \phi_j^n + \frac{1}{2}m_{2_j}, t_n + \frac{1}{2}\Delta t), \tag{2.2.84}$$

$$k_{4_j} = \Delta t\ f_j(r_j^n + k_{3_j}, z_j^n + l_{3_j}, \phi_j^n + m_{3_j}, t_n + \Delta t), \tag{2.2.85}$$

$$l_{1_j} = \Delta t\ g_j(r_j^n, z_j^n, \phi_j^n, t_n), \tag{2.2.86}$$

$$l_{2_j} = \Delta t\ g_j(r_j^n + \frac{1}{2}k_{1_j}, z_j^n + \frac{1}{2}l_{1_j}, \phi_j^n + \frac{1}{2}m_{1_j}, t_n + \frac{1}{2}\Delta t), \tag{2.2.87}$$

$$l_{3_j} = \Delta t\ g_j(r_j^n + \frac{1}{2}k_{2_j}, z_j^n + \frac{1}{2}l_{2_j}, \phi_j^n + \frac{1}{2}m_{2_j}, t_n + \frac{1}{2}\Delta t), \tag{2.2.88}$$

$$l_{4_j} = \Delta t\ g_j(r_j^n + k_{3_j}, z_j^n + l_{3_j}, \phi_j^n + m_{3_j}, t_n + \Delta t), \tag{2.2.89}$$

$$m_{1_j} = \Delta t\ h_j(r_j^n, z_j^n, \phi_j^n, t_n), \tag{2.2.90}$$

$$m_{2_j} = \Delta t\ h_j(r_j^n + \frac{1}{2}k_{1_j}, z_j^n + \frac{1}{2}l_{1_j}, \phi_j^n + \frac{1}{2}m_{1_j}, t_n + \frac{1}{2}\Delta t), \tag{2.2.91}$$

$$m_{3_j} = \Delta t\ h_j(r_j^n + \frac{1}{2}k_{2_j}, z_j^n + \frac{1}{2}l_{2_j}, \phi_j^n + \frac{1}{2}m_{2_j}, t_n + \frac{1}{2}\Delta t), \tag{2.2.92}$$

$$m_{4_j} = \Delta t\ h_j(r_j^n + k_{3_j}, z_j^n + l_{3_j}, \phi_j^n + m_{3_j}, t_n + \Delta t), \tag{2.2.93}$$

for $j = 1, \ldots, N+1$. The solution strategy requires the process to be broken down into four iterations. Initially, the values of r_j^0, z_j^0, and ϕ_j^0 are known. Using the boundary integral method we find the normal derivative of the potential. As in Section 2.2.8, we use this to calculate the right-hand-side of the KBC $f_j(r_j^0, z_j^0, \phi_j^0, 0)$ and $g_j(r_j^0, z_j^0, \phi_j^0, 0)$. As in Section 2.2.9, we then calculate the right-hand-side of the DBC $h_j(r_j^0, z_j^0, \phi_j^0, 0)$. This is used to calculate the time step Δt as in (2.2.56). We then find k_{1_j}, l_{1_j}, and m_{1_j} for each $j = 1, \ldots, N+1$. The next step is to update the values of r_j, z_j, ϕ_j, and t, using

$$r_j = r_j^0 + \frac{1}{2}k_{1_j}, \quad z_j = z_j^0 + \frac{1}{2}l_{1_j}, \quad \phi_j = r_j^0 + \frac{1}{2}m_{1_j}, \quad t = 0 + \frac{1}{2}\Delta t. \tag{2.2.94}$$

Again, using these new values we use the boundary integral method to find the normal derivative of the potential, with which we compute f_j, g_j, and h_j. These are used to find k_{2_j}, l_{2_j}, and m_{2_j} for each $j = 1, \ldots, N+1$. Next, we update the values of r_j, z_j, ϕ_j, and t, using

$$r_j = r_j^0 + \frac{1}{2}k_{2_j}, \quad z_j = z_j^0 + \frac{1}{2}l_{2_j}, \quad \phi_j = r_j^0 + \frac{1}{2}m_{2_j}, \quad t = 0 + \frac{1}{2}\Delta t. \tag{2.2.95}$$

As before, we find k_{3_j}, l_{3_j}, and m_{3_j} for each $j = 1, \ldots, N+1$. Finally, we update the values of r_j, z_j, ϕ_j, and t, using

$$r_j = r_j^0 + k_{3_j}, \quad z_j = z_j^0 + l_{3_j}, \quad \phi_j = r_j^0 + m_{3_j}, \quad t = 0 + \Delta t. \tag{2.2.96}$$

Using the boundary integral method, we find find the normal derivative of potential and hence k_{4_j}, l_{4_j}, and m_{4_j} for each $j = 1, \ldots, N+1$. Thus, using (2.2.78), (2.2.79), and

(2.2.80), we can find r_j^1, z_j^1, ϕ_j^1, and t_1 for each $j = 1, \ldots, N+1$. The algorithm is then repeated with these as starting values to find r_j^2, z_j^2, ϕ_j^2, and t_2 for each $j = 1, \ldots, N+1$. This process is continued for a predefined number of steps, depending on how long the simulation is required to continue. The co-ordinates of each node are recorded at each time step to generate an image of the bubble at each step. These images are used to study the behaviour of the bubble over time.

Some numerical procedures are required to ensure the stability of the system. At each step, the surface of the bubble is re-meshed with equal arc-length in between nodes. This is done using the interpolated surface variables $r(\xi)$ and $z(\xi)$, and the total arc-length ξ_{N+1} divided into N equal segments. This prevents the nodes from "bunching up", potentially leading to instabilities. We also require some smoothing of the surface variables. In some cases there may be sharp changes in the surface variables in between nodes. This can lead to surface instabilities. To counteract this, the five point Longuet-Higgins smoothing formula is used (Longuet-Higgins and Cokelet [1976]). This is used for each surface variable, with the smoothed value of r_j, for example, given by

$$r_j^{sm} = \frac{1}{16}\left(-r_{j-2} + 4r_{j-1} + 10r_j + 4r_{j+1} - r_{j+2}\right). \tag{2.2.97}$$

This is found for each surface variable r_j, z_j, and ϕ_j for each $j = 1, \ldots, N+1$. We perform this smoothing every five to twenty time steps, as is appropriate for the situation. The number of smoothing steps is generally chosen on a case by case basis. For relatively stable oscillations as will be considered in this thesis, twenty is appropriate as surface instabilities are less likely to occur. Additionally, as the smoothing is infrequent, the effect on the results is negligible. However, for higher energy cases, the frequency of smoothing can be increased if a "saw-tooth" like instability formed on the surface of the bubble.

The numerical model for studying the evolution of a bubble over time has now been detailed.

2.3 Modelling a toroidal bubble

Considering the non-spherical oscillations of a bubble, a potential occurrence is the development of a liquid jet. This is a high speed stream of fluid with large momentum, that can travel for a long distance before dissipating. If the jet impacts on a surface, it can cause significant damage (Benjamin and Ellis [1966]). If a liquid jet forms in a bubble, it can impact the opposite surface of the bubble as seen in figure 2.4. In this case, the jet can puncture through the surface and form a toroidal bubble as seen in figure 2.5. This leads to the numerical model failing due to the potential solution becoming non-unique. Not only this, but a circulation forms around the surface of the bubble. We assume that the jet first impacts just a single point on the opposite surface, which is an idealised situation. We also assume that the initial impact of the jet does not change the bubble shape or velocity potential distribution (Best [1993]). For an axisymmetric bubble, the point of impact lies on the axis of symmetry, the z-axis, at nodes $j = 1$ and $j = N + 1$, also seen in figure 2.4. The problem that this causes is that the fluid domain is no longer simply connected, i.e. not every disc that exists in 3D-space can be shrunk down to a single point without crossing a boundary. This leads to non-uniqueness of the flow solution. Toroidal bubbles can form when a bubble oscillates in close proximity to a boundary, with a liquid jet forming directed towards the wall. This is the primary mechanism for damage, and has been shown to remove contaminants (Chahine et al. [2016]).

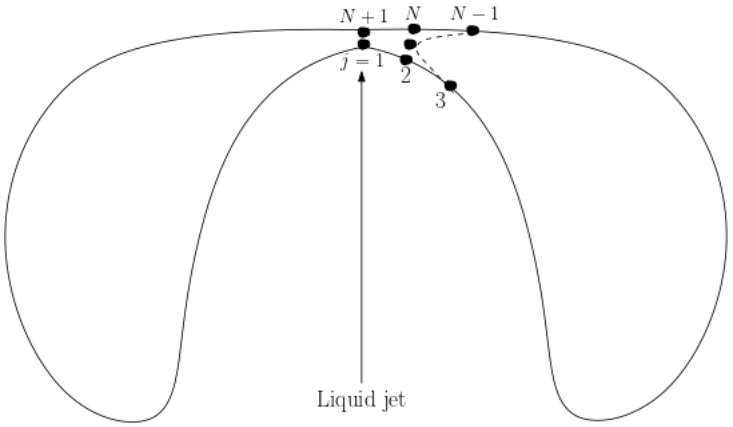

Figure 2.4: A schematic of a liquid jet impacting with the opposite bubble wall. The re-selection of nodes is also included after the jet penetrates the opposite wall.

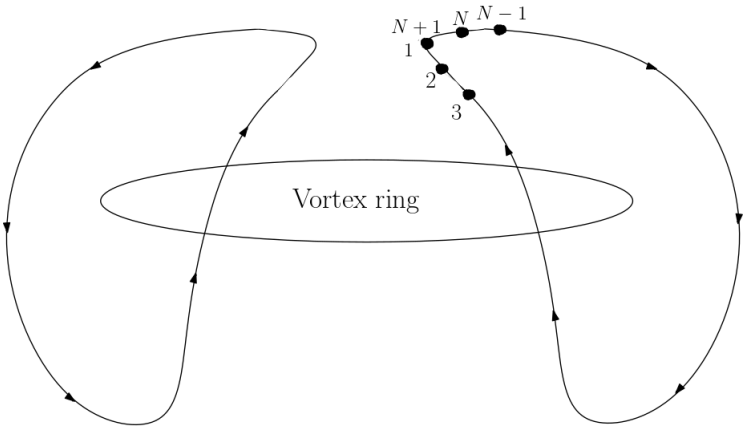

Figure 2.5: A schematic of a vortex ring placed inside a toroidal bubble, simulating the circulation around a closed path through the toroidal bubble.

The approach to deal with this problem is to artificially insert a vortex ring inside the toroidal bubble, as seen in figure 2.5. This allows us to break the problem into the unique and non-unique parts, with the non-unique flow potential analytically solvable. The vortex ring is chosen to have circulation strength Γ at the bubble surface, equal to that of the flow along any closed path that passes through the torus. This is equal to the potential jump across the contact points at the time of the collision. This is represented in the equation

$$\Gamma = \oint_C \nabla\phi \cdot d\mathbf{l} = \phi_{N+1} - \phi_1, \tag{2.3.1}$$

where ϕ_{N+1} and ϕ_1 refer to the potentials at the point of impact (Zhang et al. [1993]). Kelvin's theorem states that for an incompressible potential flow, the circulation around a closed curve moving with a fluid remains constant in time, i.e.

$$\frac{D\Gamma}{Dt} = 0. \tag{2.3.2}$$

Thus, the circulation Γ induced by the vortex ring is invariant in time.

2.3.1 Potential Due to a Vortex Ring

The potential can decomposed into two components, the potential due to the vortex ring $\psi^{vr}(r, z)$, and a single-valued remnant potential $\psi(r, z, t)$. This remnant potential is single valued, and hence has a unique flow solution. We note that the vortex ring potential contains a discontinuity, however ϕ does not. Given that the circulation due to the vortex ring is constant in time, the potential due to the vortex ring is a function of solely space, not time. It can then be written that (Wang et al. [2005])

$$\phi(r, z, t) = \psi^{vr}(r, z) + \psi(r, z, t). \tag{2.3.3}$$

The vortex ring is centered on the axis of symmetry, and is located entirely within the toroidal bubble. The exact position has no overall effect given the previous conditions are satisfied. Hence, we need to ensure that the vortex ring is not too close to the boundary of the bubble, else numerical instabilities may occur. If the vortex ring were to touch the surface of the bubble, then the condition of irrotationality would be broken in the liquid. This is due to the rotation that would occur about the vortex ring, which would also severely deform the surface such that it could no longer be tracked. To avoid this happening, if the distance between them falls to the length of one surface segment of the bubble surface, the vortex ring is re-positioned. To counteract this, we choose the initial

position of the vortex ring to be the mean position of the nodes on the bubble surface. The radius of the vortex ring, a, and position of the centre on the axis of symmetry, $z = c$, are defined by (Wang et al. [2005])

$$a = \frac{1}{N+1}\sum_{j=1}^{N+1} r_j, \quad c = \frac{1}{N+1}\sum_{j=1}^{N+1} z_j. \tag{2.3.4}$$

Then, whenever the vortex ring moves within one surface segment to the surface, we relocate the vortex ring using the same method. When the vortex ring is inserted, the remnant potential ψ needs to be calculated from (2.3.3) using the value of the vortex ring potential. This will give the initial potential distribution on the surface of the bubble, which is required for the boundary integral method. This calculation must also be performed in the incidence that the vortex ring is relocated. First we shall describe the re-discretisation of the bubble surface.

2.3.2 Re-discretisation of Bubble Surface

At the point where the jet impacts the opposite surface of the bubble, a numerical transform is required. Nodes 1 and $N + 1$, the nodes that impact each other, are removed. This allows for the transform of the singly-connected bubble to a toroidal bubble. The nodes 2 and N are moved to their mean position, and the new bubble surface is represented by the dashed line seen in figure 2.4. The remnant potential at the new position of nodes 2 and N is redefined as the mean value of potential at the previous position of the nodes. Finally, the bubble surface is re-meshed as seen in figure 2.5, with the remnant potential and surface variables re-interpolated on the new discretised surface. Note that the distance between the two sides of the bubble at the point of re-discretisation, where a segment has been removed, is the length of an element. We note that only the right-hand surface is modelled, since a rotation of 2π about the axis of symmetry would generate the toroidal bubble taking the form of a torus.

Only the remnant potential, not that due to the vortex ring, needs to be interpolated on the bubble surface given the potential due to the vortex ring can be directly calculated. The remnant potential can initially be calculated from (2.3.3), which requires the use of the potential due to the vortex ring. This can be calculated using the Biot-Savart law, an equation often used in electromagnetic field theory.

2.3.3 Biot-Savart Law

In order to calculate the potential due to a vortex ring, the Biot-Savart law must first be used to calculate the velocity field. A circular vortex ring with radius a, strength Γ, centered at the origin has velocity field given by

$$\mathbf{v}_0^{vr} = \frac{\Gamma}{4\pi} \oint_C \frac{d\mathbf{l} \times (\mathbf{r} - \mathbf{q})}{|\mathbf{r} - \mathbf{q}|^3}, \tag{2.3.5}$$

where, $\mathbf{r}$ is the field point and $\mathbf{q}$ is the source point. The curve C represents the circular vortex ring in the xy-plane. Given the axisymmetry of the problem and that the vortex ring is just a circle, the field and source points are represented by

$$\mathbf{r} = (r, 0, z), \quad \mathbf{q} = (a\cos\theta, a\sin\theta, 0). \tag{2.3.6}$$

All points of the circle C of radius a in the xy-plane, in cylindrical polar coordinates, are described by $\mathbf{q}$. Using these equations, we have:

$$\mathbf{r} - \mathbf{q} = (r - a\cos\theta)\widehat{\mathbf{i}} - a\sin\theta\widehat{\mathbf{j}} + z\widehat{\mathbf{k}}, \tag{2.3.7}$$

$$|\mathbf{r} - \mathbf{q}|^2 = (r - a\cos\theta)^2 + (a\sin\theta)^2 + z^2 = d^2 - 2ar\cos\theta, \tag{2.3.8}$$

where $d = \sqrt{r^2 + a^2 + z^2}$. Note that the vector describing the points on the circle C is given by $\mathbf{l} = (a\cos\theta, a\sin\theta, 0)$, so the line element

$$\mathrm{d}\mathbf{l} = a\mathrm{d}\theta(-\sin\theta, \cos\theta, 0). \tag{2.3.9}$$

Hence upon taking the cross product,

$$\mathrm{d}\mathbf{l} \times (\mathbf{r} - \mathbf{q}) = a\mathrm{d}\theta \begin{vmatrix} \widehat{\mathbf{i}} & \widehat{\mathbf{j}} & \widehat{\mathbf{k}} \\ -\sin\theta & \cos\theta & 0 \\ r - a\cos\theta & -a\sin\theta & z \end{vmatrix}, \tag{2.3.10}$$

$$= a\mathrm{d}\theta[z\cos\theta\widehat{\mathbf{i}} + z\sin\theta\widehat{\mathbf{j}} + (a - r\cos\theta)\widehat{\mathbf{k}}]. \tag{2.3.11}$$

The integrand from the Biot-Savart law then can be written

$$\frac{\mathrm{d}\mathbf{l} \times (\mathbf{r} - \mathbf{q})}{|\mathbf{r} - \mathbf{q}|^3} = a\frac{z\cos\theta\widehat{\mathbf{i}} + z\sin\theta\widehat{\mathbf{j}} + (a - r\cos\theta)\widehat{\mathbf{k}}}{[d^2 - 2ar\cos\theta]^{\frac{3}{2}}}\mathrm{d}\theta. \tag{2.3.12}$$

To convert to cylindrical polar coordinates, we use the substitutions given by

$$\widehat{\mathbf{r}} = \cos\theta\widehat{\mathbf{i}} + \sin\theta\widehat{\mathbf{j}}, \quad \widehat{\theta} = -\sin\theta\widehat{\mathbf{i}} + \cos\theta\widehat{\mathbf{j}}, \quad \widehat{\mathbf{k}} = \widehat{\mathbf{z}}. \tag{2.3.13}$$

Hence, we have the velocity field of the vortex ring given by

$$\mathbf{v}_0^{vr}(r, z) = \frac{\Gamma a}{4\pi}\int_0^{2\pi} \frac{z\widehat{\mathbf{r}} + (a - r\cos\theta)\widehat{\mathbf{z}}}{[d^2 - 2ar\cos\theta]^{\frac{3}{2}}}\mathrm{d}\theta = \frac{\Gamma a}{4\pi d^3}\int_0^{2\pi} \frac{z\widehat{\mathbf{r}} + (a - r\cos\theta)\widehat{\mathbf{z}}}{[1 - k\cos\theta]^{\frac{3}{2}}}\mathrm{d}\theta, \tag{2.3.14}$$

where $k = 2ar/d^2$, and $\widehat{\mathbf{r}}$ and $\widehat{\mathbf{z}}$ are the unit vectors of cylindrical polar coordinates. The r and z components of the velocity field can then be found by numerically integrating the r and z components of the integral, respectively. To do this, 16 point Gaussian quadratures

are used.

If the bubble is near a wall, the velocity field can be found using the method of images. An image of the toroidal bubble, including the vortex ring, is placed having been reflected over $z = 0$. The velocity field due to the vortex rings of radius a, strength Γ, and centres $z = c$ and $z = -c$ is given by:

$$\mathbf{v}^{vr}(r, z) = \mathbf{v}_0^{vr}(r, z - c) + \mathbf{v}_0^{vr}(r, z + c). \tag{2.3.15}$$

The two velocity fields are found upon substitution of $z = z - c$ and $z = z + c$ into (2.3.14).

2.3.4 Finding the Potential Due to a Vortex Ring

The potential due to the vortex ring can now be found using the velocity field. The potential at some point $s_j = (r_j, z_j)$ on the bubble surface can be obtained upon integration of the velocity field. Note that ψ^{vr} decays to zero at infinity. Integration of the velocity field between s_1 and s_j yields (Wang et al. [2005])

$$\psi^{vr}(r_j, z_j) = \psi^{vr}(r_1, z_1) + \int_{s_1}^{s_j} \mathbf{v}^{vr}(r, z) \cdot \mathrm{d}\mathbf{l}, \tag{2.3.16}$$

where ψ^{vr} is the potential due to the vortex ring at the point s_j. The potential at the first node of the bubble surface, $\psi^{vr}(r_1, z_1)$, is given by

$$\psi^{vr}(r_1, z_1) = \int_{-\infty}^{z_1} w^{vr}(0, z)\mathrm{d}z + \int_0^{r_1} u^{vr}(r, z_1)\mathrm{d}r, \tag{2.3.17}$$

noting that $w^{vr}(r, z)$ and $u^{vr}(r, z)$ are the z and r component of $\mathbf{v}^{vr}(r, z)$ respectively. Note that the z-component of $\mathbf{v}_0^{vr}$ at $r = 0$ is found to be

$$w^{vr}(0, z) = \frac{\Gamma a^2}{2d^3}, \tag{2.3.18}$$

and if there is a nearby wall

$$w^{vr}(0,z) = \frac{\Gamma a^2}{2\left((z-c)^2+a^2\right)^{\frac{3}{2}}} - \frac{\Gamma a^2}{2\left((z+c)^2+a^2\right)^{\frac{3}{2}}}. \tag{2.3.19}$$

Integrating, we find

$$\int_{-\infty}^{z_1} w^{vr}(0,z-c)\mathrm{d}z = \int_{-\infty}^{z_1} \frac{\Gamma a^2}{2\left((z-c)^2+a^2\right)^{\frac{3}{2}}}\mathrm{d}z, \tag{2.3.20}$$

$$= \frac{\Gamma a^2}{2}\left[\frac{1}{a^2}\frac{z-c}{\left((z-c)^2+a^2\right)^{\frac{1}{2}}}\right]_{-\infty}^{z_1} = \frac{\Gamma}{2}\left[\frac{z_1-c}{\left((z_1-c)^2+a^2\right)^{\frac{1}{2}}}+1\right]. \tag{2.3.21}$$

With the procedure following identically for $z+c$, note that in the presence of a wall

$$\int_{-\infty}^{z_1} w^{vr}(0,z)\mathrm{d}z = \frac{\Gamma}{2}\left[\frac{z_1-c}{\left((z_1-c)^2+a^2\right)^{\frac{1}{2}}} - \frac{z_1+c}{\left((z_1+c)^2+a^2\right)^{\frac{1}{2}}}\right], \tag{2.3.22}$$

and with no wall

$$\int_{-\infty}^{z_1} w^{vr}(0,z)\mathrm{d}z = \frac{\Gamma}{2}\left[\frac{z_1}{\left(z_1^2+a^2\right)^{\frac{1}{2}}}\right]. \tag{2.3.23}$$

Equations (2.3.17) and (2.3.16) can now be used to calculate the potential at any point on the bubble surface. The remaining integrals in this calculation are approximated using 16 point Gaussian quadratures.

2.3.5 Satisfaction of Laplace's Equation

Given that the fluid is assumed to be incompressible in the thin boundary layer at the surface of the bubble, we know that the velocity field of the vortex ring must satisfy Laplace's equation in the fluid, i.e. $\nabla^2\psi^{vr} = 0$. Given that the potential satisfies Laplace's equation at the surface of the bubble, $\nabla^2(\psi^{vr}+\psi) = 0$ using the definition of ϕ. Hence, the remnant potential satisfies Laplace's equation $\nabla^2\psi = 0$. We also note that the remnant potential decays to zero, since we know that both the potential and the potential due to the

vortex ring decay to zero at infinity. Given that these important properties are satisfied by both components, the remnant potential satisfies the conditions for the boundary integral method.

2.3.6 Boundary Conditions With a Vortex Ring

In order to derive the new boundary conditions for a toroidal bubble with a vortex ring, we must substitute (2.3.3) into the KBC and DBC. First note that because the potential due to a vortex ring is invariant in time, that

$$\frac{D\phi}{Dt} = \frac{D\psi}{Dt} + (\mathbf{u} \cdot \nabla)\psi^{vr}. \tag{2.3.24}$$

Since the fluid is irrotational, and again using (2.3.3), we can say that

$$\mathbf{u} = \nabla\phi = \nabla(\psi^{vr} + \psi) = \nabla\psi^{vr} + \nabla\psi. \tag{2.3.25}$$

By definition $\nabla\psi^{vr} = \mathbf{v}^{vr}$, and so

$$\frac{D\phi}{Dt} = \frac{D\psi}{Dt} + (\mathbf{v}^{vr} + \nabla\psi) \cdot \mathbf{v}^{vr}. \tag{2.3.26}$$

By simple substitution, the KBC becomes

$$\frac{D\mathbf{r}}{Dt} = \nabla\psi + \mathbf{v}^{vr}. \tag{2.3.27}$$

The DBC becomes, upon substitution of (2.3.26),

$$\frac{D}{Dt}\left(\psi - \varepsilon\frac{m_0'(t)}{2\pi}\right) = 1 - \mathbf{v}^{vr}(\mathbf{v}^{vr} + \nabla\psi) + \frac{1}{2}|\mathbf{v}^{vr} + \nabla\psi|^2 - (\delta^2 + \delta_c)(z - z_0) - \varepsilon_p\left(\frac{V_0}{V}\right)^{\lambda} + p_a\sin(kz - \omega t) + \frac{\nabla\cdot\widehat{\mathbf{n}}}{We} - \frac{2(1+C)}{Re}\frac{\partial^2}{\partial n^2}(\psi + \psi^{vr}). \tag{2.3.28}$$

This is the VCBIM model for a toroidal bubble with a vortex ring. Given that the remnant potential satisfies the relevant conditions, this model can be solved via the boundary integral method upon calculation of the vortex ring potential and velocity field. Note that if the distance between the left and right-hand sides of the bubble falls to within a pre-set distance, then the surface can be re-meshed and the bubble rejoins, so that it is no longer toroidal. This pre-set distance is chosen to be 80% of the length of a single segment of the discretised bubble surface. This value is chosen as it obtains the best agreement with experimental results.

Chapter 3

Microbubble dynamics with viscous and compressible effects, and subject to an acoustic wave

In this chapter, the weakly compressible, viscous boundary integral method is compared to theoretical and experimental results. First, it is compared to spherical bubble theory, specifically the Gilmore model, subject to an acoustic wave. Excellent agreement is achieved over multiple cycles of oscillation. Secondly, it is compared to experimental results in which a bubble is subject to a modulated acoustic wave. Due to the inclusion of viscous effects, very good agreement is achieved for both the radius history and bubble shapes. The first two results also demonstrate the ability of the BIM to accurately model many cycles of oscillation. Finally, comparisons are made with asymptotic and numerical results that demonstrate the importance of viscous and compressible effects.

3.1 Spherical Oscillations of a Bubble Subject to an Acoustic Wave

To validate the weakly compressible, viscous boundary integral method (VCBIM) subject to an acoustic wave, we compare with results from spherical bubble theory. In the works of (Lauterborn et al. [2007]), a Gilmore model was fitted to experimental results for the spherical oscillation of a bubble subject to an acoustic wave. The Gilmore model is used to predict the changing radius over time of spherical bubbles in an infinite fluid, often used for cases with large amplitude oscillations. It takes into account liquid compressibility, which is important due to the faster velocities associated with large amplitude collapse. The Gilmore equation of motion for a bubble with radius R is given by

$$R\ddot{R}\left(1-\frac{\dot{R}}{C}\right)+\frac{3}{4}\ddot{R}^2\left(1-\frac{\dot{R}}{3C}\right)=H\left(1+\frac{\dot{R}}{C}\right)+\frac{R\dot{H}}{C}\left(1-\frac{\dot{R}}{C}\right), \tag{3.1.1}$$

where

$$H=\frac{1}{\rho_\infty}\frac{n}{n-1}(p_\infty+B)\left[\left(\frac{p+B}{p_\infty+B}\right)^{\frac{n-1}{n}}-1\right], \tag{3.1.2}$$

with ρ_∞ the liquid density at infinity, C the speed of sound at the bubble surface, and n and B constants from the Tait equation of state.

The bubble, initially at equilibrium with an initial radius of 8.1 μm, was subject to an acoustic wave driven at a frequency of 21.4 kHz with pressure amplitude 132 kPa. The surrounding liquid is water, with density 1000 kgm^{-3}, viscosity $\mu = 1$ mPa·s, and surface tension coefficient $\sigma = 0.073$ N m^{-1}. The ambient pressure $p_\infty = 101$ kPa and the vapour pressure $p_v = 2980$ kPa. The experimental results are represented by the dots in figure 3.1, and the Gilmore model represented by the solid line. Using $N = 71$ segments to discretise the surface of the bubble, we receive the radius history in figure 3.2 generated by the VCBIM.

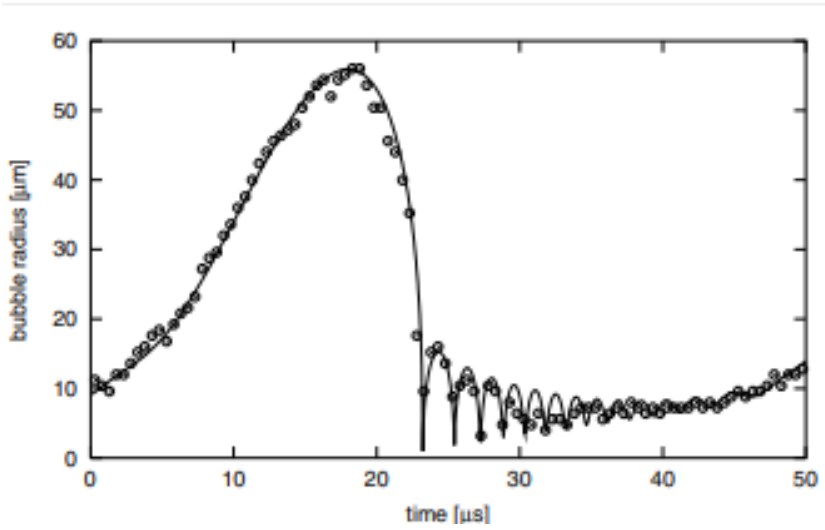

Figure 3.1: Experimental radius history of a bubble subject to a strong acoustic wave (dots), and the theoretical radius history using the spherical bubble Gilmore model (solid line). The bubble has initial radius 8.1 μm, and the acoustic wave has a frequency of 21.4 kHz with pressure amplitude 132 kPa. The surrounding liquid is water, with parameters $\rho = 1000$ kgm^{-3}, $\mu = 1$ mPa·s, $\sigma = 0.073$ N m^{-1}, $p_\infty = 101$ kPa and $p_v = 2980$ kPa.

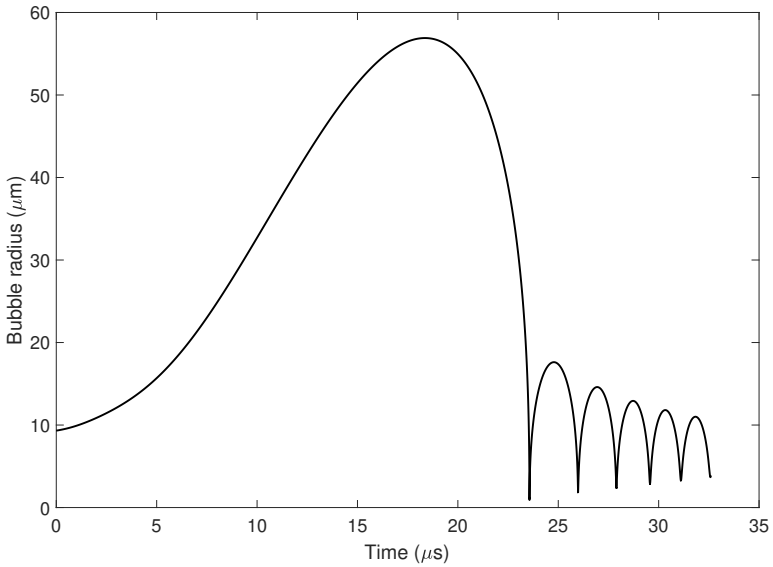

Figure 3.2: The radius history of a bubble subject to a strong acoustic wave, generated with the viscous, compressible boundary integral method. The parameters are the same as in figure 3.1.

3.1.1 Analysis of Results

In this case, the bubble experiences slow expansion, followed by a rapid collapse. There are then several after-bounces, that take place very rapidly. These occur so quickly that the camera used to generate the experimental results cannot distinguish the individual minima and maxima. We see very good agreement between the the results from figure 3.2 and 3.1. The maximum and minimum radius of each oscillation agrees well with the spherical bubble model, as well as the time at which they occur. After six oscillations, the model fails, as non-linear shape mode oscillation begins to form and the bubble collapses.

Now the modelling of non-spherical oscillations of bubbles subject to acoustic waves can be considered, given the demonstrated capability of the VCBIM to accurately predict spherical oscillations.

3.2 Bubble Subject to a Modulated Acoustic Wave

In the works of (Guédra et al. [2016]), a single air bubble was subject to a modulated acoustic wave with the aim of developing different shape modes. A shape mode is defined as a pattern of motion in which all points move sinusoidally with the same frequency and phase. The specific number of the shape mode is the number of half waves in the vibration. The frequencies at which the shape modes occur are the natural frequencies of the system.

In experimental works, evidence was found of non-linear shape mode coupling, as well as parametrically driven shape mode oscillations. Non-linear shape mode coupling occurs when other shape modes are trying to develop on the surface. They also found that at the driving frequency, shape mode three oscillation was driven mainly by the radial oscillation of the bubble. This is due to the fact that the driving frequency was close to that of the natural frequency for shape mode three. We have the natural frequency of shape mode n

given by (Lamb [1932])

$$\omega_n = \frac{1}{2\pi}\sqrt{(n-1)(n+1)(n+2)\frac{\sigma}{\rho R_0^3}}. \tag{3.2.1}$$

In the experiment, the bubble, initially at equilibrium, had initial radius $R_0 = 67\mu$m. The acoustic wave was driven at 33.2 kHz, with pressure amplitude 14 kPa, and modulated at a frequency of 100 Hz. The bubble is initiated in water, so the surface tension at the interface is $\sigma = 0.073$ N m^{-1}, and the density 1000 kg m^{-3}. This leads to the natural frequency of shape mode three $\omega_3 = 15.6$ kHz. Shape mode three oscillates at half the driving frequency, so we can see that the driving frequency of the experiment is very close to that expected to generate shape mode three.

As the acoustic wave is modulated, the pressure due to the acoustic wave is defined to be

$$p_{ac} = p_a \sin(2\pi f_m t)\sin(2\pi f t), \tag{3.2.2}$$

where $p_a = 14$ kPa is the pressure amplitude of the wave, $f_m = 100$ Hz is the modulation frequency, and $f = 33.2$ kHz is the driving frequency.

The weakly viscous, compressible model is applied to the experimental case. Of the undefined parameters, the ambient pressure is $p_\infty = 101.3$ kPa, the initial vapour pressure inside the bubble is $p_v = 2.98$ kPa, and the viscosity is $\mu = 1$ mPa·s. The surface of the bubble is discretised into 71 segments, so $N = 71$.

In figure 3.3, we can see a comparison between the radius history of the bubble in the experiment (above) and from the VCBIM (below). As the bubble is non-spherical, the equivalent radius is used, found from the volume of the bubble. The profile of the theoretical bubble shape is then superimposed as a red line over the images captured during the experiment in figures 3.4 to 3.9. This is done at a total of 18 points in time over the interval.

3.2.1 Comparison of Experimental and Theoretical Results

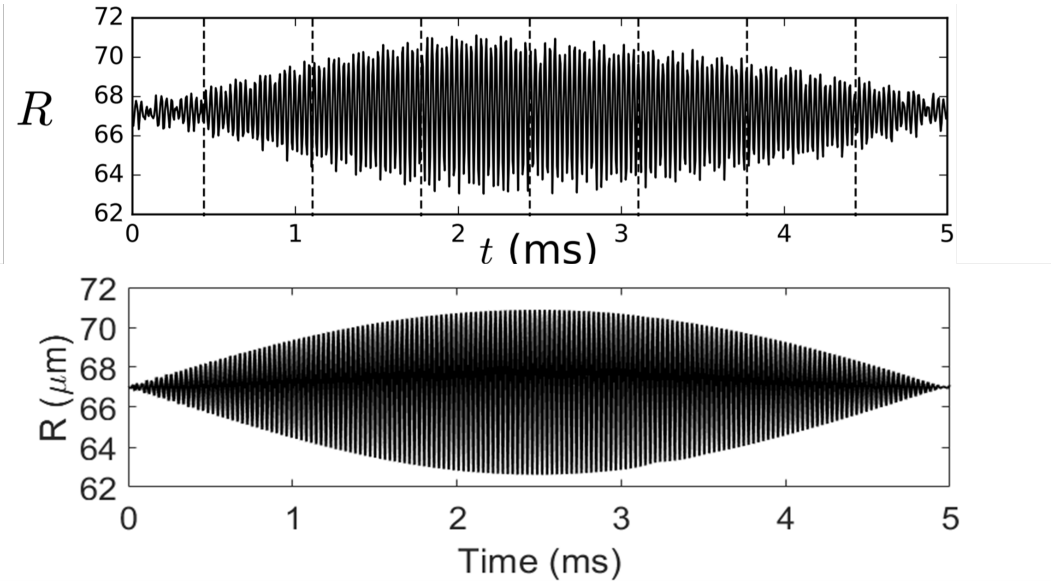

Figure 3.3: Comparison between the radius history of the bubble from experimental results (above) and theoretical results (below). The bubble has initial radius 67 μm, and the acoustic wave has a frequency of 33.2 kHz modulated at 100 Hz with pressure amplitude 14 kPa. The surrounding liquid is water, with parameters $\rho = 1000$ kg m^{-3}, $\mu = 1$ mPa·s, $\sigma = 0.073$ N m^{-1}, $p_\infty = 101$ kPa and $p_v = 2980$ kPa.

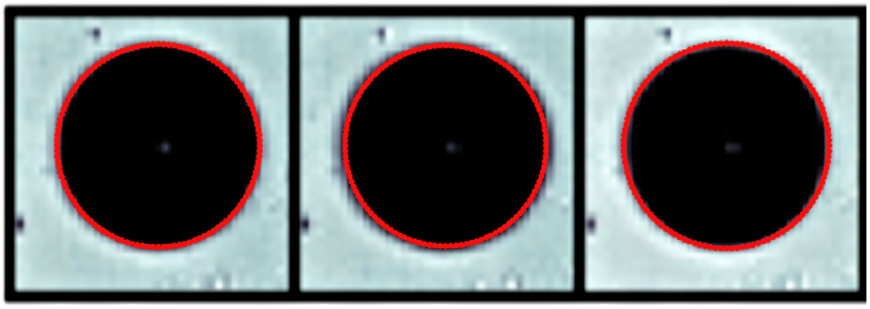

Figure 3.4: Comparison between the shape of the bubble from experimental results and from the numerical model (red outline). The images are pictured at $t = 0.0$ ms, 0.28 ms, 0.56 ms from left to right. The parameters are the same as in figure 3.3.

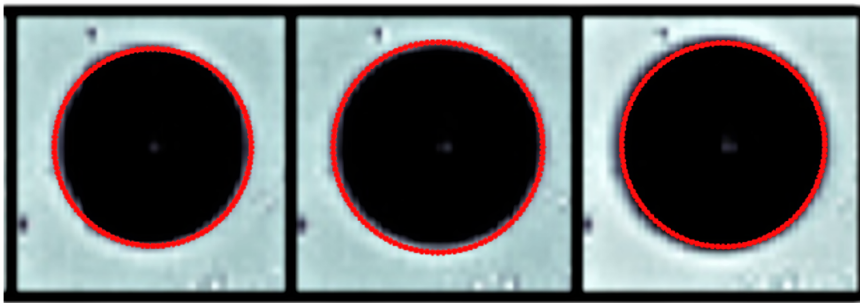

Figure 3.5: Comparison between the shape of the bubble from experimental results and from the numerical model (red outline). The images are pictured at $t = 0.83$ ms, 1.11 ms, 1.39 ms from left to right. The parameters are the same as in figure 3.3.

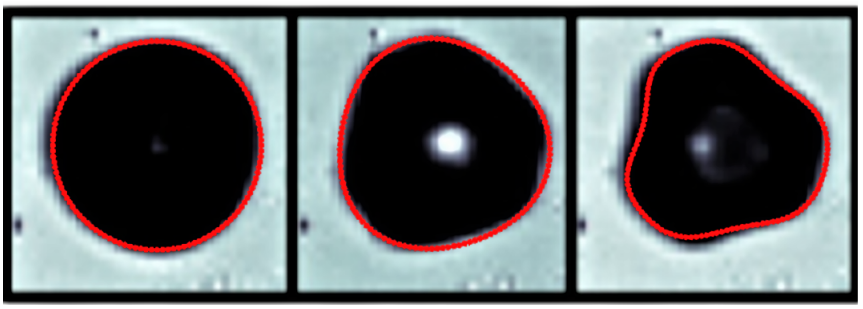

Figure 3.6: Comparison between the shape of the bubble from experimental results and from the numerical model (red outline). The images are pictured at $t = 1.67$ ms, 1.94 ms, 2.22 ms from left to right. The parameters are the same as in figure 3.3.

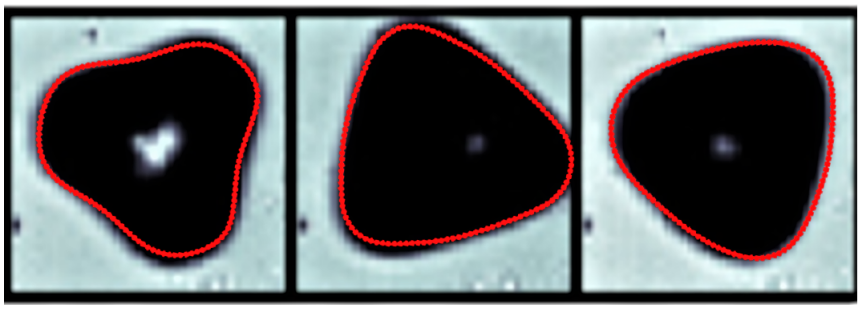

Figure 3.7: Comparison between the shape of the bubble from experimental results and from the numerical model (red outline). The images are pictured at $t = 2.5$ ms, 2.78 ms, 3.05 ms from left to right. The parameters are the same as in figure 3.3.

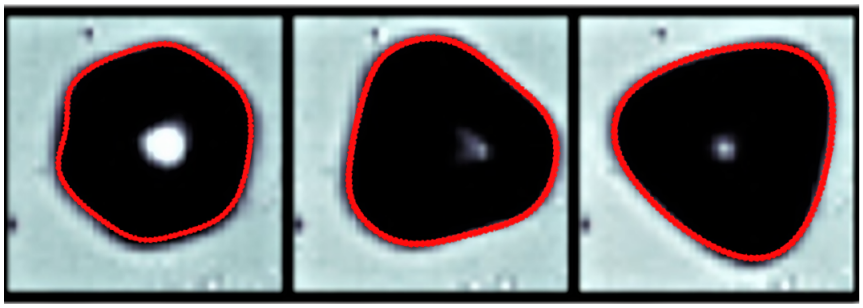

Figure 3.8: Comparison between the shape of the bubble from experimental results and from the numerical model (red outline). The images are pictured at $t = 3.33$ ms, 3.61 ms, 3.89 ms from left to right. The parameters are the same as in figure 3.3.

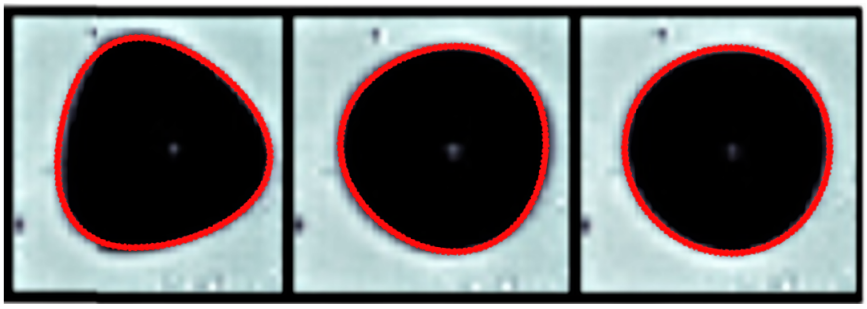

Figure 3.9: Comparison between the shape of the bubble from experimental results and from the numerical model (red outline). The images are pictured at $t = 4.17$ ms, 4.44 ms, 4.72 ms from left to right. The parameters are the same as in figure 3.3.

3.2.2 Analysis of Results

In this case, a bubble is subject to an acoustic wave travelling from left to right at a slight angle from horizontal. The bubble oscillates many times over the time period. As opposed to the previous case, the oscillation is very stable. This is due to the modulation of the acoustic wave. The stability allows for us to observe the bubble for a long period of time, and eventually find the development of shape mode three. In the experimental images, the camera captures the bubble from above. The image of the bubble is the black shape, and the theoretical results are represented by the red line on top of the image. The outline we see of the experimental bubble is the cross section through the centre, in the same plane as the axisymmetric bubble. The light that often appears at the centre of the

bubble is due to the back-lighting required to capture the images.

We see a good agreement between the radius history of the experimental results and the theoretical ones of the viscous, compressible bubble model. The total time period of oscillation agrees well, with the bubble radius returning to equilibrium after 5 ms. This makes physical sense given that the acoustic wave is modulated at a frequency of 100 Hz, and so would have a pressure amplitude of 0 Pa after 5 ms. The profile of the radius also agrees well over time, with the maximum and minimum radius of approximately 71 μm and 63 μm, respectively. The experimental results contain some error and do not have as uniform an appearence as the theoretical results. This could be for many reasons, including experimental error or external factors. Due to the very small length and time scales, μm and ms respectively, there is some error involved in the measurement of the bubble radius over time. Additionally, experimental error would be expected from equipment such as the transducer generating the acoustic wave. This error would result in a small change to the expected frequency and amplitude of the wave. Finally, the presence of impurities in the water can have the effect of altering the conditions at the surface of the bubble. An example would be the lowering of surface tension which would lead to a sloght change in the bubble radius. The order of magnitude of these errors is not stated in Guédra et al. [2016], however they would be expected to have a small influence on the results. The overall shape of the oscillation history agrees very well, however.

The predicted shape of the bubble from the model agrees very well with the experimental results. We initially see small oscillations about the equilibrium radius in figures 3.4 and 3.5. The amplitude of oscillation grows in magnitude, until shape mode three oscillations become apparent in figure 3.6. These are expected given the frequency of the acoustic wave is close to the natural frequency of shape mode three oscillation. The onset of shape mode three is slightly delayed in the theoretical model. In figure 3.6, the central image predicting the first onset of shape mode three happens 0.1 ms after the ex-

perimental image was captured, with the 0.1 ms delay continuing through the rest of the images. This is a small deviation, that does not have a significant impact on the results. It could be due to many factors, since experiments are difficult to control. A slight error in the measurement of the initial radius, or a slightly larger pressure amplitude of the acoustic wave could be potential causes of this time delay. The bubble then continues to oscillate with shape mode three in figures 3.7 and 3.8 with very good agreement with the experimental shapes. The bubble returns to spherical oscillation in figure 3.9.

3.3 Viscous and compressible effects

Next, the VCBIM is compared with other numerical results[1]. Shaw [2017] used an asymptotic model to study the shape mode oscillation of parametrically forced bubbles including viscous and compressible effects. Many cycles of oscillation were considered, showing the importance of the inclusion of viscous and compressible effects. The case chosen for comparison considers a microbubble with an equilibrium radius of 144 μm subject to an acoustic wave with a pressure amplitude of 13 kPa and a frequency of 10 kHz. The remaining parameters are $\kappa = 1.4$, $\sigma = 0.073$ N m^{-1}, $p_\infty = 100$ kPa, $p_v = 3$ kPa, $\mu = 1$ mPa·s and $\rho_L = 1000$ kg m^{-3}.

As is seen in figure 3.10, the VCBIM obtains excellent agreement with the results of the asymptotic model. The shape mode three oscillation is accurately predicted at each time, despite the numerous cycles of oscillation leading up to this time. This demonstrates the ability of the VCBIM to model a case with important viscous and compressible effects.

Additionally, Tsiglifis and Pelekasis [2005] examined the weakly viscous oscillation of elongated bubbles using a hybrid boundary-finite element method. They revealed that small initial elongations would return to a spherical shape for any Ohnesorge number,

[1]This section consists of my contribution to Wang et al. [2022].

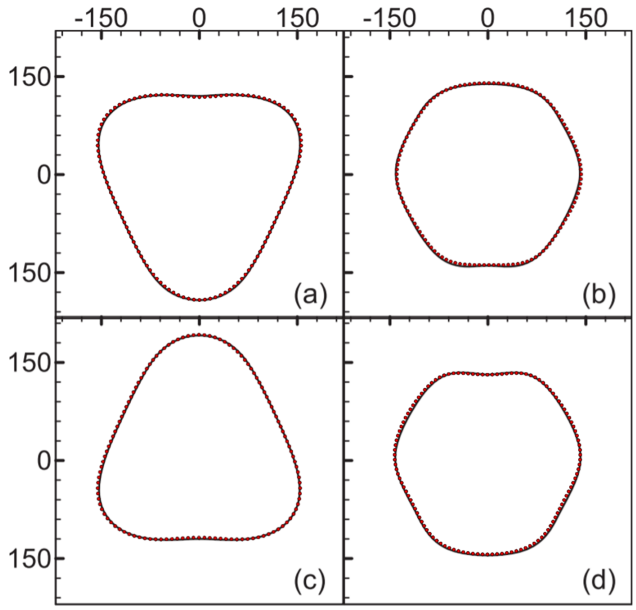

Figure 3.10: Comparison of the results obtained from the VCBIM (red dotted line) with those of Shaw [2017] where a bubble with equilibrium radius 144 μm is subject to an acoustic wave with a pressure amplitude of 13 kPa and a frequency of 10 kHz. The selected times are at (a) t = 10.07 ms; (b) t = 10.11 ms; (c) t = 10.17 ms; and (d) t = 10.22 ms. The other parameters are $\kappa = 1.4$, $\sigma = 0.073$ N m^{-1}, $p_\infty = 100$ kPa, $p_v = 3$ kPa, $\mu = 1$ mPa·s, and $\rho_L = 1000$ kg m^{-3}.

$Oh = \mu/(\rho R\sigma)^{1/2}$, whilst for larger elongations there is a threshold value of Oh^{-1} above which the bubble breaks up. The case chosen for comparison considers a microbubble with an equilibrium radius of 5.8 μm and an initial elongation parameter of S = 0.6. The inverse Ohnesorge number is given by $Oh^{-1} = 1000$, with the rest of the parameters as in figure 3.10. Figure 3.11 shows the comparison between the results of this case with those of the VCBIM during jet formation. Very good agreement is achieved between the bubble shapes, with good agreement between the jet profiles. The importance of viscous effects is demonstrated in figure 3.12, where the bubble shapes of the viscous and inviscid models are compared during bubble collapse. The inviscid model leads to an inaccurate bubble shape, in particular the profile of the jet. Including viscous effects leads to the formation of a wider jet, at both the opening of the jet and the tip. This is as expected when considering viscous effects and agrees with the results of (Tsiglifis and Pelekasis

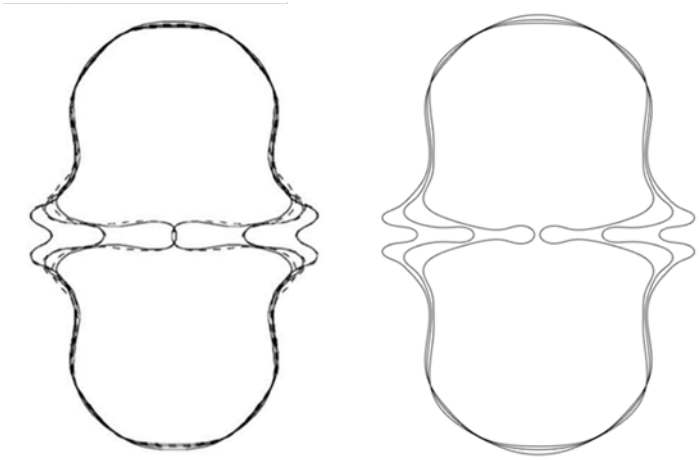

Figure 3.11: Comparison of the results of Tsiglifis and Pelekasis (2005) (left) with those of the VCBIM (right) where a bubble with equilibrium radius 5.8 μm is perturbed by an initial elongation parameter of S = 0.6. The inverse Ohnesorge number is given by Oh^{-1} = 1000, with the rest of the parameters as in figure 3.10. The selected times are at t = 1.3215, t = 1.3312 and t = 1.3453.

[2005]).

In order to judge the importance of the inclusion of viscous and compressible effects, four variations of one case are considered. These variations are including both viscous and compressible effects, only viscous effects, only compressible effects, and neither viscous nor compressible effects. The case considered is for a bubble of equilibrium radius 36 μm in water is subject to an acoustic wave with frequency 130 kHz and amplitude 120 kPa. The other parameters are $\kappa = 1.4$, $\sigma = 0.073$ N m^{-1}, $p_\infty = 100$ kPa, $p_v = 3$ kPa, $\mu = 1$ mPa $\cdot$ s and $\rho = 1000$ g m^{-3}. The ninth minimum of oscillation is examined. The inclusion of compressible effects is important to accurately model the profile of jets that may form during bubble oscillation. As is seen in figure 3.13, the inclusion of compressible effects leads to the formation of a smaller jet. This is due to the energy loss at minimum volume associated with compressible effects. Additionally, the minimum

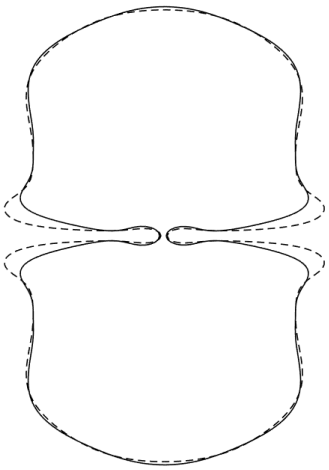

Figure 3.12: Comparison between the VCBIM (solid line) and CBIM (dotted line) during bubble collapse. The parameters are the same as in figure 3.11, except Oh^{-1} is infinite in the CBIM.

volume of the incompressible model is 0.6% smaller than that of the compressible model. Thus, when modelling multiple cycles of oscillation involving the formation of liquid jets, it is important to include compressible effects to improve the accuracy of the following cycles of oscillation.

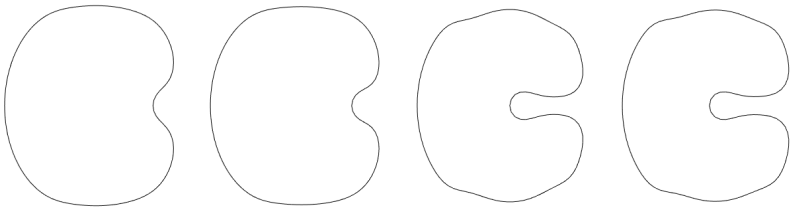

Figure 3.13: Comparison of bubble shapes at ninth minimum expansion for the case described in figure 7. From left to right, the case includes both viscous and compressible effects, only viscous effects, only compressible effects, and neither viscous nor compressible effects.

Viscous effects prove to be very important to produce accurate bubble shapes and jet

profiles. In figure 3.13, it is seen that the inviscid cases have a significantly different profile than those including viscous effects. A significantly larger jet is formed in the inviscid cases, as well as a more irregular shape. This is due to the lack of viscous dissipation that would otherwise lead to a more regular shape as seen in the viscous cases. Despite the relatively low viscosity of the surrounding fluid, the effect of viscosity compounds over numerous cycles leading to significant differences by the ninth minimum. Hence, the inclusion of viscous effects is crucial to accurately model multiple cycles of oscillation.

Chapter 4

Shape mode oscillation of a bubble near a rigid boundary

Recent experiments (Vyas et al. [2020]) have revealed the interesting cleaning effects that take place due to the shape mode oscillation of bubbles over a rigid boundary. Whilst a microbubble was undertaking shape oscillation moving over a bacterial biofilm, it removed the contaminants from the boundary and created a clean path through the biofilm. This demonstrated much higher cleaning efficiency than that associated with the volume oscillation of cavitation bubbles, however the mechanism is unknown. In this chapter, we study this phenomenon using the boundary integral method, with the viscous effects modelled using the viscous potential flow theory and the compressible effects using the weakly compressible theory. The viscous stress at the rigid boundary is approximated using boundary layer theory. We observed that the natural frequencies of shape mode oscillation decrease significantly due to the presence of the boundary. The shear stress at the boundary due to the shape oscillation of a nearby bubble is at least twenty times higher than that due to volume oscillation with the same energy, and is significant only within the area directly beneath the bubble. This is explained by the notably faster decay for higher shape modes of the kinetic energy in the fluid as the distance to the

centre of the bubble r increases, with the induced velocity of mode k decaying at a rate of $\mathcal{O}(r^{-(k+2)})$ away from the bubble. These results achieve excellent agreement with the intriguing cleaning effects first observed in the experiment, and explain the mechanism behind this new highly efficient method of cleaning.

4.1 Mathematical Model

4.1.1 Modelling a bubble connected to a rigid boundary

When a part of a bubble surface is nearly in contact with the rigid boundary, it tends to remain being nearly in contact with the boundary (Wang et al. [2015]). This results in numerical instabilities in the simulations using the BIM. To avoid these numerical instabilities, we remove the thin layer of liquid between the bubble surface and the boundary, join the bubble surface with its image to the boundary and simulate "the combined bubble" (Ni et al. [2015]; Wang et al. [2015]). In the simulations performed in this paper, the join takes place when the minimum distance δ_{min} between bubble surface and the boundary is in the range of 0.01 to 0.04.

As the bubble surface is in contact with the rigid boundary, the contact angle of the liquid-gas interface with the rigid boundary depends on the properties of the liquid, gas and the hydrophilic property of the boundary and may change with the dynamics (Shikhmurzaev [2007]). For simplicity, we assume that the contact line between them is fixed. With the smoothed cubic spline used for the interpolation of the bubble surface (Wang et al. [2019]), the solid angle $c(\mathbf{r}, t)$ takes the value 2π at the bubble surface except for at the contact line. The solid angle at the point on the contact line is given by

$$c(\mathbf{r}, t) = \iint_{S_\varepsilon} \frac{\mathrm{d}S}{\varepsilon^2}, \tag{4.1.1}$$

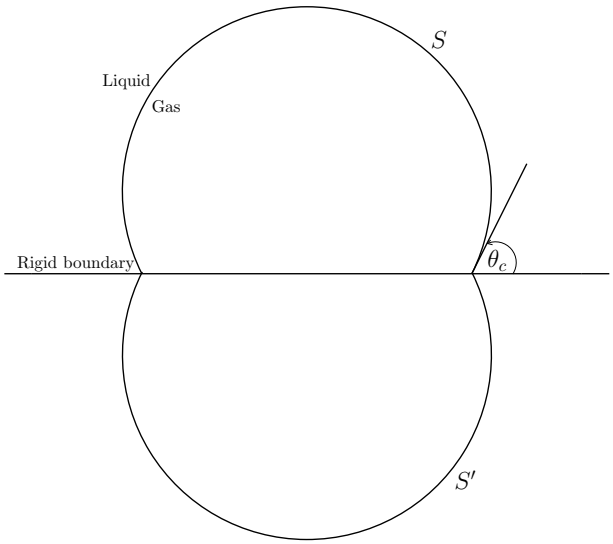

Figure 4.1: A schematic of a bubble with surface S connected to its image with surface S' on a rigid boundary. The contact angle between the bubble wall and the rigid boundary is θ_c.

where S_ε is the part of a spherical surface with radius ε centred at the contact point, cut by the tangent plane of the bubble surface and the tangent plane of the imaged bubble surface at the point of contact. Now,

$$c(\mathbf{r},t) = 2\int_0^{\pi} \mathrm{d}\theta \int_0^{\theta_c} \frac{\varepsilon^2 \sin\phi}{\varepsilon^2}\,\mathrm{d}\phi = 2\pi(1-\cos\theta_c), \tag{4.1.2}$$

where θ_c is the angle between the bubble surface and rigid wall at the contact line. This configuration is shown in figure 4.1.

4.1.2 Calculating shear stress at the rigid boundary

Nyborg [1958] obtained an approximate solution for the local viscous flow near a rigid boundary due to steady oscillating irrotational flow near a fluid-solid interface using boundary layer theory. The viscous shear stress at the rigid boundary is then approxi-

mated using boundary layer theory (Nyborg [1958]; Doinikov and Bouakaz [2010]) by

$$\tau_{zr_2} = \sqrt{\frac{\rho\mu}{\omega}} \left(u_{r2} \frac{\partial u_{r_2}}{\partial r_2} \right)_{z=0} = \sqrt{\frac{\rho\mu}{\omega}} \left(\frac{\partial \phi}{\partial r_2} \frac{\partial^2 \phi}{\partial r_2^2} \right)_{z=0}. \tag{4.1.3}$$

Here we assume that the z-axis is along the axis of symmetry and the origin is at the rigid boundary; r_2 is the r-coordinate in cylindrical coordinates.

To compare the shear stress for various modes of oscillation, we set the bubble system to have the same initial value of energy. The same potential energy of the system is achieved by setting the same initial radius and bubble gas pressure. We then need to set the same initial kinetic energy for the bubble system.

The kinetic energy of a bubble in a potential flow reads (Wang [2016]):

$$E_k(t) = \frac{\rho}{2} \oint_S \phi \phi_n \, dS. \tag{4.1.4}$$

Initially the bubble is spherical, meaning

$$E_k(0) = -\frac{\rho}{2} \oint_S \phi \phi_r \, dS. \tag{4.1.5}$$

Assuming the bubble is initially oscillating in shape mode k with amplitude a_k, the initial potential and its derivative with respect to r are given as

$$\phi_k(r,0) = \frac{a_k}{r^{k+1}} P_k(\cos\theta), \quad \frac{\partial \phi_k(r,0)}{\partial r} = -(k+1)\frac{a_k}{r^{k+2}} P_k(\cos\theta). \tag{4.1.6}$$

Substituting equation 4.1.6 into 4.1.5 yields

$$E_k(0) = \frac{\rho}{2}(k+1)\frac{a_k^2}{R_0^{2k+1}} \int_0^{2\pi} P_k^2(\cos\theta) \, \mathrm{d}\theta \int_0^{\pi} \sin\phi \, \mathrm{d}\phi = (k+1)\rho \frac{a_k^2}{R_0^{2k+1}} \int_0^{2\pi} P_k^2(\cos\theta) \mathrm{d}\theta, \tag{4.1.7}$$

where P_n is the Legendre polynomial of order n and R_0 is the initial radius of the bubble. In eqs. (4.1.5-4.1.7), (r, ϕ, θ) are the spherical coordinates with the origin at the bubble centre. With suitable choice of the amplitude a_k, the initial kinetic energy of the bubble system can be set at the same value for different modes k. The shape modes $k = 0, 1$ are for the spherical oscillation, translation of a bubble, and $k \geq 2$ is for non-spherical oscillation.

4.2 Numerical results and discussion

4.2.1 Validation of BIM model

The ability of the present BIM model to accurately model nonlinear oscillations is demonstrated in figure 4.2 in a comparison with the analytic results of (Tsamopoulos and Brown [1983]). A bubble, initially at equilibrium, with a radius of 0.06 cm is surrounded by an infinite fluid, in this case taken to be water. The density of the surrounding fluid is $\rho =$ 998 kg m^{-3}, the viscosity is $\mu = 10^{-3}$ Pa·s, the surface tension coefficient is $\sigma = 0.073$ N m^{-1}, and the polytropic constant is taken to be $\lambda = 1.4$. The ambient pressure is taken as $p_\infty = 101300$ Pa, and the vapour pressure inside the bubble is $p_v = 2980$ Pa. Here, the natural frequency of mode two oscillation is plotted against an increasing amplitude of oscillation measured by the axis ratio at maximum prolate shape (L/W). As the ratio increases, i.e. the size of the initial disturbance at the surface of the bubble increases, the natural frequency of oscillation decreases at a nonlinear rate. The numerical results of the BIM agree very well up to an axis ratio of $L/W = 1.5$, before starting to diverge from the analytical results. This can be explained by the limitations of the asymptotic model, which is only accurate up to a certain order.

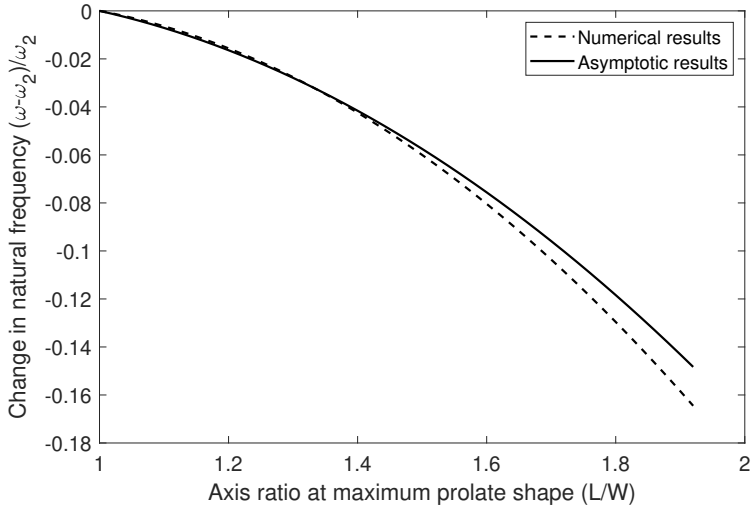

Figure 4.2: Comparison between change in $n = 2$ oscillation frequency with increasing amplitude of oscillation for the numerical results of the BIM (dashed line), and the analytical results of Tsamopoulos and Brown [1983] (solid line). A bubble with initial equilibrium radius $R_0 = 0.06$ cm is surrounded by an infinite field of water, with parameters $\gamma = 1.4$, $\sigma = 0.073$ N m^{-1}, $\rho = 998$ g m^{-3}, $\mu = 10^{-3}$ Pa·s, $p_\infty = 101300$ Pa and $p_v = 2980$ Pa.

The ability of the BIM model to numerically calculate the natural frequency of small order shape mode oscillations of a bubble is demonstrated in table 4.1. The initial bubble has a radius of 25 μm, with the remaining parameters the same as in figure 4.2. A small perturbation to the initial potential at the surface of the bubble is used to stimulate oscillation. This is of the form $\phi_0 = \varepsilon P_l(\cos\theta)$, where $\varepsilon \ll 1$, l is the shape mode number, P_l the Legendre polynomial of order l, and θ the angle between the position on the bubble surface and the x-axis. This initial potential is small and allows for an accurate comparison with the analytical results. As can be seen from table 4.1, the error in the calculation of the natural frequency of shape mode oscillation is very low. This demonstrates the ability of the present model to accurately predict the natural frequency of the shape mode oscillation of a bubble.

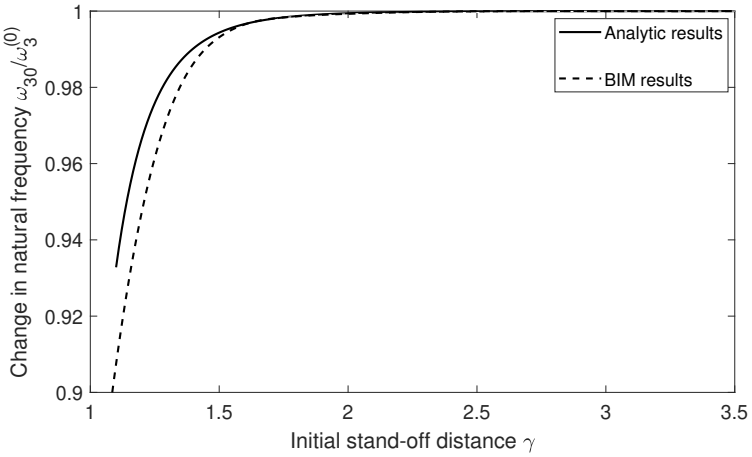

Figure 4.3: The natural frequency of shape mode three oscillation of a bubble, with initial radius $R_0 = 0.001$ m in water, calculated at multiple stand-off distances γ. The analytical results of Maksimov [2020] are compared with the present BIM model. The remaining parameters are as in figure 4.2.

Mode number	Analytical natural frequency (Hz)	Numerical natural frequency (Hz)	Error
0	132395	132369	0.02%
2	37684.4	37710.6	0.07%
3	68802.1	68843.0	0.06%
4	103203	103329	0.10%

Table 4.1: Comparison between analytical natural frequency, numerically calculated natural frequency and the associated error for four shape modes of oscillation. The initial radius is 25 μm and the remaining parameters are as in figure 4.2.

Now, the calculation of natural frequency near to a rigid boundary is compared with the analytic results of Maksimov [2020]. For these analytical results, the natural frequency of shape mode three oscillation of a bubble with initial radius $R_0 = 0.001$ m in water is derived depending on the initial dimensionless stand-off distance to the wall $\gamma = h/R_0$. The effects of surface tension, viscosity, and compressibility are ignored. As axisymmetric shape oscillations are considered, the angular momentum $m = 0$.

As can be seen in figure 4.3, excellent agreement is achieved between the results of the present BIM and the analytical results as $\gamma \geq 1.5$. As $\gamma \leq 1.5$, the wall effects

are significant and are under-predicted by the analytical results. This demonstrates the capability of the BIM to accurately predict the natural frequency of a bubble in the presence of a rigid boundary. Now, these results can be extended to a viscous, compressible fluid, as well as extending the values of the initial stand-off distance that are to be considered.

4.2.2 Natural frequency of shape mode oscillations for varying stand-off distances

The effects of an increasing stand-off distance on the natural frequency of different shape mode oscillations are detailed in figures 4.4a-4.4d. The non-dimensional stand-off distance between the rigid boundary and the centre of the bubble, $\gamma = h/R_0$, is measured against the change in natural frequency of shape mode n, $(\omega - \omega_n)/\omega_n$. Here, ω_n represents the natural frequency of mode n in an infinite fluid. Modes zero through four are included, with the exception of mode one. This is because mode one, which represents translation, is not appropriate to compare with the other modes in this study, especially when considering the bubble fixed to the wall. Each case will be using the parameters previously defined in table 4.1.

Figure 4.4a shows the change in natural frequency of shape mode zero, representing volumetric oscillation, for different stand-off distances. As the initial distance between the bubble and the wall decreases, the natural frequency decreases. This is the effect of the flow between the bubble and the wall being inhibited by the wall, which has a greater impact the closer the bubble is to the wall. As the stand-off distance becomes large, the natural frequency tends to the natural frequency of a bubble in an infinite fluid. When the non-dimensional stand-off distance $\gamma = 50$, the natural frequency of shape mode zero oscillation is within one percent of that in an infinite fluid.

As the stand-off distance increases above $\gamma = 10$, the change in natural frequency

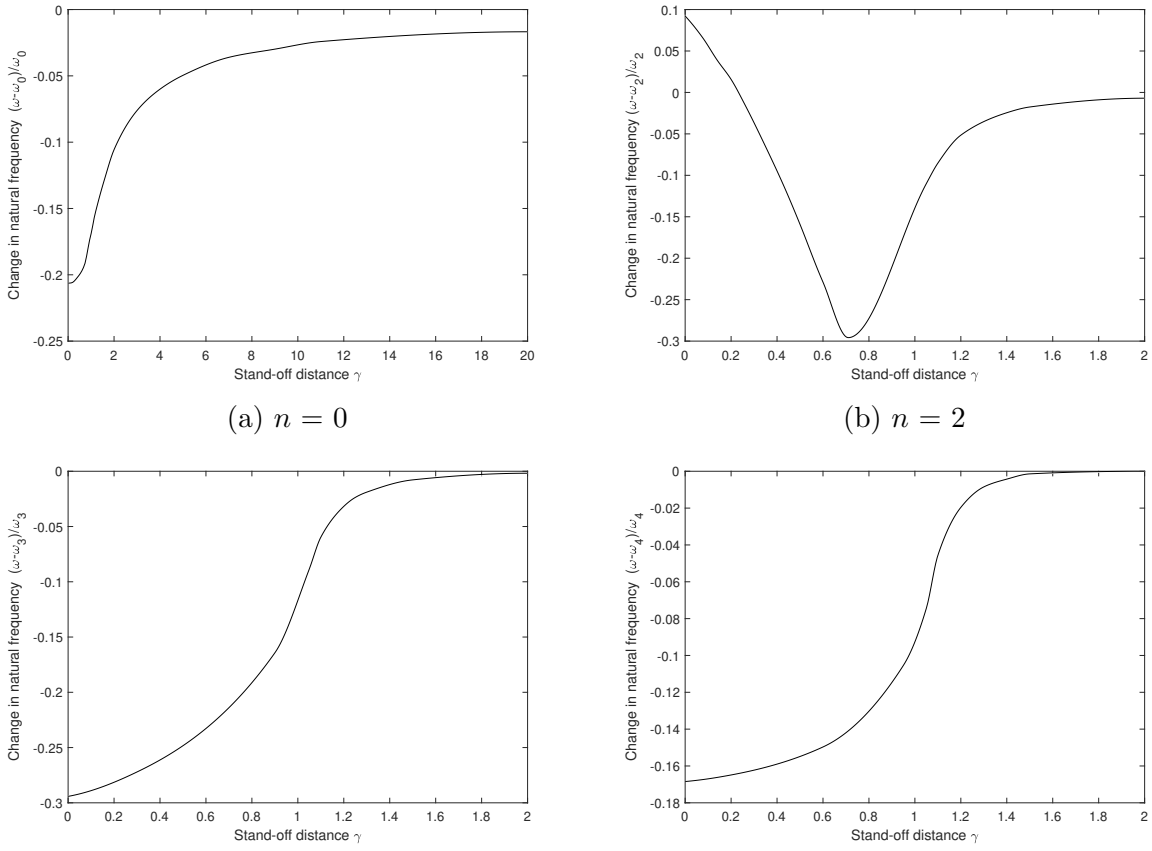

(a) $n = 0$ (b) $n = 2$

(c) $n = 3$ (d) $n = 4$

Figure 4.4: The change in shape mode n natural frequency with increasing stand-off distance for four different modes of oscillation. The bubble has initial radius $R_0 = 25$ μm, initial potential $\phi_0 = \varepsilon P_n(\cos\theta)$ where $\varepsilon \ll 1$, θ is the angle between the position on the bubble surface and the x-axis, and $P_n(\cos\theta)$ is the Legendre polynomial of order n. The remaining parameters are the same as in figure 4.2.

begins to increase at a linear rate. Below this point, the natural frequency changes at a non-linear rate. It is below $\gamma = 5$ that the natural frequency begins to rapidly decrease, signifying the growing impact of the wall as the distance between the bubble and wall decreases. When the bubble is fixed to the wall for $\gamma \leq 1$, the natural frequency continues to decrease at the same rate before tailing off around $\gamma = 0.5$. At $\gamma = 0$, the effect of the wall is at a maximum and so the natural frequency is at its minimum. This corresponds to a 21 percent decrease in natural frequency compared to a bubble in an infinite fluid.

Figure 4.4b shows the change in natural frequency of shape mode two oscillation for different stand-off distances. For stand-off distances greater than $\gamma = 1.75$, the natural frequency of mode two oscillation is within one percent of an equivalent bubble in an infinite fluid. The change in frequency slowly increases and tends towards zero as the stand-off distance increases beyond $\gamma = 1.75$. The wall has a significantly smaller effect on the oscillation frequency of shape mode two, when compared to mode zero oscillation, for $\gamma \geq 1$.

When the stand-off distance decreases below $\gamma = 0.7$, the change in natural frequency begins to increase. It continues to steadily increase until it reaches a maximum at $\gamma = 0$ of a 9 percent increase compared to a bubble in an infinite fluid. This can be explained by the effect of the fixed contact line on the shape mode two oscillation. When $\gamma = 0$, the bubble is a hemisphere resting on the wall. In this case, the fixed contact line is located at an antinode of oscillation for shape mode two. Enforcing the fixed contact line is analogous to imposing fixed boundary conditions to a freely oscillating system. This in turn leads to an increased natural frequency due to a reduced amplitude of oscillation.

Figures 4.4c and 4.4d show the change in natural frequency of shape modes three and four oscillation for different stand-off distances respectively. Both figures show similar behaviour, with the change in natural frequency approaching that of a bubble in an infinite fluid as γ increases. The natural frequency of shape mode oscillation is within one percent of an equivalent bubble in an infinite fluid when the stand-off distance is greater than $\gamma = 1.44$ for mode three, and $\gamma = 1.28$ for mode four.

In both cases, as the stand-off distance increases, the change in natural frequency increases. The change in natural frequency of shape mode three increases at a much greater rate than shape mode four, when the stand-off distance is between $\gamma = 0$ and $\gamma = 0.8$. For both figures, the decrease in natural frequency is at its maximum when $\gamma = 0$. Shape mode three oscillation sees a 29 percent decrease, and shape mode four oscillation

sees a 17 percent decrease at this point.

Comparing the different modes, we can make a number of observations. Firstly, for stand-off distances greater than approximately $\gamma = 1.2$, we note that as the mode number increases, the effect of the wall on the natural frequency decreases. This can be seen by comparing the exact stand-off distance at which the natural frequency of the mode is within one percent of a bubble in an infinite fluid. For mode zero this value is $\gamma = 50$, for mode two $\gamma = 1.75$, mode three $\gamma = 1.44$, and mode four $\gamma = 1.28$.

As the mode number increases, there is a decrease in natural frequency at $\gamma = 0$ when considering the even and odd modes separately. This implies that there are two separate behaviours for the even and odd modes. This trend can be seen in figure 4.5 in which the change in natural frequency is plotted against the increasing shape mode number. We see that the odd modes are more affected by the presence of the wall, as there is a larger decrease in natural frequency for odd modes compared to their even counterparts.

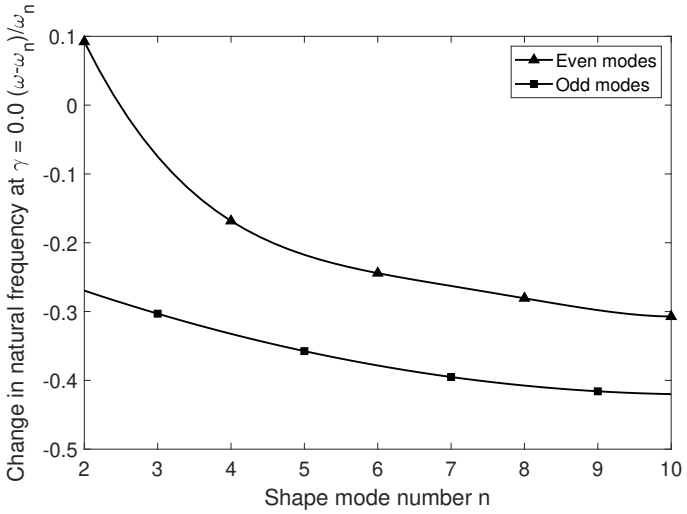

Figure 4.5: The change in natural frequency at a stand-off distance $\gamma = 0$ for increasing mode number. The even and odd modes are separated due to their different behaviours. The parameters are the same as in figure 4.4.

4.2.3 Shear stress generated on a rigid boundary

Here, we consider a bubble initially at equilibrium with radius $R_0 = 25$ μm, at a nondimensional stand-off distance from a rigid boundary of $\gamma = 1.3$ and $\gamma = 5.0$. The remaining parameters are the same as defined in table 4.1. The stand-off distance $\gamma = 1.3$ represents the behaviour of the bubble when it exists close to the wall, and the stand-off distance $\gamma = 5.0$ represents the behaviour of the bubble far away from the wall.

For both cases, the initial potential prescribed to the surface of the bubble is chosen to be $\phi_0 = \phi_a P_n(\cos\theta)$, where ϕ_a is the dimensionless amplitude of the potential distribution. To satisfy the constraint requiring the same initial kinetic energy for each modes, the size of the potential amplitude when $\gamma = 1.3$ is $\phi_a = 0.00692$, 0.00780, 0.00785, and 0.00787 for modes zero, two, three, and four respectively. When $\gamma = 5.0$, the potential amplitude is $\phi_a = 0.00775$, 0.00954, 0.00978, and 0.00991 for modes zero, two, three, and four respectively.

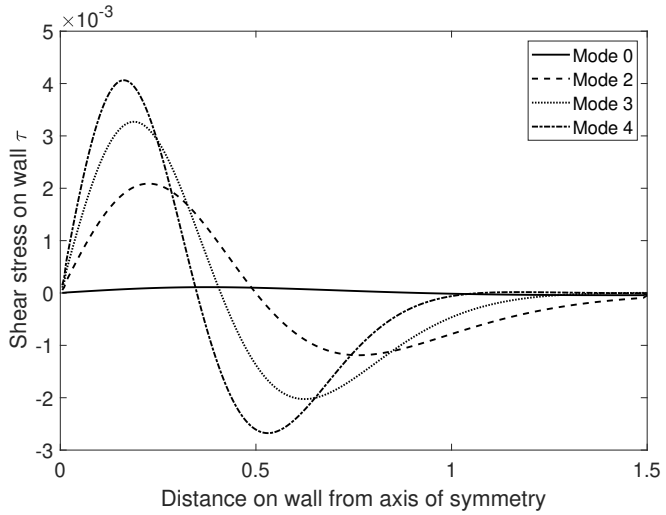

Figure 4.6: Comparison between the dimensionless shear stress generated on a rigid boundary by a bubble in shape mode zero, two, three and four oscillation at a stand-off distance $\gamma = 1.3$. The bubble has initial radius $R_0 = 25$ μm and dimensionless initial potential $\phi_0 = \phi_a P_n(\cos\theta)$, with $\phi_a = 0.00692$, 0.00780, 0.00785 and 0.00787 for modes zero, two, three and four respectively. The remaining parameters are as in figure 4.2.

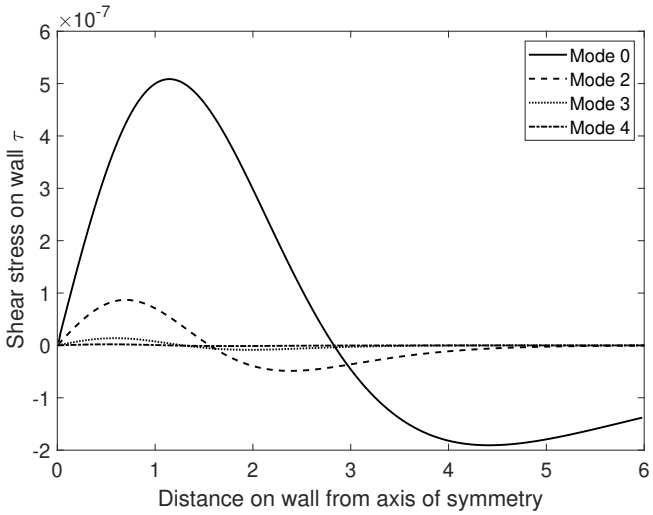

Figure 4.7: Comparison between the dimensionless shear stress generated on a rigid boundary by a bubble in shape mode zero, two, three and four oscillation at a stand-off distance $\gamma = 5.0$. The bubble has initial radius $R_0 = 25$ μm and dimensionless initial potential $\phi_0 = \phi_a P_n(\cos\theta)$, with $\phi_a = 0.00775$, 0.00954, 0.00978 and 0.00991 for modes zero, two, three and four respectively. The remaining parameters are as in figure 4.2.

Figures 4.6 and 4.7 display the shear stress on a rigid boundary generated by different shape modes when the bubble is close to and far away from the boundary respectively. The shear stress distribution is chosen at the time that the maximum shear stress occurs. Observing figure 4.6, it is clear that as the shape mode increases, so too does the maximum shear stress on the wall. Not only this, but the position of the maximum point moves closer to the axis of symmetry as the mode number increases. This could be explained by the fact that the width of the protrusion closest to the boundary decreases with increasing shape mode. For example, mode three is characterised by three protrusions of equal width, whilst mode four is characterised by four protrusions of equal width. The mode four protrusions have smaller width than those of mode three when both are compared on a bubble of the same size.

The maximum shear stress increasing with mode number may be explained by the speed of the protrusion closest to the wall. As the mode number increases, the frequency of shape mode oscillation increases, as does the speed of shape mode oscillation. The max-

imum occurs during the first oscillation, in which the protrusion closest to the boundary moves towards the boundary. As this protrusion dictates the behaviour of the shear stress, it follows that higher modes are associated with greater shear stress on the boundary due to the higher speeds. This is the case when the bubble is close to the wall where surface oscillations dominate the behaviour of the shear stress.

It can also be seen that as the mode number increases, the smaller the area the majority of the shear stress acts upon. For example, mode four oscillation exhibits the largest shear stress close to the axis of symmetry, however when the distance from the axis exceeds 0.6, the other modes begin to have greater values. On the other hand, despite mode zero oscillation having the smallest values of shear stress near to the axis of symmetry, when the distance exceeds approximately 1.8, mode zero has the greatest effect on the wall. In this region beyond a distance of 1.8, the behaviour is essentially reversed, and the values of shear stress decrease with increasing mode number.

For a bubble close to a boundary, higher shape modes of oscillation lead to a concentration of shear stress towards the axis of symmetry. This leads to significant increases in the maximum shear stress on the wall; shape mode four has a maximum shear stress approximately 20 times larger than that of mode zero. For higher modes, the majority of the shear stress occurs in the area directly beneath the bubble. Beyond a distance of approximately 1.5 from the axis of symmetry, the effect of the shear stress is essentially negligible when compared to that in the inner region. This could greatly benefit applications such as targeted ultrasonic cleaning.

Observing figure 4.7, it is clear that the maximum value of shear stress decreases with an increasing mode number. As with a bubble initiated close to a boundary, the position of the maximum value approaches the axis of symmetry when the mode number increases. Now, however, it is volumetric oscillation that drives the behaviour of the shear stress rather than surface oscillations.

As the bubble is further away from the boundary, it is no longer just the protrusion closest to the boundary that has the most significant impact. As the mode number increases, the amplitude of volumetric oscillation decreases. This explains why the maximum shear stress decreases as the mode number increases, given that volumetric oscillation is the driving force behind the generation of shear stress when the bubble is far away from the wall. Now, in contrast to the case with a bubble close to a wall, mode zero is by far the most effective shape mode to generate shear stress.

This implies that an approach with with two frequencies would be advisable to target both behaviours. This will ensure a more uniform cleaning and is in line with the approach used in industry.

4.2.4 Bubble shapes

A cycle of shape mode four oscillation near to a rigid boundary is shown in figure 4.8. To best display the characteristics of shape mode oscillation near to a rigid boundary, the initial stand-off distance is taken to be $\gamma = 1.15$ with a dimensionless initial potential amplitude of $\phi_a = 0.03$.

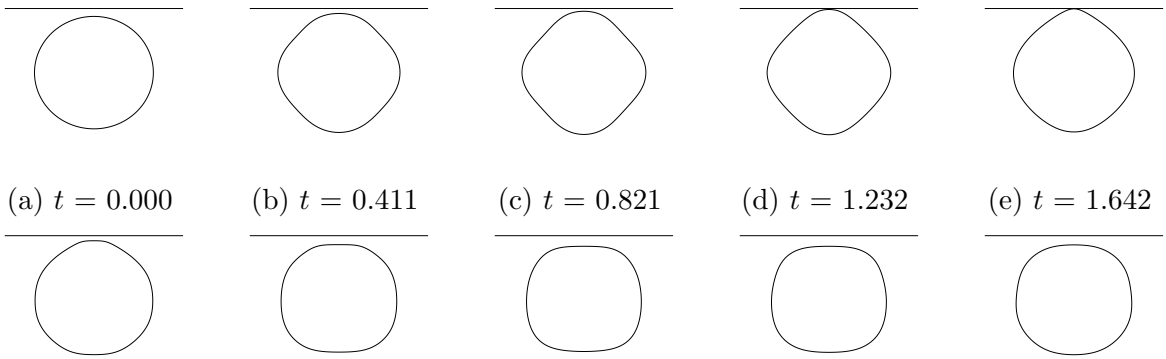

(a) $t = 0.000$ (b) $t = 0.411$ (c) $t = 0.821$ (d) $t = 1.232$ (e) $t = 1.642$

(f) $t = 2.053$ (g) $t = 2.464$ (h) $t = 2.874$ (i) $t = 3.285$ (j) $t = 3.696$

Figure 4.8: Bubble shapes for a cycle of mode four oscillation of a bubble with initial radius 25 μm in water located at a stand-off distance of $\gamma = 1.15$ from a rigid boundary. The initial potential is $\phi_0 = \phi_a P_4(\cos\theta)$ with dimensionless potential amplitude $\phi_a = 0.03$, with the remaining parameters as in figure 4.2.

The trends observed in figures 4.4 - 4.7 should have an effect on the shapes of the bubbles generated in these configurations. In order to observe these trends, we will consider three cases: a bubble initiated on a rigid boundary, close to a rigid boundary, and far away from a rigid boundary. To best contrast these behaviours, the three cases are taken to have stand-off distances of $\gamma = 0.0$, $\gamma = 1.3$, and $\gamma = \infty$ respectively. The specifications remain the same as in table 4.1, just with a larger initial potential amplitude. A larger potential amplitude is taken to better illustrate the changes to the bubble shapes.

The shapes of modes three and four will be compared, to demonstrate the difference between odd and even modes. To conserve energy between cases, the potential amplitude ϕ_a for mode three is taken to be $\phi_a = 0.0321$, 0.0255, and 0.0265 when $\gamma = \infty$, 1.3, and 0.0 respectively. For mode four, the potential amplitude is taken to be $\phi_a = 0.0326$, 0.0254, and 0.0251 when $\gamma = \infty$, 1.3, and 0.0 respectively. For each of these cases, we take the bubble shape at maximum expansion and compare at different stand-off distances. Additionally, we compare the differences between the bubble shapes for odd and even modes; here modes three and four. Figure 4.9 displays how the bubble shapes change with stand-off distance for modes three and four. Figure 4.10 compares how the bubble shapes change between modes for a bubble initiated on a wall and close to a wall.

Inspecting figure 4.9, we observe that mode three oscillation has a larger amplitude when the bubble is closer to the wall. This corresponds with the decreasing natural frequency as the bubble approaches the wall as in figure 4.4c. On the other hand, mode four displays very similar bubble shapes for both the close and far cases. As can be seen by comparing figures 4.4c and 4.4d, the natural frequency of mode four oscillation is less affected by the wall than mode three oscillation. Thus it follows that the wall should have less of an effect on the bubble shape. This trend is also reflected by the decreasing distance from the wall at which the natural frequency of increasingly higher shape modes of oscillation is within one percent of that of an equivalent bubble in an infinite fluid.

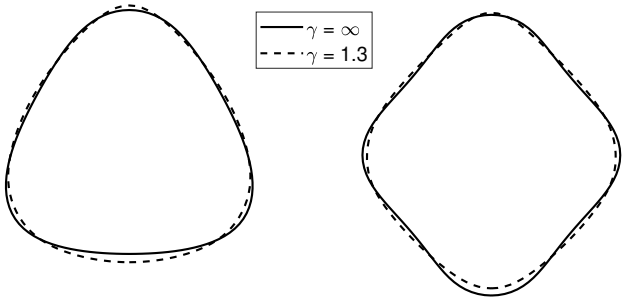

Figure 4.9: A comparison between the bubble shapes at maximum expansion for a bubble with initial radius $R_0 = 25$ μm close to a wall ($\gamma = 1.3$, dashed line), and far away from a wall ($\gamma = \infty$, solid line). Two cases are considered: mode three (left), and mode four (right). The dimensionless initial potential for mode three is $\phi_0 = \phi_a P_3(\cos\theta)$ with potential amplitude $\phi_a = 0.0321$ and 0.0255 for $\gamma = \infty$ and 1.3, respectively. For mode 4, $\phi_a = 0.0326$ and 0.0254 for $\gamma = \infty$ and 1.3, respectively. The remaining parameters are as in figure 4.2.

Thus we would expect that the bubble shape at a fixed stand-off distance should be less affected by the wall as the mode number increases.

Inspecting figure 4.10, we observe the differences between the shapes at maximum expansion of mode three and mode four oscillation at stand-off distances of $\gamma = 0.0$ and $\gamma = 1.3$. When the stand-off distance $\gamma = 0.0$, the bubble is initially a hemisphere connected to the rigid boundary. As can be seen, the fixed point connecting the bubble to the wall occurs at a node of mode four oscillation, inhibiting the ability of the bubble to reach maximum expansion. On the other hand, the fixed point does not occur at a node of mode three oscillation, leaving the bubble more free to expand. This property is the reason for the two separate behaviours of the oscillation frequency of odd and even modes, as the inhibited oscillation of even modes leads to a lower amplitude and hence higher frequency.

At a stand-off distance of $\gamma = 1.3$, the tip of the node closest to the rigid boundary is narrower than the equivalent case at $\gamma = \infty$. This corresponds with the narrower distribution of shear stress on the rigid boundary when the bubble is closer to the wall, as

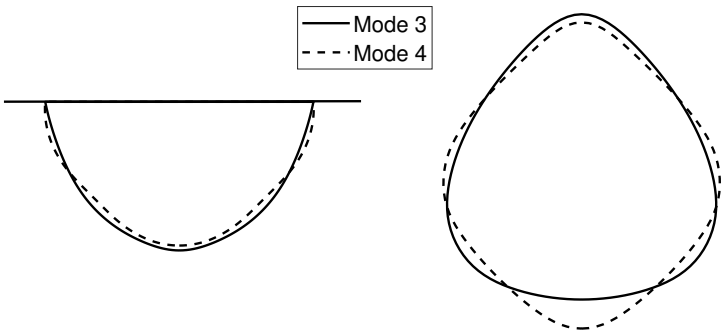

Figure 4.10: A comparison between the bubble shapes at maximum expansion for a bubble with initial radius $R_0 = 25$ μm of mode three (solid line) and mode four (dashed line) oscillation, considering a bubble initiated at a stand-off distance of $\gamma = 0.0$ (left) and $\gamma = 1.3$ (right). The initial potential for mode three is $\phi_0 = \phi_a P_3(\cos\theta)$ with dimensionless potential amplitude $\phi_a = 0.0255$ and 0.0265 for $\gamma = 1.3$ and 0.0, respectively. For mode 4, $\phi_a = 0.0254$ and 0.0251 for $\gamma = 1.3$ and 0.0, respectively. The remaining parameters are as in figure 4.2.

seen in figures 4.6 and 4.7. Additionally, the tip of the mode four node is narrower than that of the mode three node, corresponding with the findings of figure 4.6.

The shape mode three node closest to the wall has a larger amplitude than that of mode four. This is due to the higher frequency of mode four oscillation than mode three. The maximum shear stress generated on the wall, however, is larger for mode four than mode three. This indicates that the effect of the larger velocity associated with mode four oscillation makes up for the smaller amplitude of oscillation when compared with mode three. This explains the larger maximum shear stress generated on the wall by mode four oscillation than mode three, a trend which continues as the mode number increases.

4.2.5 Comparison with experimental observations

Having analysed the shear stress generated on a rigid boundary when the bubble is close and far away, we now consider the case of a bubble initiated on the wall. This is to

compare with the experimental results of (Vyas et al. [2020]), in which a bubble attached to a rigid boundary is shown only cleaning the area in the immediate vicinity of the bubble (supplementary video d).

To compare with this case, the contact angle between the bubble surface and the wall is chosen to be $\theta_c = \pi/4$, translating to an initial stand-off distance of approximately $\gamma = 0.707$. The remaining parameters are the same as in previous cases, with the exception of the potential amplitude selected to be $\phi_a = 0.00470, 0.00475, 0.00480$ in order to conserve energy between modes.

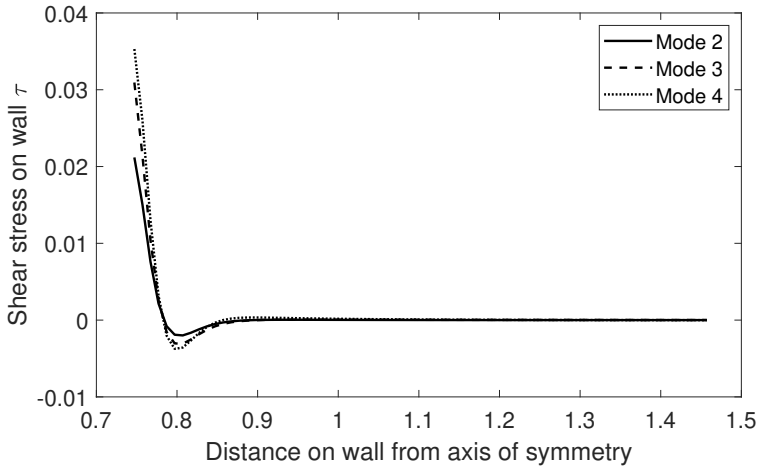

Figure 4.11: Shear stress generated on a rigid boundary by a bubble located at a stand-off distance of $\gamma = 0.70$. Shape modes two, three and four are compared. The remaining parameters are the same as in figure 4.4, with dimensionless potential amplitude $\phi_a = 0.00470, 0.00475, 0.00480$ for modes two, three and four, respectively.

As is seen in figure 4.11, shear stress is generated directly in the region near to the bubble surface. This agrees with experimental observations. Additionally, higher shape modes generate a larger maximum shear stress on the boundary. This suggests that higher shape modes should be targeted to maximise the removal of contaminants from a rigid boundary. The order of the maximum shear stress increases significantly as the stand-off distance decreases, so targeting higher shape modes located close to a rigid boundary should prove to be optimal for removal. The results from this thesis for the behaviour

of the natural frequency of shape mode oscillation at different stand-off distances can be used to more effectively target these higher shape modes near to a wall.

Chapter 5

Microbubble dynamics subject to a surfactant

In this chapter, a model for a bubble with a surfactant is derived using the Szyskowski equation for the updated surface tension, and the conservation of mass to update the concentration. Considering the applications towards ultrasonic cleaning, the modification of the behaviour of a bubble in shape oscillation is considered, as well as the formation of a liquid jet. It is found that the presence of a surfactant has a large impact on the amplitude and frequency of shape oscillation, and greatly increases the shear stress generated on a nearby rigid boundary. Jet formation is more likely, and the associated jet speed is increased.

5.1 Governing Equations

Given the presence of a non-ionic surfactant at a free surface, the surface tension is given by the widely used Frumkin equation of state (Frumkin [1925], Karakashev and Manev [2002], Taylor et al. [2003])

$$\sigma = \sigma_0 + \Gamma_\infty R_g T \log\left(\frac{\Gamma_\infty - \Gamma}{\Gamma_\infty}\right) + \beta\Gamma^2. \tag{5.1.1}$$

Here, σ_0 is the surface tension at the interface without the effect of a surfactant, Γ_∞ is the maximum packing concentration of the surfactant, R_g is the universal gas constant, T is the temperature, Γ is the concentration of the surfactant at the bubble surface, and β is a parameter of molecular interaction. In the special case of negligible molecular interaction ($\beta = 0$), the surface tension at the interface is described by the Szyskowski equation,

$$\sigma = \sigma_0 + \Gamma_\infty R_g T \log\left(\frac{\Gamma_\infty - \Gamma}{\Gamma_\infty}\right). \tag{5.1.2}$$

Upon introducing the concentration scale $\overline{\Gamma} = \Gamma/\Gamma_\infty$, the surface tension term in the dimensionless dynamic boundary condition becomes

$$\frac{\sigma_0}{\Delta p R_0}\left(1 + \frac{\Gamma_\infty R_g T}{\sigma_0}\log\left(1 - \overline{\Gamma}\right)\right) = \frac{1}{We}\left(1 + \alpha \log(1 - \overline{\Gamma})\right), \tag{5.1.3}$$

where the nondimensional parameter $\alpha = \Gamma_\infty R_g T/\sigma_0$ represents the effectiveness of the surfactant, and the Weber number We represents the relative importance of the fluid's inertia compared to surface tension. Given that the concentration of the surfactant ranges between zero and Γ_∞, and thus the dimensionless concentration ranges between zero and one, we have $\log(1 - \overline{\Gamma}) \leqslant 0$. As the parameter α is strictly positive, it can then be seen that an increase in the concentration of the surfactant will always result in a decrease of the surface tension in the system. Additionally, the effectiveness of the surfactant α dictates the rate at which the surface tension decreases with increasing surfactant concentration.

It now remains to introduce the equation governing the concentration of the surfactant at the bubble's free surface. The concentration of the surfactant is governed by (Stone and Leal [1990], Blyth and Pozrikidis [2004])

$$\Gamma_t + \nabla_s \cdot (\Gamma \mathbf{u}_s) + \Gamma(\nabla_s \cdot \widehat{\mathbf{n}})(\mathbf{u} \cdot \widehat{\mathbf{n}}) = S(\Gamma, B_s) + D_s \nabla_s^2 \Gamma, \tag{5.1.4}$$

where $\nabla_s = \nabla - \widehat{\mathbf{n}}(\widehat{\mathbf{n}} \cdot \nabla)$ is the surface gradient operator, $\mathbf{u}_s$ is the tangential velocity, S is the source term of the surfactant as a function of the surfactant concentration and bulk concentration, and D_s is the surface diffusivity of the surfactant. Assuming that the surfactant is insoluble and there is no adsorption $S = 0$, and diffusivity is negligible with $D_s = 0$, the total amount of surfactant on the bubble surface remains constant. Equation 5.1.4 can now be written

$$\frac{\partial \Gamma}{\partial t} + \mathbf{u} \cdot \nabla \Gamma - \Gamma \widehat{\mathbf{n}} \cdot (\widehat{\mathbf{n}} \cdot \nabla)\mathbf{u} = 0. \tag{5.1.5}$$

Using the definition of the material derivative, and the fact that the velocity field of a potential flow can be expressed as $\mathbf{u} = \nabla\phi$, equation 5.1.5 becomes

$$\frac{D\Gamma}{Dt} = \Gamma \widehat{\mathbf{n}} \cdot (\widehat{\mathbf{n}} \cdot \nabla)\nabla\phi. \tag{5.1.6}$$

Given an initial surfactant concentration on the surface of the bubble, Γ_0, we can use a 4^{th} order Runge-Kutta time-stepping scheme to update the concentration at each time step. Upon discretisation of the bubble surface into $N+1$ nodes, we update the surfactant concentration at node j according to

$$\frac{D\Gamma_j}{Dt} = \Gamma_j \frac{\partial^2 \phi_j}{\partial n^2}, \tag{5.1.7}$$

where $\partial^2/\partial n^2$ represents the normal derivative of the normal derivative, which is known at each point on the bubble's surface.

With the modified surface tension term in the dynamic boundary condition and a method to update the concentration at each node at each time step, the boundary integral method can be used as defined in Chapter 2 to study the behaviour of a bubble with a surfactant.

5.2 Numerical results and discussion

Following the addition of the surfactant model to the weakly compressible, viscous boundary integral method, the effect of the presence of a surfactant on bubble oscillation can be measured. Given the application to ultrasonic cleaning, two important cleaning mechanisms will be considered; shape oscillation, and the formation of a liquid jet near to a rigid boundary. In particular, the change to the natural frequency and amplitude of shape mode oscillation given an increasing concentration of surfactant will be calculated, along with changes to the generation of shear stress on the boundary. The threshold for the formation of a liquid jet will be found for different concentrations of surfactant, as well as changes to the velocity of the jet that forms.

The non-ionic surfactant is arbitrarily chosen to be $C_{10}E_8$ as it has been widely studied and the parameters are known (Taylor et al. [2003]). This has a maximum packing concentration $\Gamma_\infty = 2.3$ μmol m^{-2}, with the temperature of the adiabatic system remaining constant at 293.15 K. The bubble has an initial radius of 25 μm. In the absence of a surfactant, the density of the surrounding fluid is $\rho = 998$ kg m^{-3}, the viscosity is $\mu = 10^{-3}$ Pa·s, the surface tension coefficient is $\sigma = 0.073$ N m^{-1}, and the polytropic constant is taken to be $\lambda = 1.4$. The ambient pressure is $p_\infty = 101300$ Pa, and the vapour pressure inside the bubble is $p_v = 2980$ Pa.

5.2.1 Shape mode oscillation with a surfactant

To induce shape oscillation, the initial potential at the surface of the bubble is prescribed to be $\phi_0 = \varepsilon P_l(\cos\theta)$, where $\varepsilon \ll 1$, l is the shape mode number, P_l the Legendre polynomial of order l, and θ the angle between the position on the bubble surface and the x-axis. Figures 5.1 through 5.3 detail how the maximum amplitude of mode two, three and four oscillation changes with an increasing concentration. Figures 5.4 through 5.6 detail how the natural frequency of mode two, three and four oscillation changes with an

increasing concentration.

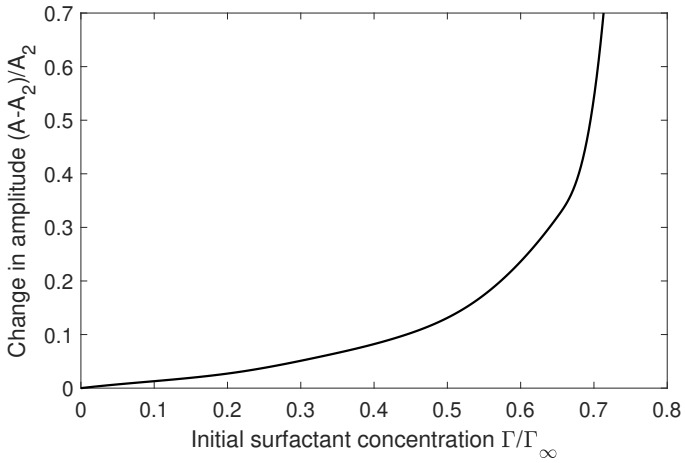

Figure 5.1: The change to the maximum amplitude of shape mode two oscillation A with increasing dimensionless surfactant concentration Γ/Γ_∞, compared to the amplitude in the absence of a surfactant A_2. The bubble has an initial radius of 25 μm. In the absence of a surfactant, the density of the surrounding fluid is $\rho = 998$ kg m^{-3}, the viscosity is $\mu = 10^{-3}$ Pa·s, the surface tension coefficient is $\sigma = 0.073$ N m^{-1}, and the polytropic constant is taken to be $\lambda = 1.4$. The ambient pressure is taken as $p_\infty = 101300$ Pa, and the vapour pressure inside the bubble is $p_v = 2980$ Pa. The non-ionic surfactant is taken to be $C_{10}E_8$, with $\Gamma_\infty = 2.3$ μmol m^{-2}.

As can be seen in figures 5.1-5.3, the maximum amplitude of shape mode oscillation increases exponentially as the concentration of the surfactant increases when compared to an equivalent bubble without a surfactant. Mode two sees a maximum increase of 70%, whereas for mode three this is 50%, and mode four 35%. Additionally, this maximum occurs at a dimensionless concentration of $\Gamma = 0.71$ for mode two, $\Gamma = 0.78$ for mode three, and $\Gamma = 0.79$ for mode four. Above these threshold values the shape oscillation is no longer stable.

As can be seen in figures 5.4-5.6, the natural frequency of shape mode oscillation decreases exponentially as the concentration of the surfactant increases when compared to an equivalent bubble without a surfactant. Mode two sees a maximum decrease of 30%, whereas for mode three this is 20%, and mode four 16%. As before, this maximum occurs

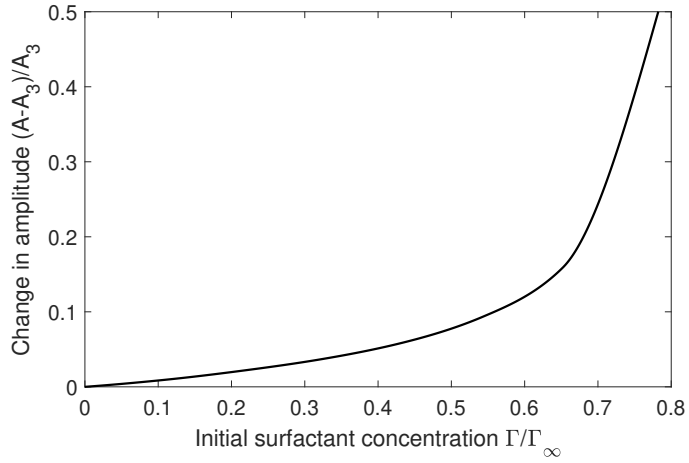

Figure 5.2: The change to the maximum amplitude of shape mode three oscillation A with increasing dimensionless surfactant concentration Γ/Γ_∞, compared to the amplitude in the absence of a surfactant A_3. The parameters are the same as in figure 5.1.

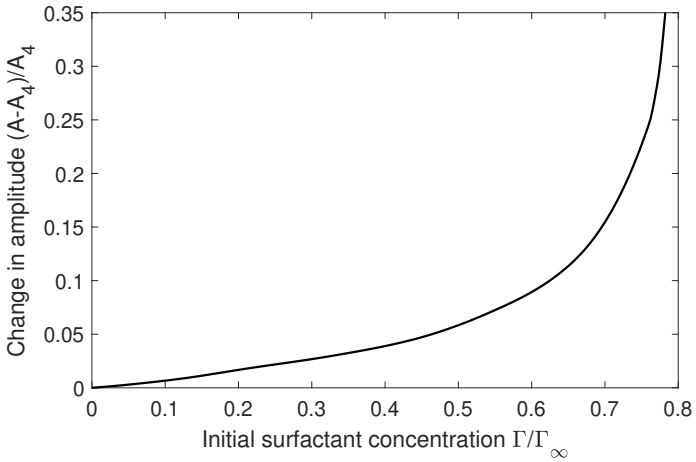

Figure 5.3: The change to the maximum amplitude of shape mode four oscillation A with increasing dimensionless surfactant concentration Γ/Γ_∞, compared to the amplitude in the absence of a surfactant A_4. The parameters are the same as in figure 5.1.

at a dimensionless concentration of $\Gamma = 0.71$ for mode two, $\Gamma = 0.78$ for mode three, and $\Gamma = 0.79$ for mode four. For a more effective surfactant with a larger parameter α, the overall behaviour would be the same, but the stability threshold would be significantly reduced.

These behaviours can be attributed to the decrease in surface tension as the concen-

tration increases. As a smaller proportion of the initial energy is dissipated overcoming surface tension, there is more energy associated with the bubble oscillation leading to a higher maximum amplitude. This in turn leads to a decreasing natural frequency, analogous to the non-linear decrease in natural frequency due to an increasing amplitude of oscillation as in (Tsamopoulos and Brown [1983]).

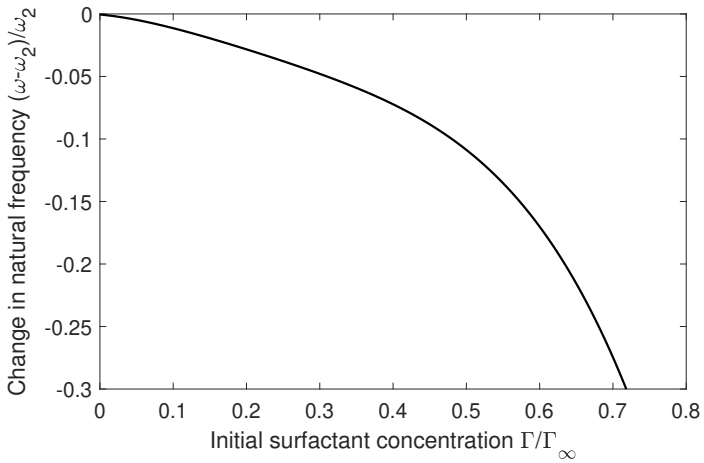

Figure 5.4: The change to the natural frequency of shape mode two oscillation ω with increasing dimensionless surfactant concentration Γ/Γ_∞, compared to the natural frequency in the absence of a surfactant ω_2. The parameters are the same as in figure 5.1.

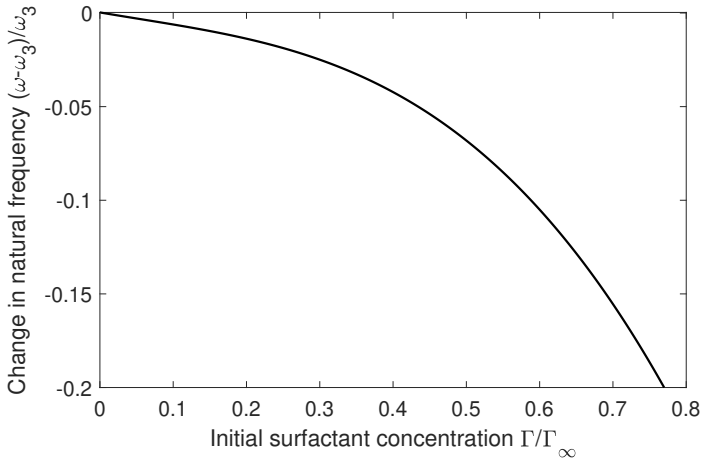

Figure 5.5: The change to the natural frequency of shape mode three oscillation ω with increasing dimensionless surfactant concentration Γ/Γ_∞, compared to the natural frequency in the absence of a surfactant ω_3. The parameters are the same as in figure 5.1.

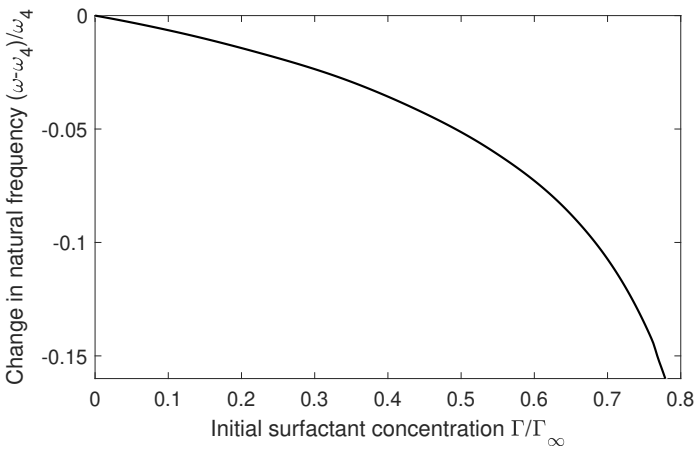

Figure 5.6: The change to the natural frequency of shape mode four oscillation ω with increasing dimensionless surfactant concentration Γ/Γ_∞, compared to the natural frequency in the absence of a surfactant ω_4. The parameters are the same as in figure 5.1.

The relation between the surfactant concentration and the shear stress generated on a rigid boundary by the shape oscillation of a bubble with a surfactant is now presented for modes two through four. As before, an initial potential is prescribed to the surface of the bubble of the form $\phi = \phi_a P_l(\cos\theta)$, where ϕ_a is the amplitude of the initial potential. To ensure a fair comparison, the initial total energy at the surface of the bubble must be kept constant for different concentrations. The potential energy of a bubble depends on the surface tension, which from (Wang and Manmi [2014]) can be given in dimensionless form by

$$E_p = \frac{\varepsilon_p V_0}{\lambda - 1}\left(\frac{V_0}{V}\right)^{\lambda-1} + \sigma S + V, \tag{5.2.1}$$

where S is the surface area of the bubble. Hence, as the total mechanical energy in the system is given by $E_t = E_p + E_k$, the kinetic energy must be increased to account for the decrease in potential energy. With the initial kinetic energy for a bubble undergoing shape mode l oscillation from equation 4.1.7 given by

$$E_k(0) = (l+1)\rho\frac{\phi_a^2}{R_0^{2k+1}}\int_0^{2\pi} P_l^2(\cos\theta)\,\mathrm{d}\theta, \tag{5.2.2}$$

it follows that the initial total energy is given by

$$E_t(0) = V_0\left(1 + \frac{\varepsilon_p}{\lambda - 1}\right) + \frac{1}{We}(1 + \alpha\log(1 - \overline{\Gamma}_0))S_0 + (l+1)\rho\frac{\phi_a^2}{R_0^{2k+1}}\int_0^{2\pi} P_l^2(\cos\theta)\,\mathrm{d}\theta. \tag{5.2.3}$$

With each of these quantities known upon the arbitrary selection of $\overline{\Gamma}_0$, the potential amplitude ϕ_a can be found to ensure that $E_t(0)$ remains constant.

For each mode, the shear stress distribution is calculated for an initial concentration of $\overline{\Gamma}_0 = 0.25$, 0.5, and 0.75. The dimensionless potential amplitudes that satisfy the constant energy requirement for these values are $\phi_a = 0.055$, 0.085, and 0.12 respectively. The initial stand-off distance is chosen to be $\gamma = 1.3$ to compare with the results from figure 4.6 for a bubble close to a boundary. As demonstrated in chapter 4, shape oscillation is only an effective cleaning mechanism when the bubble is close to a rigid boundary. Hence, the stand-off distance must be small. The remaining parameters are the same as in figure 5.1.

As can be seen in figures 5.7 through 5.9, the presence of a surfactant greatly increases

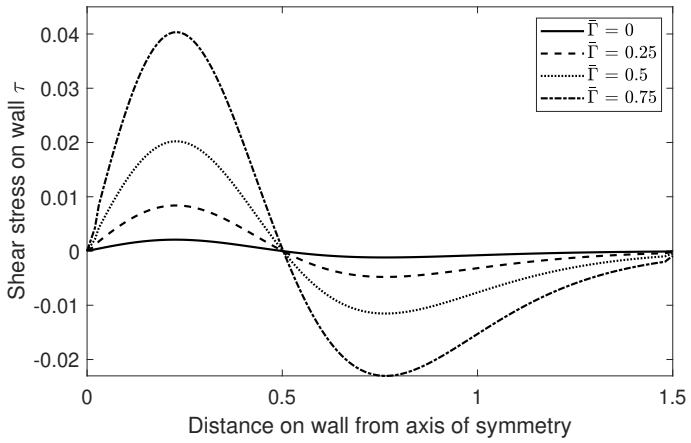

Figure 5.7: The dimensionless shear stress generated on a rigid boundary, located at a stand-off distance of $\gamma = 1.3$, by a bubble in shape mode two oscillation with a surfactant present. Four cases are compared; the initial surfactant concentration $\overline{\Gamma}_0 = 0.0$, 0.25, 0.50 and 0.75. The remaining parameters are the same as in figure 5.1.

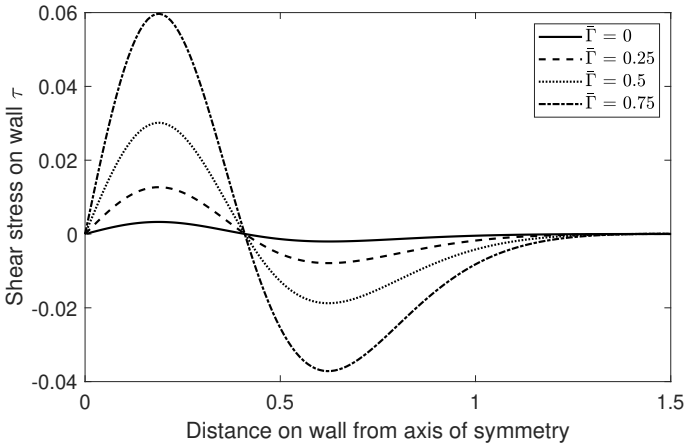

Figure 5.8: The dimensionless shear stress generated on a rigid boundary, located at a stand-off distance of $\gamma = 1.3$, by a bubble in shape mode three oscillation with a surfactant present. Four cases are compared; the initial surfactant concentration $\overline{\Gamma}_0 = 0.0$, 0.25, 0.50 and 0.75. The remaining parameters are the same as in figure 5.1.

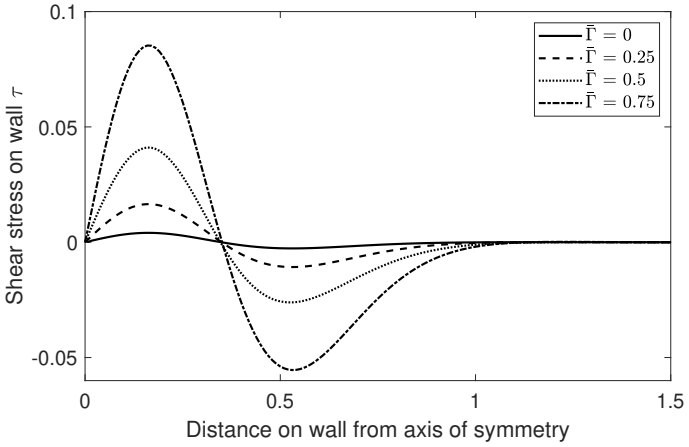

Figure 5.9: The dimensionless shear stress generated on a rigid boundary, located at a stand-off distance of $\gamma = 1.3$, by a bubble in shape mode four oscillation with a surfactant present. Four cases are compared; the initial surfactant concentration $\overline{\Gamma}_0 = 0.0$, 0.25, 0.50 and 0.75. The remaining parameters are the same as in figure 5.1.

the shear stress generated on a rigid boundary by a bubble in shape oscillation. For each mode, the maximum shear stress is increased by a factor of approximately twenty, a significantly large improvement to the cleaning efficiency of the system. The maximum shear stress increases exponentially as the surfactant concentration increases, with a concentration of $\overline{\Gamma}_0 = 0.25$ increasing the stress by a factor of approximately four, and a

concentration of $\overline{\Gamma}_0 = 0.5$ increasing the stress by a factor of approximately ten. Higher modes still generate more shear stress and should prove to be more efficient at cleaning.

The maximum shear stress increasing exponentially with surfactant concentration corresponds with the exponential growth of the amplitude. Again, as there is more energy in the system when surface tension is lower, more energy is transferred to the boundary. With even a small concentration of surfactant, there is a significant increase to the shear stress on the boundary. Given that bubbles are easier to generate, as well as requiring less energy to induce into shape oscillation, it follows that the presence of a surfactant has a significant benefit to ultrasonic cleaning.

5.2.2 Liquid jet formation with a surfactant

Now, the effect of the presence of a surfactant on the formation and behaviour of liquid jets is considered. The energy threshold for jet formation, as well as the jet speed are to be studied against the initial concentration of the surfactant. In addition, bubble shapes during jet formation with and without a surfactant will be compared. A bubble in water with initial radius 25 μm is considered, with the rest of the parameters as in figure 5.1.

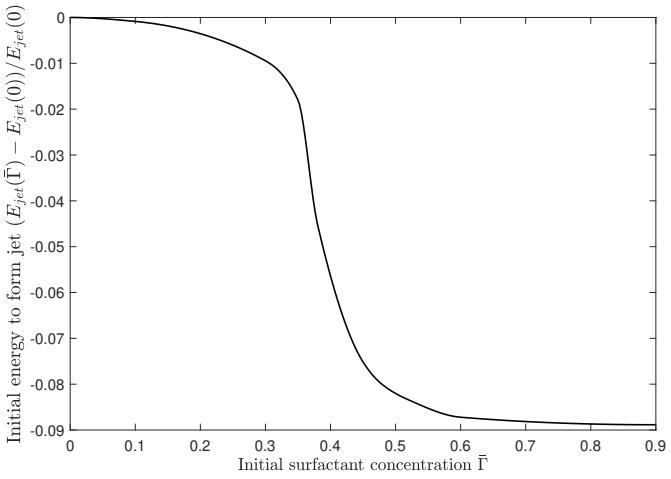

Figure 5.10: The change in initial energy at the surface of a bubble required to form a liquid jet in the first cycle of oscillation $E_{jet}(\overline{\Gamma})$, against the initial concentration of surfactant $\overline{\Gamma}_0$. The parameters are the same as in figure 5.1.

In figure 5.10, the change in initial energy required to form a liquid jet $E_{jet}(\overline{\Gamma})$ is found for differing initial surfactant concentrations. The energy threshold is found following the numerical calculation of the total energy. It is found that the presence of a surfactant decreases the energy required to form a liquid jet by up to 9%. Initially, as the concentration of the surfactant is increased, there is only a small decrease in the energy threshold up until a concentration of approximately $\overline{\Gamma}_0 = 0.3$. In the region between $\overline{\Gamma}_0 = 0.3$ and 0.5, however, there is a significant rapid decrease in the energy threshold. For $\overline{\Gamma}_0 \geq 0.5$, there is only a small decrease and the system approaches its limit. This behaviour can be explained by the increased energy in the system given the presence of a surfactant, as less is dissipated to overcome surface tension.

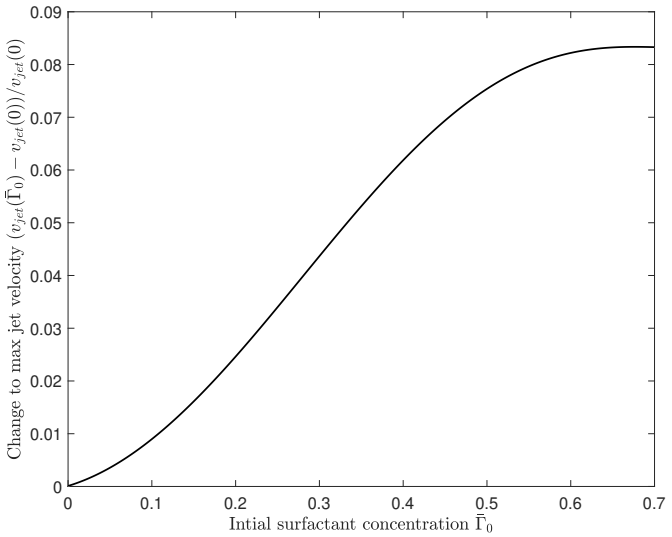

Figure 5.11: The change in the maximum jet velocity of a bubble, with initial radius 25 μm and initial dimensionless velocity potential ϕ_0 = -1.5, against the initial concentration of surfactant $\overline{\Gamma}_0$. The remaining parameters are the same as in figure 5.1.

Next, the velocity of the liquid jet that forms is considered. The same case as in figure 5.10 is considered, with an initial dimensionless potential ϕ_0 = -1.5 to induce a liquid jet. As is seen in figure 5.11, the presence of a surfactant increases the maximum velocity of a liquid jet up to a maximum of approximately 8.5%. The jet velocity increases in a close

to linear fashion for an initial surfactant concentration $\overline{\Gamma}_0 \leq 0.5$, before tailing off as as the system approaches its limit for $\overline{\Gamma}_0 \geq 0.6$. As the surface tension decreases with an increasing concentration, the force due to surface tension acting against the motion of the jet is reduced. Thus, the jet reaches a higher maximum velocity.

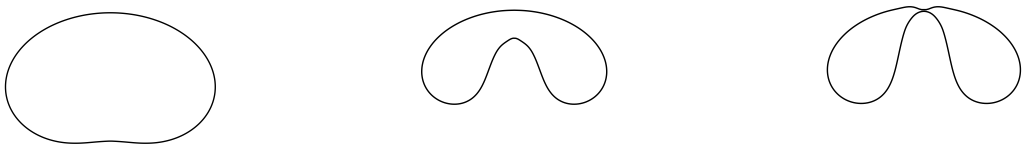

Figure 5.12: Bubble shapes during the collapse of a bubble with a liquid jet. No surfactant is present. The parameters are the same as in figure 5.11.

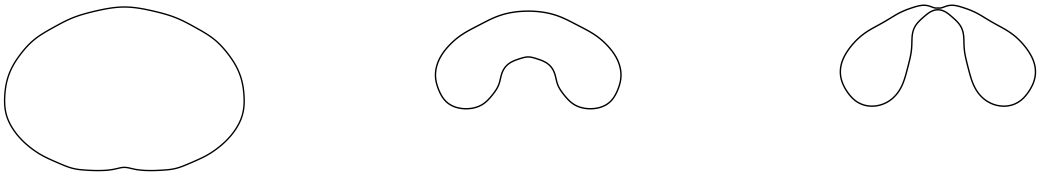

Figure 5.13: Bubble shapes during the collapse of a bubble with a liquid jet. A surfactant is present with initial concentration $\overline{\Gamma}_0 = 0.75$. The remaining parameters are the same as in figure 5.11.

Figures 5.12 and 5.13 show the formation of a liquid jet and subsequent collapse of a bubble with initial radius 25 μm and initial dimensionless potential ϕ_0 = -1.5, with remaining parameters as in figure 5.1, for a bubble without a surfactant, and a bubble with an initial surfactant concentration of $\overline{\Gamma}_0 = 0.75$. The presence of a surfactant has two main effects on the shape of the bubble. Firstly, the surface of the bubble is more irregular, almost bumpy in appearence. With the effect of surface tension much weaker,

the bubble is no longer working as hard to return to a spherical shape. Additionally, some areas on the bubble surface will have a higher concentration of surfactant than others. This leads to a non-uniform distribution of surface tension, and so due to the Marangoni effect fluid will flow away from regions of low surface tension towards regions of high surface tension. This can lead to a non-uniform surface. Secondly, the jet is wider, without a pronounced jet tip. This is due to the reduced effect of surface tension working to minimise the surface area.

Chapter 6

Conclusions and future work

6.1 Conclusions

6.1.1 Microbubble dynamics with viscous and compressible effects, and subject to an acoustic wave

The weakly compressible, viscous boundary integral method is validated against, analytical, numerical, and experimental results. The importance of viscous and compressible effects is demonstrated, as well as their importance to accurately modelling multiple cycles of oscillation. Excellent agreement is achieved in each comparison for a variety of different cases.

First, the BIM was compared with spherical bubble theory, namely the Gilmore model, along with experimental results. Here, a microbubble with an initial radius of 8.1 μm in water was subject to an acoustic wave with amplitude 132 kPa and frequency 21.4 kHz. The bubble undergoes a large slow expansion followed by multiple small fast oscillations. Very good agreement is achieved with the radius history for six cycles of oscillation, before non-linear shape mode oscillation forms and the bubble collapses.

Next, the BIM was compared to experimental results in which a bubble was subject to a modulated acoustic wave inducing shape mode three oscillation. The bubble, initiated

in water, had initial radius 67 μm, with the wave with frequency 33.2 kHz and amplitude 15.6 kPa modulated at 100 Hz. Accurate bubble shapes in shape mode three oscillation were found with excellent agreement with the experimental results, even after many cycles of oscillation. Additionally, the radius history agrees well with that observed in the experiment. Here, viscous effects proved to be important to find accurate bubble shapes.

Comparing to the asymptotic results of (Shaw [2017]), in which viscous and compressible effects are important, further demonstrates the ability of the VCBIM to accurately model these effects. A bubble with an initial radius of 144 μm was subject to an acoustic wave with pressure amplitude 13 kPa and frequency 10 kHz, inducing shape mode three oscillation. Excellent agreement was achieved with the bubble shapes.

When compared to the numerical results of (Tsiglifis and Pelekasis [2005]), in which an elongated bubble with equilibrium radius 5.8 μm is modelled in a viscous liquid with inverse Ohnesorge number $Oh^{-1} = 1000$, the VCBIM achieves very good agreement. The importance of viscous is demonstrated, with the formation of a wider jet due to viscous effects.

Finally, four cases are considered based on the numerical results in (Wang et al. [2022]). The ninth minimum expansion is considered including both viscous and compressible effects, only viscous effects, only compressible effects, and neither compressible nor viscous effects. It is shown that including compressible effects leads to the formation of a smaller jet, due to the energy loss through the shock-wave emission associated with compressible effects. Additionally, it is shown that viscous effects lead to a more regular shape and smaller jet, given viscous dissipation.

Thus, it has been shown that the VCBIM can accurately model bubble behaviour over multiple cycles of oscillation. The inclusion of viscous and compressible effects is crucial for finding accurate bubble shapes after multiple cycles.

6.1.2 Shape oscillation of a bubble near a rigid boundary

A numerical model is described for the shape mode oscillation of a bubble near to as well as connected to a rigid boundary. It is based on the boundary integral method, with the viscous effects modelled using viscous potential flow theory and the compressible effects using weakly compressible theory. The viscous stress at the boundary is approximated using boundary layer theory. Parametric studies are carried out for the natural frequency of shape modes and the shear stress at the rigid boundary in terms of the shape modes and the standoff distance of the bubble from the boundary. A series of new features have been noticed, which may be summarized as follows.

The natural frequency of shape mode oscillation of a bubble near a rigid boundary is decreased by the presence of the boundary. The wall effects decrease as the standoff distance increases, and the larger the mode number, the faster the wall effects decrease. The maximum decreases in the natural frequency for modes $k = 0$ (spherical mode), 2, 3, 4 are 21%, 30%, 29% and 14%.

As a bubble oscillates with shape modes either very close to or in contact with a rigid boundary, significant shear stress occurs only within approximately 1.5 R_{eq} from the axis of symmetry, with the maximum value of shear stress located within the image of the projection of the bubble onto the wall. The shear stress at the rigid boundary decreases when the standoff distance of the bubble from the boundary increases. The shear stress due to shape oscillation decreases faster with the standoff distance than that due to the volume oscillation of bubbles. The larger the shape mode the faster the shear stress decreases with the standoff distance.

In particular, the magnitude of the shear stress due to shape oscillation for a bubble very close to the rigid boundary is at least twenty times larger than that due to spherical oscillation with the same energy. This is because the shape mode oscillation of bubbles generates more local streaming and stress in comparison to volume oscillation of a bubble

at the same energy. This explains the dramatic cleaning effects of a bubble oscillating with shape modes in very close proximity to a rigid boundary, the experimental findings of Vyas et al. [2020], in which the bubble only cleans the area directly near to the bubble surface.

These results are consistent with the order analysis based on the perturbation theory. The induced velocity due to shape mode k is $\mathcal{O}(r^{-(k+2)})$, decaying faster for a larger mode k. For the non-spherical shape modes, i.e. $k \geq 2$, the induced velocity decreases much faster than that of spherical oscillation ($k = 0$). The disturbance of shape oscillation to the flow decays much faster away from the bubble than that of spherical oscillation. As such, the wall effects for shape mode oscillation decrease with the standoff distance much faster than spherical oscillation; the higher the shape mode k the faster the decrease.

The shear stress at the rigid boundary due to shape mode k is $\mathcal{O}(r^{-3(k+3)})$ using equation 4.1.3, decaying faster with the standoff distance than the induced velocity. This confirms the local nature of the shear stress at the rigid boundary due to shape oscillation.

6.1.3 Microbubble dynamics subject to a surfactant

The presence of a surfactant significantly impacts the shape mode oscillation of a bubble, leading to a large improvement to the efficiency of ultrasonic cleaning. The energy required to induce shape oscillation is lower due to a reduction in the surface tension. In addition, the maximum shear stress generated on a rigid boundary is increased by a factor of up to twenty times.

As the initial surfactant concentration increases, the maximum amplitude of shape oscillation increases exponentially. Shape mode two oscillation sees a maximum increase of 70%, mode three 50%, and mode four 35%. The threshold concentration above which each mode is no longer stable is $\overline{\Gamma}_0 = 0.71,\ 0.78,\ 0.79$ for modes two, three and four respectively. Surfactants with a different effectiveness parameter α exhibit the same be-

haviour, just shifted such that the stability threshold decreases as α increases.

As the initial surfactant concentration increases, the natural frequency of shape oscillation decreases exponentially. Shape mode two oscillation sees a maximum decrease of 30%, mode three 20%, and mode four 16%. The increase to amplitude and subsequent decrease in natural frequency are a consequence of the decreased surface tension. With less energy required to overcome surface tension, the bubble is free to expand further. With a larger amplitude, it follows that the natural frequency will decrease.

Increasing the surfactant concentration leads to an exponential increase in the shear stress generated on a nearby rigid boundary by a bubble in shape oscillation. A concentration of $\overline{\Gamma}_0 = 0.25$ leads to a factor four increase, $\overline{\Gamma}_0 = 0.50$ a factor ten increase, and $\overline{\Gamma}_0 = 0.75$ a factor twenty increase. This is due to the fact that a lower surface tension results in a lower potential energy, so given that the initial total mechanical energy is kept constant, the initial kinetic energy will be increased. Thus, more energy is transferred to the boundary rather than dissipated overcoming surface tension.

As the amplitude increases exponentially with concentration, the distance between the bubble wall and the boundary decreases. Hence, it follows that the generated shear stress will also increase exponentially given it has been shown that the order of magnitude of shear stress increases exponentially as the distance decreases at a rate of $\mathcal{O}(r^{-3(k+3)})$ for mode k, where r is the distance of the bubble from the boundary.

The presence of a surfactant has a number of effects on the formation of a liquid jet during bubble collapse. Firstly, the threshold initial energy required for the jet to form is reduced by up to 9% as the initial surfactant concentration increases. Secondly, the jet velocity increases by up to 8.5% as the concentration increases. Finally. the shape of the bubble during collapse is changed, with a non-uniform surface and the formation of a wider jet. These effects can be attributed to the increased energy in the system, and reduced surface tension.

6.2 Future developments

6.2.1 Development of perturbation theory

The perturbation theory for a translating bubble in shape mode oscillation when a small distance away from a rigid boundary will be developed. A bubble in shape oscillation in an infinite liquid was studied by Plesset [1954] and Prosperetti [1977], using perturbation methods and spherical harmonic functions. This has been extended for a bubble in the presence of a rigid boundary by Maksimov [2020]. In collaboration with Shanghai Jiatong University, the Birmingham research group has further developed this work for encapsulated bubbles (Liu and Wang [2016], Liu et al. [2017], Liu et al. [2018]).

The perturbation theory for bubbles in shape oscillation near a rigid boundary will be developed by including the translation velocity of a bubble as well as the viscous effects. The translation of a bubble will be modelled by incorporating a term Ux in the expansion of the velocity potential, where U is the translational velocity, and the x-axis is the direction of translation. The viscous effects will be modelled by the viscous potential flow theory (Joseph and Wang [2004]; Wang et al. [2022]).

The natural frequency of the shape modes of a bubble near a rigid boundary will be studied and characterised in terms of the Reynolds number, the Weber number, the standoff distance of the bubble to the rigid boundary, as well as the translation velocity. Additionally, the viscous shear stress at the boundary will be investigated, which is approximated using boundary layer theory (Nyborg [1958]).

6.2.2 3D computational capacity

A three-dimensional (3D) computational capability for bubbles in shape mode oscillation near and over a rigid boundary will be developed. The capability will be based on the integration of the advanced 3D BEM bubble code of the Birmingham bubble group (Wang

and Manmi [2014], Wang et al. [2020]). This modelling is grid free in the flow domain, accurate and stable for dozens of cycles of oscillation, and thus ideal for modelling the phenomenon. The wall effect is modelled using the method of images. As a bubble is in contact with the wall, a thin layer of liquid exists between the bubble and the wall (Wang et al. [2015]). Consequently, this can be approximated by removing this thin layer of liquid and combining the bubble with its image to the wall, as shown in figure 6.1. As the bubble surface is in contact with the rigid boundary, the contact angle of the liquid-gas interface with the rigid boundary depends on the properties of the liquid, gas and the hydrophilic property of the boundary and may change with the dynamics. The

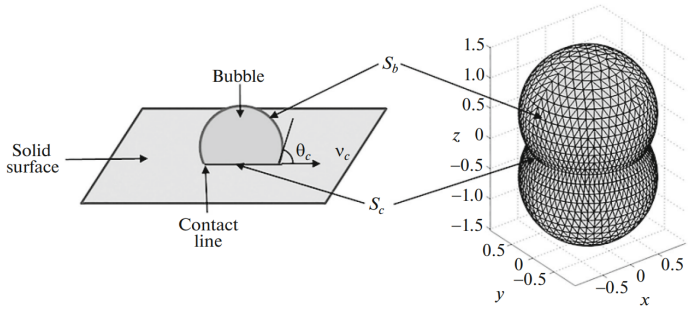

Figure 6.1: A microbubble initiated on a rigid boundary with contact angle θ_c, and the geometry of the mesh used to describe the bubble surface (Abramova et al. [2018]).

computational capability will be evaluated using theoretical results obtained in phase 1 for bubbles a small distance away from the rigid wall. This in turn also provides the threshold of the standoff distance over which the theory provides a good approximation. This will develop 3D theory and computational capability for translating bubbles in shape oscillation on a rigid boundary. The natural frequency of the shape modes and viscous shear stress at the rigid boundary will be characterised. With these developments, the proposed plan is to develop the understanding of the cleaning mechanisms, namely, the interaction between the shape oscillation and translation, and removal of the bio-film from the boundary.

Appendix A
Cubic spline calculation

Note that the cumulative arc-length along the surface is defined as the sum of the arc-length of each segment, from node $k = 1, \ldots, j$, i.e.

$$\xi_j = \sum_{k=1}^{j-1} |S_k|, \quad \text{for } \; j = 2, \ldots, N+1, \tag{A.0.1}$$

where ξ_j represents the cumulative arc-length up to node j, and $|S_k|$ represents the arc-length of segment S_k. We note that $\xi_1 = 0$. As the exact profile of the segments is unknown, and the segments themselves are very small, the arc-length of segment k is approximated as:

$$|S_k| = \sqrt{(r_{k+1} - r_k)^2 + (z_{k+1} - z_k)^2}, \quad \text{for } \; k = 1, \ldots, N. \tag{A.0.2}$$

We have the set of data points $\{\xi_1, \xi_2, \ldots, \xi_N, \xi_{N+1}\}$ representing the cumulative arc-length at each node, and the corresponding data set $\{y_1, y_2, \ldots, y_N, y_{N+1}\}$. Here, y_j represents the known data at each node, used as a placeholder to be replaced by one of r_j, z_j, and ϕ_j. We are looking for an interpolating piecewise polynomial function $F(\xi)$ of the form:

$$F(\xi) = \begin{cases} f_1(\xi) & \text{if} \quad \xi_1 \leqslant \xi < \xi_2; \\ f_2(\xi) & \text{if} \quad \xi_2 \leqslant \xi < \xi_3; \\ & \vdots \\ f_N(\xi) & \text{if} \quad \xi_N \leqslant \xi \leqslant \xi_{N+1}, \end{cases} \tag{A.0.3}$$

where for $i = 1, \ldots, N$ we have

$$f_i(\xi) = a_i(\xi - \xi_i)^3 + b_i(\xi - \xi_i)^2 + c_i(\xi - \xi_i) + d_i. \tag{A.0.4}$$

We note that upon differentiation, we have:

$$f_i'(\xi) = 3a_i(\xi - \xi_i)^2 + 2b_i(\xi - \xi_i) + c_i, \tag{A.0.5}$$

$$f_i''(\xi) = 6a_i(\xi - \xi_i) + 2b_i, \tag{A.0.6}$$

for $i = 1, \ldots, N$. We require a number of restrictions to ensure a smooth interpolation. There are four conditions that need to be satisfied:

- $F(\xi)$ interpolates all data points,
- $F(\xi)$ is continuous on the interval $[\xi_1, \xi_{N+1}]$,
- $F'(\xi)$ is continuous on the interval $[\xi_1, \xi_{N+1}]$,
- $F''(\xi)$ is continuous on the interval $[\xi_1, \xi_{N+1}]$.

The first condition yields the restraint that $F(\xi_i) = y_i$ for $i = 1, \ldots, N+1$. We note that since $\xi_i \in [\xi_i, \xi_{i+1})$, $F(\xi_i) = f_i(\xi_i)$ for $i = 1, \ldots, N$. This means that we have

$$y_i = f_i(\xi_i) = a_i(\xi_i - \xi_i)^3 + b_i(\xi_i - \xi_i)^2 + c_i(\xi_i - \xi_i) + d_i = d_i, \tag{A.0.7}$$

for each $i = 1, \ldots, N$.

If $F(\xi)$ is to be continuous across the entire interval, we require that each sub-function must be equal at each data point. Hence, we say that

$$f_i(\xi_i) = f_{i-1}(\xi_i) \quad \text{for} \quad i = 2, \ldots, N. \tag{A.0.8}$$

We have already found

$$f_i(\xi_i) = d_i \quad \text{and} \quad f_{i-1}(\xi_i) = a_{i-1}(\xi_i - \xi_{i-1})^3 + b_{i-1}(\xi_i - \xi_{i-1})^2 + c_{i-1}(\xi_i - \xi_{i-1}) + d_{i-1}, \tag{A.0.9}$$

so we have the condition that

$$d_i = a_{i-1}h_{i-1}^3 + b_{i-1}h_{i-1}^2 + c_{i-1}h_{i-1} + d_{i-1} \quad \text{for} \quad i = 2, \ldots, N, \tag{A.0.10}$$

noting that $h_{i-1} = \xi_i - \xi_{i-1}$.

We also require that the derivatives are equal at the data points to satisfy continuity of derivative. Hence, we have:

$$f_i'(\xi_i) = f_{i-1}'(\xi_i) \quad \text{for} \quad i = 2, \ldots, N. \tag{A.0.11}$$

From (A.0.5), we find for $i = 2, \ldots, N$ that

$$f_i'(\xi_i) = c_i, \tag{A.0.12}$$

$$f_{i-1}'(\xi_i) = 3a_{i-1}h_{i-1}^2 + 2b_{i-1}h_{i-1} + c_{i-1}. \tag{A.0.13}$$

Thus,

$$3a_{i-1}h_{i-1}^2 + 2b_{i-1}h_{i-1} + c_{i-1} = c_i, \tag{A.0.14}$$

for $i = 2, \ldots, N$.

To satisfy the condition of continuity of the second derivative we require :

$$f_i''(\xi_i) = f_{i-1}''(\xi_i) \quad \text{for} \quad i = 2, \ldots, N. \tag{A.0.15}$$

We find from (A.0.6) that

$$f_i''(\xi_i) = 2b_i, \tag{A.0.16}$$

$$f_{i-1}''(\xi_i) = 6a_{i-1}h_{i-1} + 2b_{i-1}, \tag{A.0.17}$$

for $i = 2, \ldots, N$. Thus it follows that

$$2b_i = 6a_{i-1}h_{i-1} + 2b_{i-1} \quad \text{for} \quad i = 2, \ldots, N. \tag{A.0.18}$$

For simplicity, we set $f_i''(\xi_i) = M_i$. Then $M_i = 2b_i$, and so $b_i = \frac{M_i}{2}$. Given that we know $b_i = \frac{M_i}{2}$ and $d_i = y_i$, we now want to find expressions for the other coefficients in terms of y_i and M_i. Beginning with a_i, we have from the expression (A.0.18)

$$2b_{i+1} = 6a_ih_i + 2b_i \quad \text{for} \quad i = 1, \ldots, N-1, \tag{A.0.19}$$

which upon rearranging and substituting for b_i becomes:

$$a_i = \frac{M_{i+1} - M_i}{6h_i} \quad \text{for} \quad i = 1, \ldots, N-1. \tag{A.0.20}$$

Then, looking for c_i, we have from (A.0.10) that

$$d_{i+1} = a_ih_i^3 + b_ih_i^2 + c_ih_i + d_i \quad \text{for} \quad i = 1, \ldots, N-1. \tag{A.0.21}$$

Again rearranging and substituting for the known a_i, b_i and d_i, we find

$$c_i = \frac{y_{i+1} - y_i}{h_i} - \left(\frac{M_{i+1} + 2M_i}{6}\right) h_i \quad \text{for} \quad i = 1, \ldots, N-1. \tag{A.0.22}$$

We now have the following system:

$$\begin{cases} a_i = \frac{M_{i+1} - M_i}{6h_i}, \\ b_i = \frac{M_i}{2}, \\ c_i = \frac{y_{i+1} - y_i}{h_i} - \left(\frac{M_{i+1} + 2M_i}{6}\right) h_i, \\ d_i = y_i, \end{cases} \tag{A.0.23}$$

for $i = 1, \ldots, N-1$.

Now, we want to eliminate the coefficient terms and solve for the unknowns M_i. To do this, we begin with (A.0.14),

$$c_{i+1} = 3a_ih_i^2 + 2b_ih_i + c_i \quad \text{for} \quad i = 1, \ldots, N-1. \tag{A.0.24}$$

Substituting from (A.0.23) yields:

$$3\left(\frac{M_{i+1} - M_i}{6h_i}\right) h_i^2 + 2\left(\frac{M_i}{2}\right) h_i + \frac{y_{i+1} - y_i}{h_i} - \left(\frac{M_{i+1} + 2M_i}{6}\right) h_i$$

$$= \frac{y_{i+2} - y_{i+1}}{h_{i+1}} - \left(\frac{M_{i+2} + 2M_{i+1}}{6}\right) h_{i+1} \quad \text{for} \quad i = 1, \ldots, N-1. \tag{A.0.25}$$

This reduces to:

$$M_i h_i + M_{i+1}(2(h_i + h_{i+1})) + M_{i+2} h_{i+1} = 6\left(\frac{y_{i+2} - y_{i+1}}{h_{i+1}} - \frac{y_{i+1} - y_i}{h_i}\right) \quad \text{for} \quad i = 1, \ldots, N-1. \tag{A.0.26}$$

This can be written as a matrix of the form

$$\mathbf{Hm} = \mathbf{y}, \tag{A.0.27}$$

where for $i = 1, \ldots, N-1$ and $j = 1, \ldots, N+1$:

$$\mathbf{H} = (H_{ij}) = \begin{cases} h_i & \text{if } j = i, \text{ for } i = 1, \ldots, N-1; \\ 2(h_i + h_j) & \text{if } j = i+1, \text{ for } i = 1, \ldots, N-1; \\ h_{i+1} & \text{if } j = i+2, \text{ for } i = 1, \ldots, N-1; \\ 0 & \text{otherwise,} \end{cases} \tag{A.0.28}$$

$$\mathbf{m} = (M_j), \qquad \text{for } j = 1, \ldots, N+1, \tag{A.0.29}$$

$$\mathbf{y} = (\tilde{y}_i), \text{ where } \tilde{y}_i = 6\left(\frac{y_{i+2} - y_{i+1}}{h_{i+1}} - \frac{y_{i+1} - y_i}{h_i}\right) \quad \text{for } i = 1, \ldots, N-1. \tag{A.0.30}$$

This can be represented equivalently as:

$$\begin{pmatrix} h_1 & 2(h_1+h_2) & h_2 & 0 & \cdots & 0 \\ 0 & h_2 & 2(h_2+h_3) & \ddots & \vdots & \vdots \\ \vdots & \vdots & \ddots & \ddots & h_{N-1} & 0 \\ 0 & 0 & \cdots & h_{N-1} & 2(h_{N-1}+h_N) & h_N \end{pmatrix} \begin{pmatrix} M_1 \\ M_2 \\ \vdots \\ M_N \\ M_{N+1} \end{pmatrix} = \begin{pmatrix} \tilde{y}_1 \\ \tilde{y}_2 \\ \vdots \\ \tilde{y}_{N-2} \\ \tilde{y}_{N-1} \end{pmatrix}, \tag{A.0.31}$$

This is a system with $N-1$ rows and $N+1$ columns, consequently leaving the system under-determined by two equations. Hence, we require two more conditions to find a unique cubic spline.

To determine the required additional equations, we note that both $\phi(\xi)$ and $z(\xi)$ are symmetric about the axis of symmetry. This means that they are required to have zero first derivative on the axis of symmetry. These are called clamped splines. Given that $r(\xi)$ is antisymmetric, it has second derivative equal to zero on the axis of symmetry. This is called a natural spline.

Natural Splines

A natural spline has a zero second derivative on the axis of symmetry, i.e. $M_1 = M_{n+1} = 0$. This allows us to exclude the first and last column, as they correspond to the M_1 and M_{n+1} values. Imposing this condition, and replacing the placeholder data set y_j with data

set $\{r_1, \ldots, r_{n+1}\}$, allows us to write the matrix system as

$$\begin{pmatrix} 2(h_1+h_2) & h_2 & \cdots & 0 \\ h_2 & 2(h_2+h_3) & \ddots & \vdots \\ \vdots & \ddots & \ddots & h_{N-1} \\ 0 & \cdots & h_{N-1} & 2(h_{N-1}+h_N) \end{pmatrix} \begin{pmatrix} M_2 \\ \vdots \\ M_N \end{pmatrix} = \begin{pmatrix} \tilde{y}_1 \\ \vdots \\ \tilde{y}_{N-1} \end{pmatrix}. \quad \text{(A.0.32)}$$

This is a system of $N-1$ equations with $N-1$ unknowns, and can now be solved. The matrix is tri-diagonal and the system can be solved for M_i using the Thomas algorithm Press et al. [1988], a simplification of Gaussian elimination, which will find the values of M_i for $i = 2, \ldots, N$. We then find the spline coefficients upon substitution into (A.0.23). Thus, we will have an interpolated function describing the r coordinate of the whole bubble surface.

Clamped Splines

A clamped spline has a zero first derivative on the axis of symmetry. Hence we have

$$f_1'(\xi_1) = 0, \quad f_{N+1}'(\xi_{N+1}) = 0. \quad \text{(A.0.33)}$$

From the first condition, and the definition of $f(\xi)$ from (A.0.7), we deduce that

$$f_1'(\xi_1) = 3a_1(\xi_1 - \xi_1)^2 + 2b_1(\xi_1 - \xi_1) + c_1 = c_1 = 0. \quad \text{(A.0.34)}$$

From (A.0.23) we can then write a new condition for the first spline,

$$h_1 M_2 + 2h_1 M_1 = \frac{6}{h_1}(y_2 - y_1). \quad \text{(A.0.35)}$$

This can be added to the matrix to provide another condition. Similarly for the second condition we have

$$f_N'(\xi_{N+1}) = 3a_N h_N^2 + 2b_N h_N + c_N = 0. \quad \text{(A.0.36)}$$

Rearranging and substituting from (A.0.23) gives the second new condition:

$$h_N M_N + 2h_N M_{N+1} = \frac{6}{h_N}(y_N - y_{N+1}). \quad \text{(A.0.37)}$$

These two conditions can be simply added to our previous system to receive a determined system of equations, given by

$$\begin{pmatrix} 2h_1 & h_1 & 0 & \cdots & 0 \\ h_1 & 2(h_1+h_2) & h_2 & \cdots & 0 \\ \vdots & \ddots & \ddots & \ddots & \vdots \\ 0 & \cdots & h_{N-1} & 2(h_{N-1}+h_N) & h_N \\ 0 & \cdots & 0 & h_N & 2h_N \end{pmatrix} \begin{pmatrix} M_1 \\ \vdots \\ M_{N+1} \end{pmatrix} = \begin{pmatrix} \frac{6(y_2-y_1)}{h_1} \\ \tilde{y}_1 \\ \vdots \\ \tilde{y}_{N-1} \\ \frac{6(y_N-y_{N-1})}{h_N} \end{pmatrix}. \tag{A.0.38}$$

This is now a a system with $N+1$ equations and $N+1$ unknowns that can now be solved. Again, this system is solved using the Thomas algorithm to find the spline coefficients.

List of References

[1] O. A. Abramova, I. Sh. Akhatov, N. A. Gumerov, Yu. A. Pityuk, and S. P. Sametov. Numerical and experimental study of bubble dynamics in contact with a solid surface. *Fluid Mechanics*, 53(3):337–346, 2018.

[2] S. B. Awad and N. F. Awad. Chapter 6 - The Role of Surfactants in Ultrasonic Cleaning: Nanoparticle Removal and Other Challenging Applications. In *Surfactants in Precision Cleaning*, pages 227–271. Elsevier, 2022. ISBN 978-0-12-822216-4.

[3] C. K. Batchelor and G. K. Batchelor. *An Introduction to Fluid Dynamics*. Cambridge Mathematical Library. Cambridge University Press, 2000. ISBN 9780521663960.

[4] T. B. Benjamin and A. T. Ellis. The Collapse of Cavitation Bubbles and the Pressures thereby Produced against Solid Boundaries. *Philosophical Transactions of the Royal Society of London Series A*, 260(1110):221–240, July 1966.

[5] J. Best. The formation of toroidal bubbles upon the collapse of transient cavities. *Journal of Fluid Mechanics*, 251:79 – 107, 06 1993.

[6] J. P. Best and A. Kucera. A numerical investigation of non-spherical rebounding bubbles. *Journal of Fluid Mechanics*, 245:137–154, 1992.

[7] J. R. Blake and D. C. Gibson. Growth and collapse of a vapour cavity near a free surface. *Journal of Fluid Mechanics*, 111:123–140, 1981.

[8] J. R. Blake and D. C. Gibson. Cavitation bubbles near boundaries. *Annual Review of Fluid Mechanics*, 19(1):99–123, 1987.

[9] J. R. Blake, B. B. Taib, and G. Doherty. Transient cavities near boundaries. Part 1. Rigid boundary. *Journal of Fluid Mechanics*, 170:479–497, 1986.

[10] M. G. Blyth and C. Pozrikidis. Evolution equations for the surface concentration of an insoluble surfactant; applications to the stability of an elongating thread and a stretched interface. *Theoretical and Computational Fluid Dynamics*, 17(3):147–164, 2004.

[11] J. M. Boulton-Stone and J. R. Blake. Gas bubbles bursting at a free surface. *Journal of Fluid Mechanics*, 254:437–466, 1993.

[12] C. E. Brennen and D. M. E. C. E. Brennen. *Cavitation and Bubble Dynamics*. Oxford engineering science series. Oxford University Press, 1995. ISBN 9780195094091.

[13] Howard Brenner. *Interfacial transport processes and rheology*. Elsevier, 2013.

[14] M. P. Brenner, S. Hilgenfeldt, and D. Lohse. Single-bubble sonoluminescence. *Rev. Mod. Phys.*, 74:425–484, May 2002.

[15] E. Brujan and Y. Matsumoto. Collapse of micrometer-sized cavitation bubbles near a rigid boundary. *Microfluidics and Nanofluidics*, 13, 12 2012.

[16] T. J. Bulat. Macrosonics in industry: 3. Ultrasonic cleaning. *Ultrasonics*, 12(2):59 – 68, 1974. ISSN 0041-624X.

[17] J. C. Butcher. Coefficients for the study of Runge-Kutta integration processes. *Journal of the Australian Mathematical Society*, 3(2):185–201, 1963.

[18] G. L. Chahine, A. Kapahi, J. K. Choi, and C. T. Hsiao. Modeling of surface cleaning by cavitation bubble dynamics and collapse. *Ultrasonics Sonochemistry*, 29:528–549, 2016. ISSN 1350-4177.

[19] C.-H. Chang and E. I. Franses. Adsorption dynamics of surfactants at the air/water interface: a critical review of mathematical models, data, and mechanisms. *Colloids and Surfaces A: Physicochemical and Engineering Aspects*, 100:1–45, 1995.

[20] J. Collis, R. Manasseh, P. Liovic, P. Tho, A. Ooi, K. Petkovic-Duran, and Y. Zhu. Cavitation microstreaming and stress fields created by microbubbles. *Ultrasonics*, 50(2):273 – 279, 2010. ISSN 0041-624X. Selected Papers from ICU 2009.

[21] C. C. Coussios and R. A. Roy. Applications of acoustics and cavitation to noninvasive therapy and drug delivery. *Annual Review of Fluid Mechanics*, 40:395–420, 2008.

[22] J. Cui, Z.-P. Chen, Q. X. Wang, T.-R. Zhou, and C. Corbett. Experimental studies of bubble dynamics inside a corner. *Ultrasonics Sonochemistry*, 64:104951, 2020. ISSN 1350-4177.

[23] A. A. Doinikov. Mathematical model for collective bubble dynamics in strong ultrasound fields. *The Journal of the Acoustical Society of America*, 116(2):821–827, 2004.

[24] A. A. Doinikov and A. Bouakaz. Theoretical investigation of shear stress generated by a contrast microbubble on the cell membrane as a mechanism for sonoporation. *The Journal of the Acoustical Society of America*, 128(1):11–19, 2010.

[25] M. D. Van Dyke. Perturbation methods in fluid mechanics. *Parabolic Press*, 2nd edn., 1975.

[26] A. N. Frumkin. Surface tension curves of higher fatty acids and the equation of condition of the surface layer. *Z. phys. Chem*, 116:466–484, 1925.

[27] D. Fuster and F. Montel. Mass transfer effects on linear wave propagation in diluted bubbly liquids. *Journal of Fluid Mechanics*, 779:598–621, 2015.

[28] D. F. Gaitan, L. A. Crum, C. C. Church, and R. A. Roy. Sonoluminescence and bubble dynamics for a single, stable, cavitation bubble. *The Journal of the Acoustical Society of America*, 91(6):3166–3183, 1992.

[29] V. Garbin, D. Cojoc, E. Ferrari, E. Di Fabrizio, M. L. J. Overvelde, S. M. van der Meer, N. de Jong, D. Lohse, and M. Versluis. Changes in microbubble dynamics near a boundary revealed by combined optical micromanipulation and high-speed imaging. *Applied Physics Letters*, 90(11):114103, 2007.

[30] D. C. Gibson and J. R. Blake. The growth and collapse of bubbles near deformable surfaces. *Applied Scientific Research*, 38, 1982.

[31] M. Guédra, C. Inserra, C. Mauger, and B. Gilles. Experimental evidence of nonlinear mode coupling between spherical and nonspherical oscillations of microbubbles. *Phys. Rev. E*, 94:053115, Nov 2016.

[32] M. Guédra and C. Inserra. Bubble shape oscillations of finite amplitude. *Journal of Fluid Mechanics*, 857:681–703, 2018.

[33] M. Guédra, C. Cornu, and C. Inserra. A derivation of the stable cavitation threshold accounting for bubble-bubble interactions. *Ultrasonics Sonochemistry*, 38:168–173, 2017. ISSN 1350-4177.

[34] C. Hastings. *Approximations for Digital Computers*. Princeton University Press, USA, 1955. ISBN 0691079145.

[35] N. Jones. Ocean uproar: saving marine life from a barrage of noise. *Nature*, 568 (7751):158–161, April 2019.

[36] D. D. Joseph and J. Wang. The dissipation approximation and viscous potential flow. *J. Fluid Mech.*, 505:365–377, 2004.

[37] S. I. Karakashev and E. D. Manev. Effect of interactions between the adsorbed species on the properties of single and mixed-surfactant monolayers at the air/water interface. *Journal of Colloid and Interface Science*, 248(2):477–486, 2002. ISSN 0021-9797.

[38] J. B. Keller and M. Miksis. Bubble oscillations of large amplitude. *The Journal of the Acoustical Society of America*, 68(2):628–633, 1980.

[39] H. Lamb. *Hydrodynamics*. Cambridge U.P, 6th edition, 1932. ISBN 0521055156.

[40] W. Lauterborn and T. Kurz. Physics of bubble oscillations. *Reports on Progress in Physics*, 73(10):106501, 2010.

[41] W. Lauterborn, T. Kurz, R. Mettin, and C. D. Ohl. *Experimental and Theoretical Bubble Dynamics*, pages 295–380. John Wiley & Sons, Ltd, 2007. ISBN 9780470141694.

[42] M. Lee, E. Klaseboer, and B. C. Khoo. On the boundary integral method for the rebounding bubble. *Journal of Fluid Mechanics*, 570:407–429, 2007.

[43] T. A. Leslie and J. E. Kennedy. High-intensity focused ultrasound principles, current uses, and potential for the future. *Ultrasound Quarterly*, 22(4):263—272, December 2006. ISSN 0894-8771.

[44] J. Li. General explicit difference formulas for numerical differentiation. *Journal of Computational and Applied Mathematics*, 183(1):29 – 52, 2005. ISSN 0377-0427.

[45] S. J. Lind. A numerical study of the effect of viscoelasticity on cavitation and bubble dynamics. *Doctor of Philosophy thesis, Department of Mathematics, University of Cardiff*, 2010.

[46] S. J. Lind and T. N. Phillips. The effect of viscoelasticity on a rising gas bubble. *Journal of Non-Newtonian Fluid Mechanics*, 165(15):852–865, 2010. ISSN 0377-0257.

[47] S. J. Lind and T. N. Phillips. The influence of viscoelasticity on the collapse of cavitation bubbles near a rigid boundary. *Theoretical and Computational Fluid Dynamics*, 26:245–277, 2012.

[48] S. J. Lind and T. N. Phillips. The effect of viscoelasticity on the dynamics of gas bubbles near free surfaces. *Physics of Fluids*, 25(2):022104, 2013.

[49] Y. Q. Liu and Q. X. Wang. Stability and natural frequency of nonspherical mode of an encapsulated microbubble in a viscous liquid. *Physics of Fluids*, 28, 062102, 2016.

[50] Y. Q. Liu, M. Calvisi, and Q. X. Wang. Nonlinear oscillation and interface stability of an encapsulated microbubble under dual-frequency ultrasound. *Fluid Dynamics Research*, 49(2), 2017.

[51] Y. Q. Liu, Q. X. Wang, and A. M. Zhang. Surface stability of a bubble in a liquid fully confined in an elastic solid. *Physics of Fluids*, 30, 127106, 2018.

[52] M. S. Longuet-Higgins and E. D. Cokelet. The deformation of steep surface waves on water. I. A numerical method of computation. *Proceedings of the Royal Society of London. Series A, Mathematical and Physical Sciences*, 350(1660):1–26, 1976. ISSN 00804630.

[53] G. Lucca and A. Prosperetti. A numerical method for the dynamics of non-spherical cavitation bubbles. In *2d International Colloquium on Drops and Bubbles*, pages 175–181, March 1982.

[54] A. Maksimov. Splitting of the surface modes for bubble oscillations near a boundary. *Physics of Fluids*, 32, 102104, 2020.

[55] K. Manmi and Q. X. Wang. Acoustic microbubble dynamics with viscous effects. *Ultrasonics Sonochemistry*, 36:427 – 436, 2017. ISSN 1350-4177.

[56] T. J. Mason. Ultrasonic cleaning: An historical perspective. *Ultrasonics Sonochemistry*, 29:519–523, 2016.

[57] M. J. Miksis, Jean-Marc Vanden-Broeck, and J. B. Keller. Rising bubbles. *Journal of Fluid Mechanics*, 123:31–41, 1982.

[58] A. A. Ndiaye, R. Pflieger, B. Siboulet, J. Molina, J.-F. Dufrêche, and S. I. Nikitenko. Nonequilibrium vibrational excitation of OH radicals generated during multibubble cavitation in water. *The Journal of Physical Chemistry A*, 116(20):4860–4867, 2012.

[59] B. Y. Ni, A. M. Zhang, and G. X. Wu. Numerical and Experimental Study of Bubble Impact on a Solid Wall. *Journal of Fluids Engineering*, 137(3), 03 2015. ISSN 0098-2202. 031206.

[60] W. L. Nyborg. Acoustic streaming near a boundary. *J. Acoust. Soc. Am.*, 30: 329–339, 1958.

[61] C. D. Ohl, M. Arora, R. Dijkink, V. Janve, and D. Lohse. Surface cleaning from laser-induced cavitation bubbles. *Applied Physics Letters*, 89(7):074102, 2006.

[62] A. Philipp and W. Lauterborn. Cavitation erosion by single laser-produced bubbles. *Journal of Fluid Mechanics*, 361:75–116, 1998.

[63] R. Piorr. *Structure and Application of Surfactants*, pages 5–22. Springer Berlin Heidelberg, Berlin, Heidelberg, 1987. ISBN 978-3-642-71545-7.

[64] M. S. Plesset. On the stability of fluid flows with spherical symmetry. *J. Appl. Phys.*, 25(96), 1954.

[65] M. S. Plesset and R. B. Chapman. Collapse of an initially spherical vapour cavity in the neighbourhood of a solid boundary. *Journal of Fluid Mechanics*, 47(2):283–290, 1971.

[66] M. S. Plesset and A. Prosperetti. Bubble dynamics and cavitation. *Annual Review of Fluid Mechanics*, 9(1):145–185, 1977.

[67] S. Popinet and S. Zaleski. Bubble collapse near a solid boundary: A numerical study of the influence of viscosity. *Journal of Fluid Mechanics*, 464:137–163, 08 2002.

[68] W. H. Press, S. A. Teukolsky, W. T. Vetterling, and B. P. Flannery. *Numerical Recipes*. Cambridge University Press, 1988.

[69] A. Prosperetti. Viscous effects on perturbed spherical flows. *Quart. Appl. Math.*, 34(339), 1977.

[70] S. J. Putterman and K. R. Weninger. Sonoluminescence: How bubbles turn sound into light. *Annual Review of Fluid Mechanics*, 32(1):445–476, 2000.

[71] R. C. Reilly. Mean curvature, the Laplacian, and soap bubbles. *The American Mathematical Monthly*, 89(3):180–198, 1982. ISSN 00029890, 19300972.

[72] F. Reuter, S. Lauterborn, R. Mettin, and W. Lauterborn. Membrane cleaning with ultrasonically driven bubbles. *Ultrasonics Sonochemistry*, 37:542–560, 2017. ISSN 1350-4177.

[73] S. Roovers, T. Segers, G. Lajoinie, J. Deprez, M. Versluis, S. De Smedt, and I. Lentacker. The role of ultrasound-driven microbubble dynamics in drug delivery: From microbubble fundamentals to clinical translation. *Langmuir*, 35, 01 2019.

[74] M. J. Rosen and J. T. Kunjappu. *Reduction of Surface and Interfacial Tension by Surfactants*, chapter 5, pages 235–271. John Wiley & Sons, Ltd, 2012. ISBN 9781118228920.

[75] S. J. Shaw. The stability of a bubble in a weakly viscous liquid subject to an acoustic traveling wave. *Physics of Fluids*, 21(2):022104, 2009.

[76] S. J. Shaw. Nonspherical sub-millimeter gas bubble oscillations: Parametric forcing and nonlinear shape mode coupling. *Physics of Fluids*, 29(12):122103, 2017.

[77] Y. Shikhmurzaev. Capillary flows with forming interfaces. *Chapman and Hall/CRC*, 09 2007.

[78] W. D. Song, M. H. Hong, B. Lukyanchuk, and T. C. Chong. Laser-induced cavitation bubbles for cleaning of solid surfaces. *Journal of Applied Physics*, 95(6): 2952–2956, 2004.

[79] H. A. Stone and L. G. Leal. The effects of surfactants on drop deformation and breakup. *Journal of Fluid Mechanics*, 220:161–186, 1990.

[80] A. H. Stroud and D. Secrest. *Gaussian quadrature formulas*. Prentice-Hall series in automatic computation. Prentice-Hall, Englewood Cliffs, NJ, 1966.

[81] A. J. Szeri, B. D. Storey, A. Pearson, and J. R. Blake. Heat and mass transfer during the violent collapse of nonspherical bubbles. *Physics of Fluids*, 15(9):2576–2586, 2003.

[82] B. B. Taib. Boundary integral method applied to cavitation bubble dynamics. *Doctor of Philosophy thesis, Department of Mathematics, University of Wollongong*, 1985.

[83] C. D. Taylor, D. S. Valkovska, and C. D. Bain. A simple and rapid method for the determination of the surface equations of state and adsorption isotherms for efficient surfactants. *Phys. Chem. Chem. Phys.*, 5:4885–4891, 2003.

[84] J. A. Tsamopoulos and R. A. Brown. Nonlinear oscillations of inviscid drops and bubbles. *Journal of Fluid Mechanics*, 127:519–537, 1983.

[85] K. Tsiglifis and N. A. Pelekasis. Nonlinear oscillations and collapse of elongated bubbles subject to weak viscous effects. *Physics of Fluids*, 17(10):102101, 2005.

[86] N. Vyas, Q. X. Wang, K. A. Manmi, R. L. Sammons, S. A. Kuehne, and A. D. Walmsley. How does ultrasonic cavitation remove dental bacterial biofilm? *Ultrasonics Sonochemistry*, 67, 105112, 2020.

[87] Q. X. Wang. Multi-oscillations of a bubble in a compressible liquid near a rigid boundary. *Journal of Fluid Mechanics*, 745, 2014.

[88] Q. X. Wang. Local energy of a bubble system and its loss due to acoustic radiation. *Journal of Fluid Mechanics*, 797:201–230, 2016.

[89] Q. X. Wang and J. R. Blake. Non-spherical bubble dynamics in a compressible liquid. Part 1. Travelling acoustic wave. *Journal of Fluid Mechanics*, 659:191–224, 2010.

[90] Q. X. Wang and J. R. Blake. Non-spherical bubble dynamics in a compressible liquid. Part 2. Acoustic standing wave. *Journal of Fluid Mechanics*, 679:559–581, 2011.

[91] Q. X. Wang and K. Manmi. Three dimensional microbubble dynamics near a wall subject to high intensity ultrasound. *Physics of Fluids*, 26(3):032104, 2014.

[92] Q. X. Wang, K. S. Yeo, B. C. Khoo, and K. Y. Lam. Vortex ring modelling of toroidal bubbles. *Theoretical and Computational Fluid Dynamics*, 19(5):303–317, October 2005.

[93] Q. X. Wang, W. K. Liu, A. M. Zhang, and Y. Sui. Bubble dynamics in a compressible liquid in contact with a rigid boundary. *Interface Focus*, 5(5):20150048, 2015.

[94] Q. X. Wang, W. Liu, D. Leppinen, and Walmsley D. Microbubble dynamics in a viscous compressible liquid near a rigid boundary. *IMA Journal of Applied Mathematics*, 84(4):696–711, August 2019. ISSN 0272-4960.

[95] Q. X. Wang, M. Mahmud, J. Cui, W. R. Smith, and A. D. Walmsley. Numerical investigation of bubble dynamics at a corner. *Physics of Fluids*, 32, 053306, 2020.

[96] Q. X. Wang, W. Liu, C. Corbett, and W. R. Smith. Microbubble dynamics in a viscous compressible liquid subject to ultrasound. *Physics of Fluids*, 34, 012105, 2022.

[97] Y.-C. Wang and C. Brennen. Shock waves and noise in the collapse of a cloud of cavitation bubbles. *International Symposium on Shock Waves*, 06 1995.

[98] A. M. Zhang and B. Ni. Three-dimensional boundary integral simulations of motion and deformation of bubbles with viscous effects. *Computers & Fluids*, 92, 01 2013.

[99] S. Zhang, J. H. Duncan, and G. L. Chahine. The final stage of the collapse of a cavitation bubble near a rigid wall. *Journal of Fluid Mechanics*, 257:147–181, 1993.

[100] S. Zhang, J. H. Duncan, and G. L. Chahine. The behavior of a cavitation bubble near a rigid wall. In *Bubble Dynamics and Interface Phenomena*, pages 429–436, Dordrecht, 1994. Springer Netherlands.